AD-A220 249

④

GL-TR-89-0308

Geophysical Studies Related to Geodetic
Reference Frames

John Wahr

University of Colorado
Department of Physics
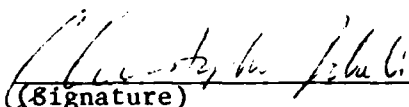Boulder, CO 80309-0390

9 February 1990

Final Report
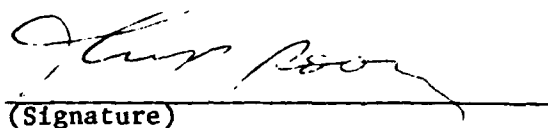2 April 1986–30 April 1989

**DTIC
ELECTE
APR 10 1990
B**

"This technical report has been reviewed and is approved for publication"

(Signature)
(Signature)
GERALD SHAW
Contract Manager

(Signature)
(Signature)
THOMAS ROONEY
Branch Chief

FOR THE COMMANDER

(Signature)
(Signature)
DONALD H. ECKHARDT
Division Director

This report has been reviewed by the ESD Public Affairs Office (PA) and is releasable to the National Technical Information Service (NTIS).

Qualified requestors may obtain additional copies from the Defense Technical Information Center. All others should apply to the National Technical Information Service.

If your address has changed, or if you wish to be removed from the mailing list, or if the addressee is no longer employed by your organization, please notify GL/IMA, Hanscom AFB, MA 01731. This will assist us in maintaining a current mailing list.

Do not return copies of this report unless contractual obligations or notices on a specific document requires that it be returned.

REPORT DOCUMENTATION PAGE

Public reporting burden for this collection of information is estimated to average 1 hour per response, including the time for reviewing instructions, searching existing data sources, gathering and maintaining the data needed, and completing and reviewing the collection of information. Send comments regarding this burden estimate or any other aspect of this collection of information, including suggestions for reducing this burden, to Washington Headquarters Services, Directorate for Information Operations and Reports, 1215 Jefferson Davis Highway, Suite 1204, Arlington, VA 22202-4302, and to the Office of Management and Budget, Paperwork Reduction Project (0704-0188), Washington, DC 20503.

1. AGENCY USE ONLY (Leave blank)	2. REPORT DATE Feb. 9, 1990	3. REPORT TYPE AND DATES COVERED Final Report - Apr. 2, 1986 - Apr. 30, 1989

4. TITLE AND SUBTITLE

Geophysical Studies Related to Geodetic Reference Frames

5. FUNDING NUMBERS

61102F
2309G1BR

Contract F19628-86-K-0011

6. AUTHOR(S)

John Wahr

7. PERFORMING ORGANIZATION NAME(S) AND ADDRESS(ES)

University of Colorado
Department of Physics
Boulder, CO 80309-0390

8. PERFORMING ORGANIZATION REPORT NUMBER

9. SPONSORING/MONITORING AGENCY NAME(S) AND ADDRESS(ES)

Geophysics Laboratory
Hanscom AFB
Massachusetts 01731-5000

Contract Manager: Gerry Shaw, Lt Col, USAF/LWG

10. SPONSORING/MONITORING AGENCY REPORT NUMBER

GL-TR-89-0308

11. SUPPLEMENTARY NOTES

12a. DISTRIBUTION/AVAILABILITY STATEMENT

Approved for public release; distribution unlimited

12b. DISTRIBUTION CODE

13. ABSTRACT (Maximum 200 words)

This contract was used to support work on several different problems:
(1) We developed models to estimate the effects of atmospheric pressure loading on surface displacements and surface gravity.
(2) We investigated the effects of aspherical core structure on the forced nutations.
(3) We studied the possibility of aspherical structure inside the core, and its possible implications for geodetic and seismic constraints on the core-mantle boundary topography.
(4) We began a study of the ocean's response to pressure, and its implications for certain geodetic observations. So far, we have concentrated on trying to assess the accuracy of pressure data sets over the ocean.
(5) We used monthly, global tide gauge data to investigate certain long period oceanic disturbances which have implications for the interpretation of geodetic (eg., rotation, earth tide, crustal dynamics) data.

14. SUBJECT TERMS

Geodegy, earth rotation, earth and ocean tides, earth's core.

15. NUMBER OF PAGES

86

16. PRICE CODE

17. SECURITY CLASSIFICATION OF REPORT	18. SECURITY CLASSIFICATION OF THIS PAGE	19. SECURITY CLASSIFICATION OF ABSTRACT	20. LIMITATION OF ABSTRACT
Unclassified	Unclassified	Unclassified	SAR

CHAPTER I

SUMMARY

This contract was used to support work on several different problems. Each chapter, below, describes a different problem. In this chapter, we summarize the results of those later chapters.

SUMMARY OF CHAPTER II

We examined the theoretical effects of air pressure loading on surface displacements and surface gravity. We concluded that global baseline changes due to this effect can frequently be 2 cm or more, and that gravity perturbations can be as large as 3-6 microgals. The effects at a station can be adequately calculated using real pressure data within about 1000 km of that station. For inland points, adequate results can be obtained using only two parameters to describe the pressure, as described by Rabbel and Zschau (J.Geophys., 56, 81-99, 1985). At points near the coast, however, more complete pressure data are required.

SUMMARY OF CHAPTER III

We investigated the effects of core structure on the forced nutations. VLBI observations (from Herring, et al., and Gwinn, et al.) and tidal gravity studies (from Levine, et al., and Neuberg, et al.) suggest that the fluid core resonance in the nutations and tides should have an inertial space period of around 433 days, instead of the 460 days predicted for a hydrostatically pre-stressed earth. We developed a theoretical model of the resonance for an earth which is non-hydrostatically pre-stressed, but which has a fluid outer core. We find, for this model, that the resonance is sensitive to the l=2, m=0 spherical harmonic term in the non-hydrostatic structure, but not to any other spherical harmonic component.

SUMMARY OF CHAPTER IV

We found that there can be lateral, non-hydrostatic structure inside th̲ ̲d core, caused by gravitational forcing from the mantle, from the inner core, or from topography on the core/mantle or inner core/outer core boundaries. The possibility of such structure has been overlooked in the past, and it can have important implications for geodetic and seismic studies of the core. We developed the differential equations which describe the structure, and considered the effects of the solutions on nutation and tidal constraints for core/mantle boundary topography. We concluded that those constraints could accommodate large l=2, m=0 topography on the boundary, if there was a thin, low density fluid layer just beneath the boundary.

1

SUMMARY OF CHAPTER V

We began addressing the problem of the ocean's response to pressure. It is important to understand this response when: (a) modelling the pressure-induced and wobble-induced crustal deformation at gravity, VLBI, satellite ranging, etc., sites within a few hundred km of the coast; (b) estimating the effects of global pressure on polar motion; (c) using satellite altimeter data to study the wind-driven circulation of the ocean. We analyzed GEOSAT altimeter data to study this response. (GEOSAT data are particularly helpful to investigate the short period response; tide gauge data are helpful to study the long period response - see item (6), below.)

Our first work in this area has been to assess the reliability of global pressure data. We found substantial differences between results from different meteorological centers, particularly over the Southern Pacific.

SUMMARY OF CHAPTER VI

We used monthly tide gauge data from the Permanent Service for Mean Sea Level in Bidston, England, to investigate certain long-period disturbances in the ocean. We found: (a) the 18.6 year lunar tide and 14 month pole tide are close to equilibrium in the global ocean (it is important to understand these ocean tides when interpreting: (i)satellite ranging results for the 18.6 year earth tide, and (ii) polar motion observations of the Chandler wobble period, in terms of mantle anelasticity); (b) the response of the ocean to pressure is very close to inverted barometer at periods of two months and longer; (c) the global rise in sea level over the last 80 years, after removing the effects of post-glacial rebound on individual tide gauge records, has been between 1.1 mm/yr and 1.9 mm/yr.

2

CHAPTER II

DISPLACEMENTS OF THE EARTH'S SURFACE DUE TO ATMOSPHERIC LOADING:
EFFECTS ON GRAVITY AND BASELINE MEASUREMENTS

SUMMARY

Atmospheric mass loads and deforms the earth's crust. By performing a convolution sum between daily, global barometric pressure data and mass loading Green's functions, we estimate the time dependent effects of atmospheric loading, including those associated with short–term synoptic storms, on surface point positioning measurements and surface gravity observations. We calculate the response for both an oceanless earth and an earth with an inverted barometer ocean. Load responses for near-coastal stations are significantly affected by the inclusion of an inverted barometer ocean. Peak to peak vertical displacements are frequently 15–20 mm with accompanying gravity perturbations of 3–6 μGal. Baseline changes can be as large as 20 mm or more. The perturbations are largest at higher latitudes and during winter months. These amplitudes are consistent with the results of Rabbel and Zschau [1985], who modeled synoptic pressure disturbances as Gaussian functions of radius around a central point. Deformation can be adequately computed using real pressure data from points within about 1000 km of the station. Knowledge of local pressure, alone, is not sufficient. Rabbel and Zschau's hypothesized corrections for these displacements, which use local pressure and the regionally averaged pressure, prove accurate at points well inland but are, in general, inadequate within a few hundred kilometers of the coast.

INTRODUCTION

Recent improvements in geodetic instrumentation and measurement techniques have made the detection of crustal movements over short time periods feasible. It is expected that space techniques such as very long baseline interferometry (VLBI) and satellite laser ranging will soon have the capability of measuring distances over long baselines to within a centimeter or better (see, for example, *Herring* [1986], and *Cohen and Smith* [1985]. Relative gravity observations used to detect vertical crustal motions have already achieved sub-microGal accuracies over long time periods (see for example, *Richter* [1983], *Levine et al.* [1986], and *Goodkind* [1986]). These techniques promise to provide valuable information about tectonic deformation of the earth. Since nontectonic processes can also cause crustal motions, their effects need to be considered as well and, if necessary, removed from the data. In this chapter we consider displacements caused by global barometric pressure fluctuations around the earth.

Variations in the horizontal distribution of atmospheric mass induce deformations within the earth. The interaction between the atmosphere and the earth is through pressure loading at the surface and, particularly at longer wavelengths, through the gravitational attraction of the atmospheric mass. The displacement of the surface is primarily vertical, and there is a change in the acceleration of gravity at the displaced surface.

Horizontal changes in atmospheric mass can be inferred from surface atmospheric pressure measurements. *Stolz and Larden* [1979] concluded that global seasonal fluctuations in barometric pressure would, in general, contribute less than a centimeter to surface displacements. The largest pressure variations, however, are those associated with synoptic scale storms. Because the average life span of these storms is approximately 5 days [*Klein*, 1956], they do not contribute appreciably to the seasonal variability in global pressure.

3

A simple calculation using elastic Green's functions for the spherically symmetric Gutenberg-Bullen A earth model from *Farrell* [1972] shows that a uniform pressure increase of 20 mbar over a disk of diameter 2000 km causes a depression of 10 mm at the center of the disk. This displacement scales linearly with the pressure over the disk and also increases, although more slowly than linearly, with the diameter of the disk. For example, if the 20-mbar pressure is distributed over a disc with only a 1000-km diameter, the central depression is about 6 mm. Since large synoptic storms can have spatial scales of about 2000 km and peak-to-peak pressure fluctuations which may be as large as 40-50 mbar, it is probable that vertical displacements could frequently be 10 mm or larger along a storm track.

Rabbel and Zschau [1985] estimated the deformation caused by these synoptic storms by assuming that the accompanying pressure disturbance is a Gaussian function of radius about some central high or low and then convolving that pressure distribution with Farrell's Green's functions. Their results suggest that vertical displacements of the earth's surface of 10-20 mm can occur. They found that they could adequately predict the deformation caused by a Gaussian pressure distribution by using a simple regression equation together with estimates of the local pressure at the point of interest and of the average surface pressure with a 2000-km radius of the point.

In this chapter we extend and assess Rabbel and Zschau's results by convolving Farrell's Green's functions with real, interpolated global pressure data. Radial and horizontal displacements as well as changes in the gravitational acceleration for various stations are calculated. Baseline changes between stations are also examined.

In particular, we address the following questions. First, are the displacements predicted using real data as potentially important as suggested by the results of Rabbel and Zschau? We conclude that they are. We find that displacements are generally larger at higher latitudes, and during the winter months. Typically, peak-to-peak displacements of a centimeter or two occur during each winter month at higher latitudes.

Second, a change in atmospheric pressure can cause a change in sea level height which further deforms the earth. How important is it to include this ocean-induced deformation in the calculations? We find that if the ocean responds to pressure variations as an inverted barometer, the effect on vertical displacements can be greater than 10 mm at stations on the coast, and often 10 mm within several hundred kilometers of the coast.

Third, do Rabbel and Zschau's regression equations provide adequate approximations to the deformation predicted from real data? We find that the equations work well at inland points but are, in general, inadequate at points within a few hundred kilometers of the coast, assuming that an inverted barometer ocean response is appropriate.

METHOD

Farrell [1972] constructed Green's functions to describe the response of an elastic earth to a point load on its surface. Gravitational accelerations, displacements, tilts, and strains can be determined for any surface load by evaluating a convolution sum between the Green's functions and the load distribution. The effects of anelasticity at the periods of interest here are almost certain to be less than 10% and so, judging by the results below, can be ignored.

We obtained (from the National Center for Atmospheric Research in Boulder, Colorado) the National Meteorological Center (NMC) global atmospheric pressure values from 1979 through 1984. The NMC calculated surface pressure values twice daily for a 2.5° × 2.5° grid over the entire surface of the earth. Because we are interested only in time dependent displacements, we subtract the atmospheric pressure for an arbitrary day from all other daily values.

To estimate the displacement at a surface point, we partition the earth into a similar 2.5° × 2.5° grid system. Grid elements that lie within 5° of the field point are further subdivided into smaller units. Values for the Green's functions are assigned to each grid element and are determined by the angular distance between the element and the surface point. The Green's functions are multiplied by

the daily atmospheric load, and the results are summed. In this way, we can determine the radial and horizontal displacements and the change in the gravitational acceleration at any point on the surface of the earth. We calculate the change in gravity due to the elastic deformation of the solid earth plus that due to the gravitational attraction of all displaced atmospheric mass except for the excess mass directly above the point. The contribution from that excess mass can be crudely approximated by multiplying the local pressure in millibars by the factor 0.42 μGal/mbar, determined by assuming the excess mass is an infinite plane of uniform density. This latter pressure contribution is typically larger than the effects we are considering here by a factor of 3 and is already routinely included in many data analyses. The effects of the mass directly overhead can not be exactly described with a constant factor of 0.42 μGal/mbar, since the mass is not a uniform plane. A better way to remove those effects is to fit them to the data [*Warburton and Goodkind*, 1977; *Spratt*, 1982; *Levine et al.*, 1986].

RESULTS

Deformations and gravitational accelerations are calculated using both an oceanless earth model and a model in which the oceans respond as an inverted barometer to atmospheric loading. The inverted barometer hypothesis states that for every millibar increase in atmospheric pressure, the sea surface depresses locally by 1 cm. This implies that the ocean basins experience none of the forces associated with barometric pressure fluctuations and is equivalent to setting the total incremental mass load over the ocean basins equal to zero. However, to conserve oceanic mass, the inverted barometer hypothesis must be modified slightly. If there is a net increase or decrease in the mass of air above the oceans, the seafloor experiences a uniform pressure D acting everywhere on the earth's surface under the oceans and equal to

$$D = \frac{\int_s \Delta P \, dS}{A}$$

where ΔP is the local change in pressure, A is the surface area of the oceans, and the integral is over the ocean surface. Results indicate that the effects of the pressure D on vertical displacements are no more than 3 mm for coastal geodetic stations and are even smaller at inland points.

It is likely that the ocean does respond to pressure as an inverted barometer at periods of weeks to a few years. *Wunsch* [1972] compared local pressure and tide gauge data taken at Bermuda and concluded that a local inverted barometer response was probably appropriate at periods as short as 3 or 4 days. On the other hand, the decidedly nonequilibrium diurnal ocean tides imply that the global response is certainly not an inverted barometer at periods close to 1 day. Furthermore, *Eubanks et al.* [1985] have concluded from recent polar motion data that the southern ocean may differ significantly from the inverted barometer response. We are thus not certain that our global inverted barometer assumption is appropriate for the short–period synoptic storms which most concern us. (See *Chelton and Enfield* [1986] for a summary of observational evidence for the inverted barometer response.)

We attempt to bound the actual atmospheric-induced deformations by using the oceanless earth and the inverted barometer model as end points. The larger estimates of atmospheric loading effects are obtained for the oceanless earth model. Figure II.1 is a graph of the calculated surface displacements and associated gravity perturbations at Boulder, Colorado, during 1980 for such a model. The largest peak–to–peak barometric pressure fluctuations (Figure II.1a) and crustal responses occur during the winter months where radial displacements often exceed 10 mm (Figure II.1b). Horizontal displacements are also calculated (not shown) but are found to be only between 1 and 2 mm. Fluctuations in the local value of gravity (besides those approximately described by the 0.42 μGal/mbar factor discussed above) are shown in Figure II.1c. Perturbations are determined to be about 2–4 μGal and are mostly due to the vertical displacement of the surface. The calculated displacements and gravity fluctuations are somewhat smaller during the summer months, with maximum peak to peak radial displacements of about 10 mm.

5

At higher latitudes the loading effects are systematically larger due to the larger pressure variations there. For example, at Onsala, Sweden, during 1980 our calculations for an oceanless earth predict that vertical crustal motions of 20–30 mm (Figure II.2b) and gravity perturbations of 6–8 μGal (Figure II.2c) occur regularly during the winter months. Horizontal displacements are larger as well but are still small, having maximum magnitudes of 2–3 mm.

We then recompute the load responses using the inverted barometer assumption. The addition of oceans to the earth model has a greater effect on the points closer to the coast. Radial displacements at Onsala, situated on the North Sea and close to the North Atlantic Ocean, are reduced by as much as 10 mm (Figure II.3b) and gravity perturbations are decreased by up to 2 μGal. A large reduction is not surprising since when the inverted barometer assumption is applied, the crust under the nearby ocean no longer experiences the effects of large pressure fluctuations and therefore no longer contributes to the deformations at Onsala. The load response at inland stations is less affected by the addition of an inverted barometer ocean to the model. For example, at Boulder the displacements calculated for an inverted barometer model differ by only a couple of millimeters from those for the oceanless earth model (Figure II.3a). Still, we find that differences of at least a centimeter can persist up to several kilometers inland.

The results of our calculated perturbations in gravity were used by *Levine et al.* [1986] to correct gravity measurements for atmospheric effects. They used a LaCoste and Romberg gravimeter to record continuously the local changes in the gravitational acceleration at Boulder from May through December 1983. By removing the gravitational effects due to global pressure variations, Levine et al. were able to reduce the amplitude of their residuals by about one third and improve the agreement between calculated and observed tidal admittances.

Baseline lengths are affected by displacements of the end points. Because the displacements are mostly radial, the effects are largest on very long baselines. As an example, the effects on the Onsala to Haystack Observatory baseline during 1984 are shown in Figure II.4a. This baseline is too short (only about one earth radius) to maximize the effect, but it is one of the more carefully and frequently measured VLBI baselines [*Herring et al.* 1986].

Vertical motions at both Onsala and Haystack can be as large as 30 mm for the oceanless earth model. Corresponding baseline changes of 15–20 mm are common, and maximums of 35 mm can occur during the winter. Baseline changes are decreased by using the inverted barometer assumption (Figure II.4b), where maximum variations are of the order of 20 mm. We find similar baseline changes for other medium to long baselines at high latitudes.

The effects on a baseline depend on the relative motion of the end points. An examination of the vertical motions at Onsala and Haystack indicates that the earth deforms approximately in-phase at these points, thus increasing the atmospheric effects on baseline changes. When pressure variations associated with synoptic storms around the globe are expanded in terms of spherical harmonics, Y_n^m, the largest coefficients are found to occur at $n=6$ and 7 [*Spratt*, 1982]. These harmonics correspond to a wavelength of around 6000 km, which is about equal to the distance over the earth's surface between Onsala and Haystack, a result consistent with the in-phase deformation at the two stations.

Herring et al. [1986] measured the Onsala-Haystack baseline with VLBI on 34 different days during 1980–1984. We compared our estimates for this baseline with their results and found no significant correlation. However, our estimates with the inverted barometer ocean for those particular days are mostly within only a few millimeters of each other, with only one outlying point as large as 10 mm. By contrast, errors in the VLBI results due to uncertainties in the atmospheric water vapor are probably around 20 mm or so for this data (T. Herring, personal communication, 1986).

The various results described above are consistent in amplitude with the general results of *Rabbel and Zschau* [1985]. They reinforce Rabbel and Zschau's conclusion that atmospheric pressure corrections to geodetic point positioning and gravity measurements should be considered in future analyses.

We next estimate the spatial extent of real data required in order to accurately apply atmospheric corrections using the method described in this chapter. Dotted curve in Figure II.5 shows the predicted radial displacements at Boulder obtained by considering only those pressure changes in the NMC data which occur at points within a 10° (1000 km radius) of Boulder. Solid curve shows the results obtained

using the entire global data set. The difference between these results and those obtained using all the data is always less than 3 mm, suggesting that it is not presently necessary to consider the entire atmospheric load. However, we also find that it is not sufficient to use only the pressure variations close to the point of interest. For example, calculations which include only the pressure fluctuations within 1° (about 100 km) of Boulder can differ from the global results by as much as 10 mm (dashed curve in Figure II.5).

To explore this result further, we calculate the vertical displacements at Boulder on January 8, 1980, using several different cutoff angles for the data. The vertical displacement computed using the entire global data set is large on this day, roughly 13 mm. The displacements predicted using different cutoff angles are plotted in Figure II.6. The differences from the global result are 5 mm for a 5° cutoff, 2.5 mm for a 10° cutoff, and less than 0.5 mm for a 20° cutoff. Differences can be somewhat larger on other days and at higher latitudes, since the maximum displacements are larger there. These results suggest that pressure data from at least the surrounding 1000 km is desirable, given the accuracy levels of the various new geodetic techniques. This distance is consistent with the observation that the largest storms are on the order of 2000 km across.

It would be impractical if a barometer array had to be installed whenever an observation was made, to determine pressure variations within the surrounding 1000 km. Fortunately, interpolated global pressure data are available from the NMC with only a few weeks delay. Still, it might be convenient in some cases if a linear relationship between the local and regionally averaged pressures and the local crustal displacement could be found. By mathematically modeling the pressure distribution of synoptic scale storms as an exponentially decaying function with radius from the center of the storm and convolving the result with Farrell's Green's functions, *Rabbel and Zschau* [1985] hypothesized a relationship between the local pressure, the average pressure within 2000 km of the station, and the local radial displacement and change in the acceleration of gravity:

Radial displacement [*Rabbel and Zschau*, 1985]

$$U = -0.90P_l - 0.35(P_s - P_l)$$

Gravity, besides the 0.42 μGal/mbar factor described above [*Rabbel and Zschau*, 1985],

$$G = -0.17P_l - 0.08(P_s - P_l)$$

where U is in millimeters, G is in microGal, and the pressure values P_l and P_s are in millibars. Here, P_s is the local pressure change, and P_l is obtained by averaging the pressure variations within a surrounding radius of 2000 km. Rabbel and Zschau suggested that for an inverted barometer ocean, P_l should be calculated by setting the pressure changes for the ocean areas to zero. To use these corrections, one would only need to know the local pressure changes and to use a weather map to obtain a value for the average pressure in the surrounding area.

To assess the accuracy of these equations, we use them to estimate vertical displacements at various points, using both the oceanless earth and the inverted barometer ocean models. The results are compared with displacements calculated using the real NMC pressure data (for comparison, we let D equal zero when using the inverted barometer model). For an oceanless earth model and at points well inland for the inverted barometer model, the results generally agree to within 90%, suggesting that the equations of Rabbel and Zschau are useful for calculating atmospheric corrections for inland points. This is mostly confirmation that the pressure disturbances associated with large storms are, indeed, reasonably well represented by Gaussian functions. Contour plots of the pressure data during times of maximum displacement further reinforce this assumption.

However, the agreement is not as encouraging near coasts for the inverted barometer ocean. For example, the two sets of results for Onsala during the winter of 1980 have peak to peak discrepancies of as much as 10 mm (Figure II.7). Discrepancies as large as 5 mm or more can persist for several hundred kilometers inland. The reason is that when the pressure is set equal to zero over the oceans, the Gaussian character of the storms is destroyed sufficiently that Rabbel and Zschau's regression

7

equations are no longer adequate. W. Rabbel (personal communication, 1986) suggests that corrections for near-coastal stations might conceivably be obtained by extending the regression equations to include a modification factor appropriate to each station. On the other hand, since there is only a few weeks delay in obtaining the NMC sea level pressure data, accurate atmospheric load corrections can be obtained relatively quickly for both coastal and inland stations by performing a convolution sum with the data as outlined in this chapter.

CONCLUSIONS

The magnitude of pressure-induced deformations of the earth's surface and of the associated gravity changes are within the accuracies obtainable by present measurement techniques. Using real atmospheric data, we conclude that vertical surface displacements of 20 mm and gravity perturbations of 4 μGal are common. The displacements are generally the largest during winter and at higher latitudes. These amplitudes are consistent with the conclusions of *Rabbel and Zschau* [1985], who used an analytical, Gaussian model for storm–related pressure disturbances. Rabbel and Zschau proposed simple two–parameter equations to approximate these deformations. We find that the equations are accurate for points well inland but near the coasts they can differ from results computed with real data by as much as 50%. The gravity amplitudes are also consistent with the results estimated by *Spratt* [1982] using atmospheric pressure data. (Spratt used a somewhat different computational approach than .s.)

At coastal stations and at points within a few hundred kilometers of the coast, the value of the response depends on the ocean model applied. At Onsala, Sweden, during 1980, for example, the maximum vertical displacements are reduced from 45 mm for an oceanless earth to 30 mm for an inverted barometer ocean. Calculated maximum changes for the Onsala-Haystack baseline are between 35 and 20 mm depending on the ocean model. Observation points more than a few hundred kilometers inland are not appreciably affected by the choice of ocean model. It is not certain that the inverted barometer assumption is justified at the time scale of synoptic storms, but we have attempted to bound the true surface displacements between the oceanless earth and inverted barometer assumptions. We are presently working to understand the global oceanic response to pressure in more detail.

The results presented here indicate that air pressure corrections are large enough to affect significantly many point positioning measurements. Adequate corrections are not possible if only local pressure fluctuations are included. We have determined empirically that pressure data from a 1000–km radius around the observation point are required to match accurately the displacement calculated from global pressure data.

CHAPTER II REFERENCES

Chelton, D. B., and D. B. Enfield, Ocean signals in tide gauge records, *J. Geophys. Res., 91*, 9081–9098, 1986.

Cohen, S. C., and D. E. Smith, LAGEOS scientific results: Introduction, *J. Geophys. Res., 90*, 9217–9220, 1985.

Eubanks, T. M., and J. O. Dickey, J. A. Steppe, Rapid polar motions during 1984, *EOS Trans. AGU, 66*, 854, 1985.

Farrell, W. E., Deformation of the earth by surface loads, *Rev. Geophys., 10*, 761–797, 1972.

Goodkind, J. M., Continuous measurement of nontidal variations of gravity, *J. Geophys. Res., 91*, 9125–9134, 1986.

Herring, T. A., Precision of vertical position estimates from very long baseline interferometry, *J. Geophys. Res., 91*, 9177–9182, 1986.

Herring, T. A., I. I. Shapiro, T. A. Clark, C. Ma, J. W. Ryan, B. R. Schupler, C. A. Knight, G. Lundqvist, D. B. Shaffer, N. R. Vandenberg, B. E. Corey, H. F. Hinteregger, A. E. E. Rogers, J.

C. Webber, A. R. `.nitney, G. Elgered, B. O. Rönnäng, and J. L. Davis, Geodesy by radio inter-ferometry: Evidence for contemporary plate motion, *J. Geophys. Res.*, *91*, 8341-8347, 1986.

Klein, W. H., The frequency of cyclones and anticyclones in relation to the mean circulation, *J. Meterol.*, *13*, 98-102, 1956.

Levine, J., J. C. Harrison, and W. Dewhurst, Gravity tide measurements with a feedback gravity meter, *J. Geophys. Res.*, *91*, 12,835-12,841, 1986.

Rabbel, W., and J. Zschau, Static deformations and gravity changes at the earth's surface due to atmospheric loading, *J. Geophys.*, *56*, 81-99, 1985.

Richter, B., Three years of registration with the superconducting gravimeter, *Bull. Inf. Marees Terr.*, *93*, 1-9, 1983.

Spratt, R. S., Modelling the effect of atmospheric pressure variations on gravity, *Geophys. J. R. Astron. Soc.*, *71*, 173-186, 1982.

Stolz, A., and D. R. Larden, Seasonal displacement and deformation of the earth by the atmosphere, *J. Geophys. Res.*, *84*, 6185-6194, 1979.

Warburton, R. J., and J. M. Goodkind, The influence of barometric-pressure variations on gravity, *Geophys. J. R. Astron. Soc.*, *48*, 281-292, 1977.

Wunsch, C., Bermuda sea level in relation to tides, weather, and baroclinic fluctuations, *Rev. Geophys.*, *10*, 1-49, 1972.

CHAPTER II FIGURE CAPTIONS

Figure II.1. (*a*) Local pressure variations at Boulder, Colorado, for winter 1980. (*b*) Radial displacements. (*c*) Gravity perturbations (does not include the 0.42 µGal/mbar factor discussed in text) Note that the zero lines in these plots have has no physical significance since daily pressure was differenced with that for an arbitrary day.

Figure II.2. Same as Figure 1 for Onsala, Sweden, for winter 1980.

Figure II.3. (*a*) The solid line represents the radial displacements at Boulder for the inverted barometer model; the dashed line represents the radial displacements for an oceanless earth model. (*b*) Same as Figure 3*a* but for Onsala.

Figure II.4. (*a*) Baseline change between Haystack, Massachusetts and Onsala for the oceanless earth model [1984]. (*b*) Same as Figure 4*a* for the inverted barometer model.

Figure II.5. Radial displacements at Boulder for January 1982 with the inverted barometer model. Solid curve, using data from the entire earth; dotted curve, considering only pressure changes within 1000 km of Boulder; dashed curve, considering only pressure changes within 100 km of Boulder.

Figure II.6. Radial displacements at Boulder, computed for January 8, 1980, using different cutoff angles θ (pressure values are set to zero at all grid points further than θ away from Boulder). the vertical subsidence at Boulder computed using the entire, global data set is 13.4 mm.

Figure II.7. Radial displacements at Onsala during winter 1980, including inverted barometer oceans. The solid curve represents displacements calculated from real data, as discussed in this chapter. The dashed curve represents displacements calculated from Rabbel and Zschau's regression equation. Agreement is much better at stations a few hundred kilometers inland.
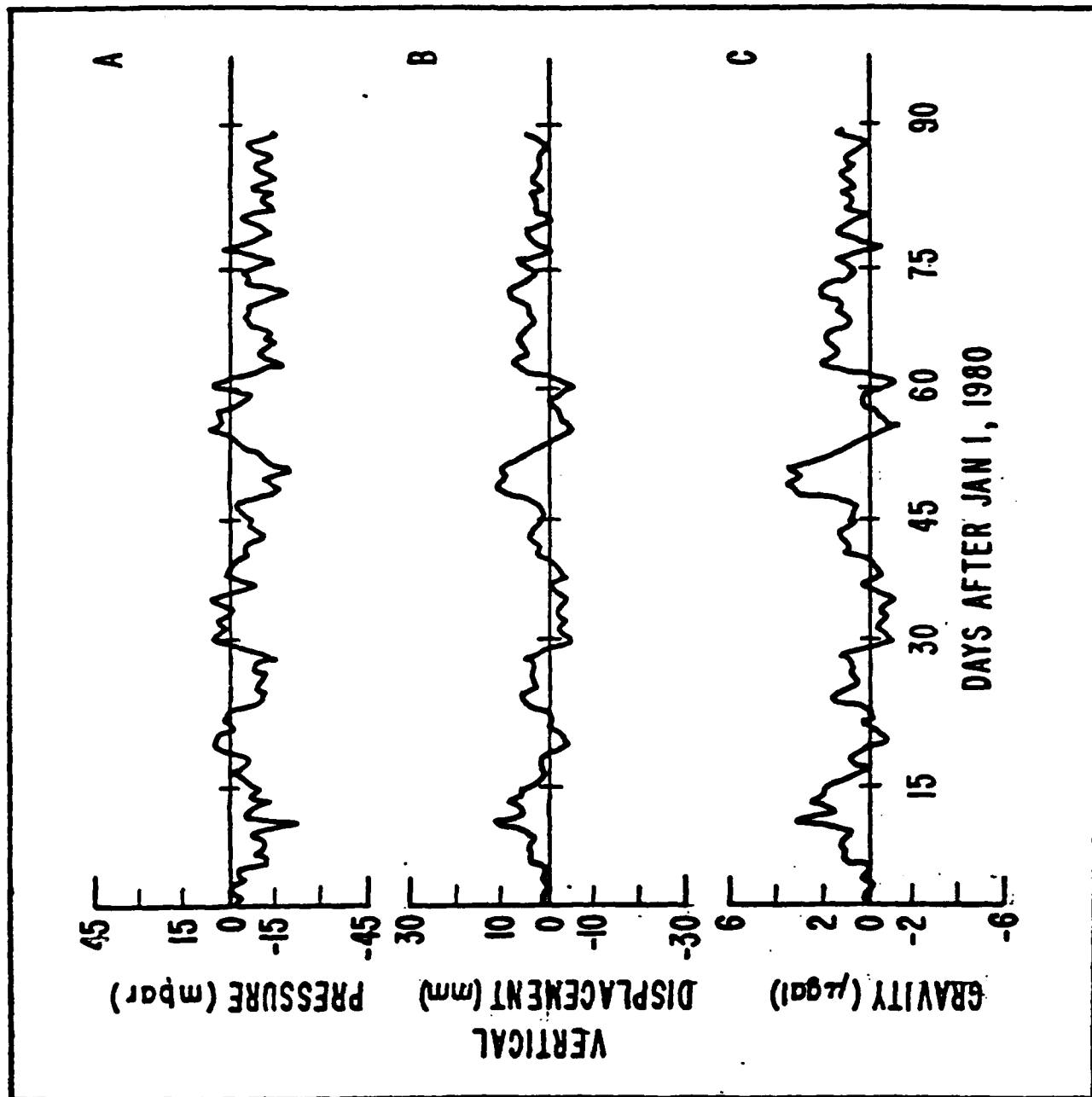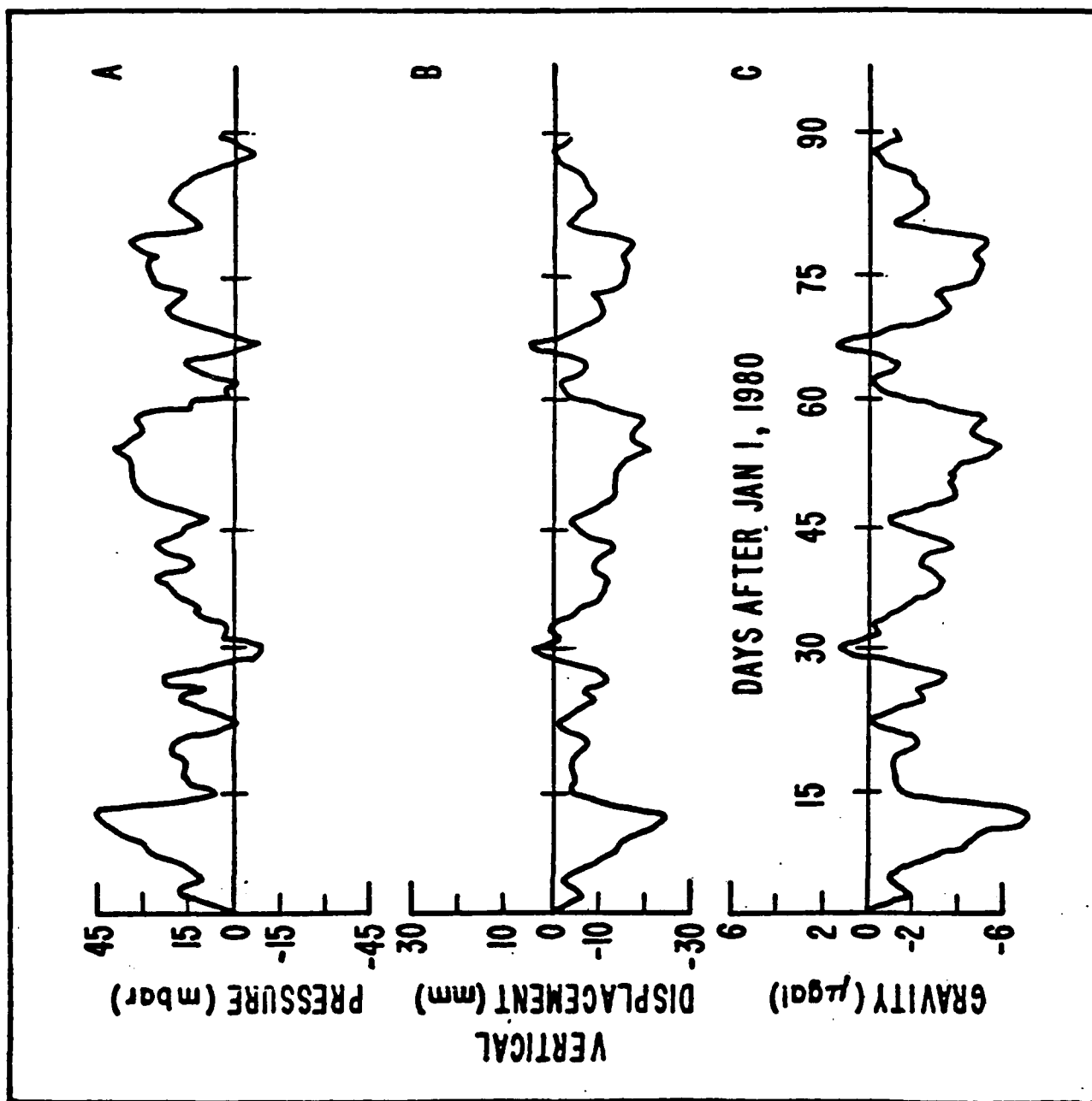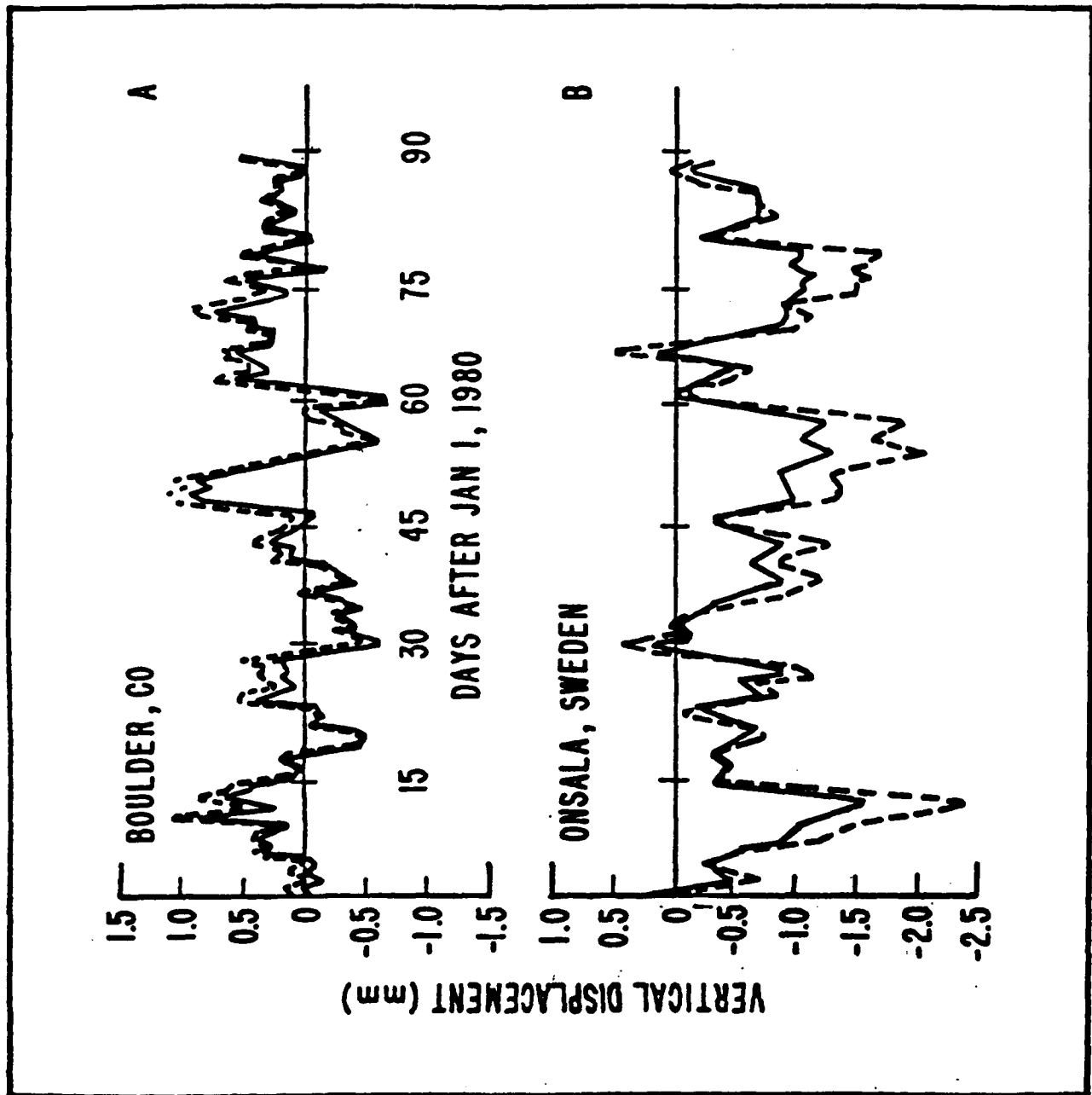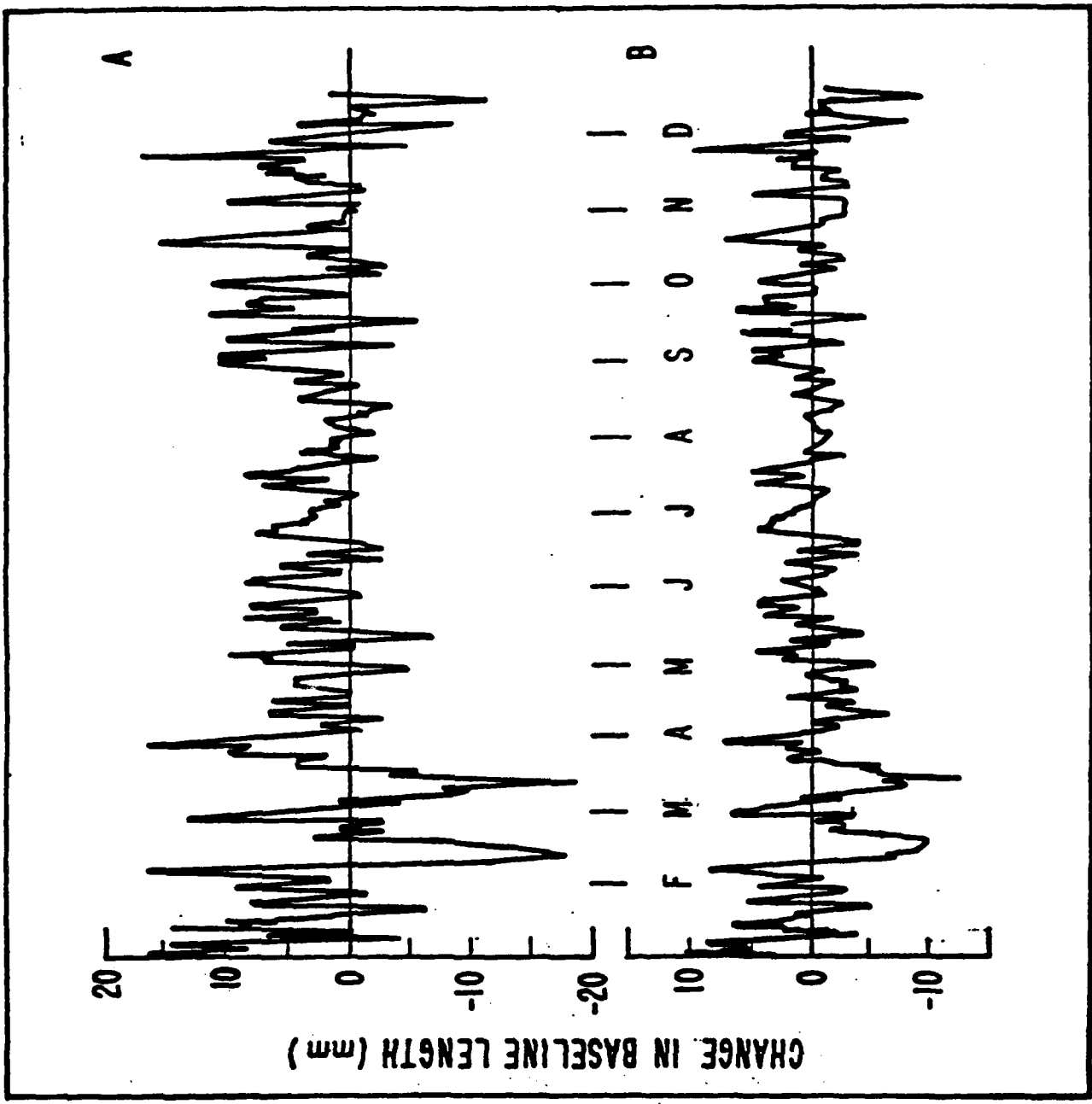
Figure II.1

Figure II.2

13

Figure II.3

14
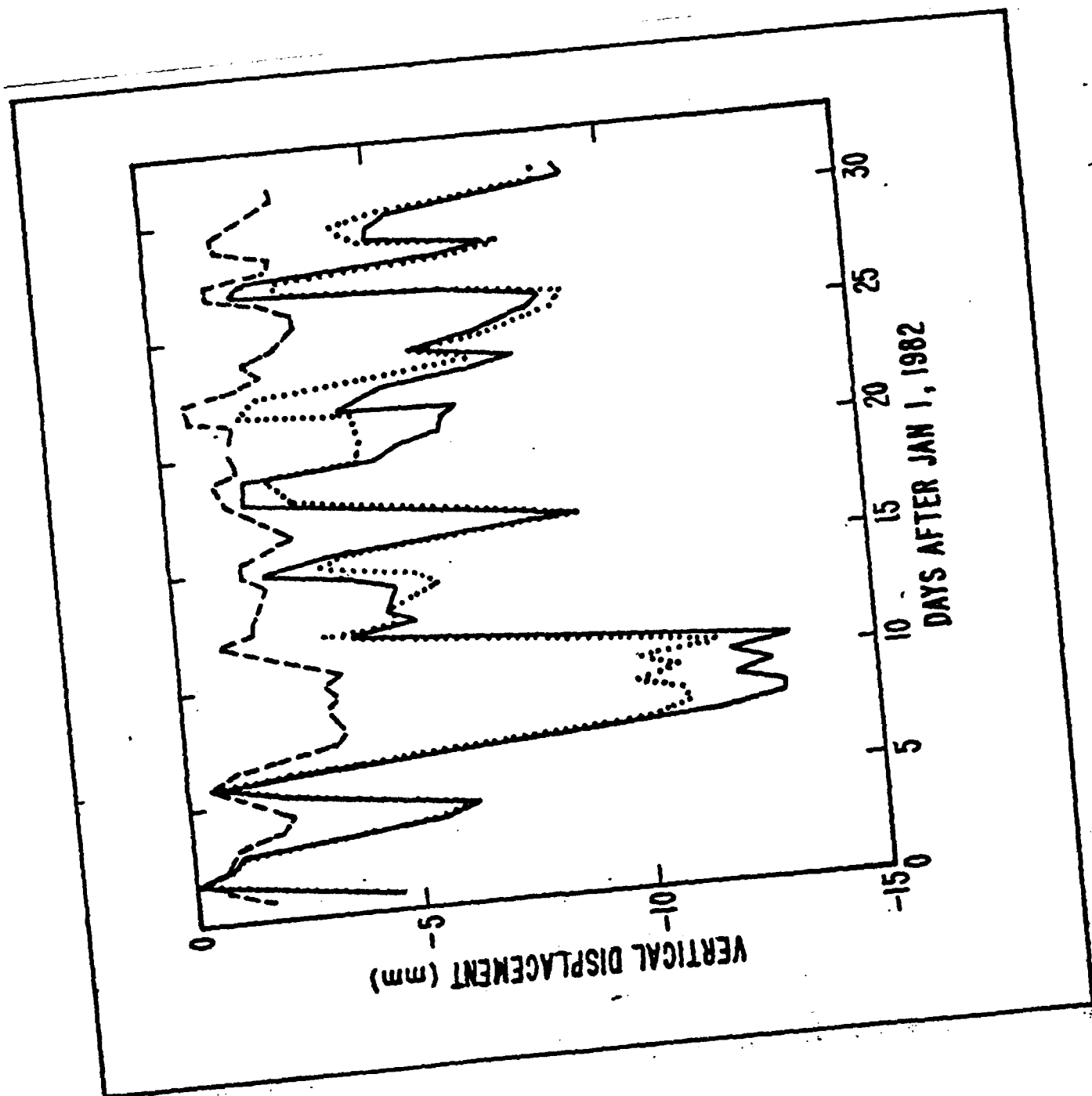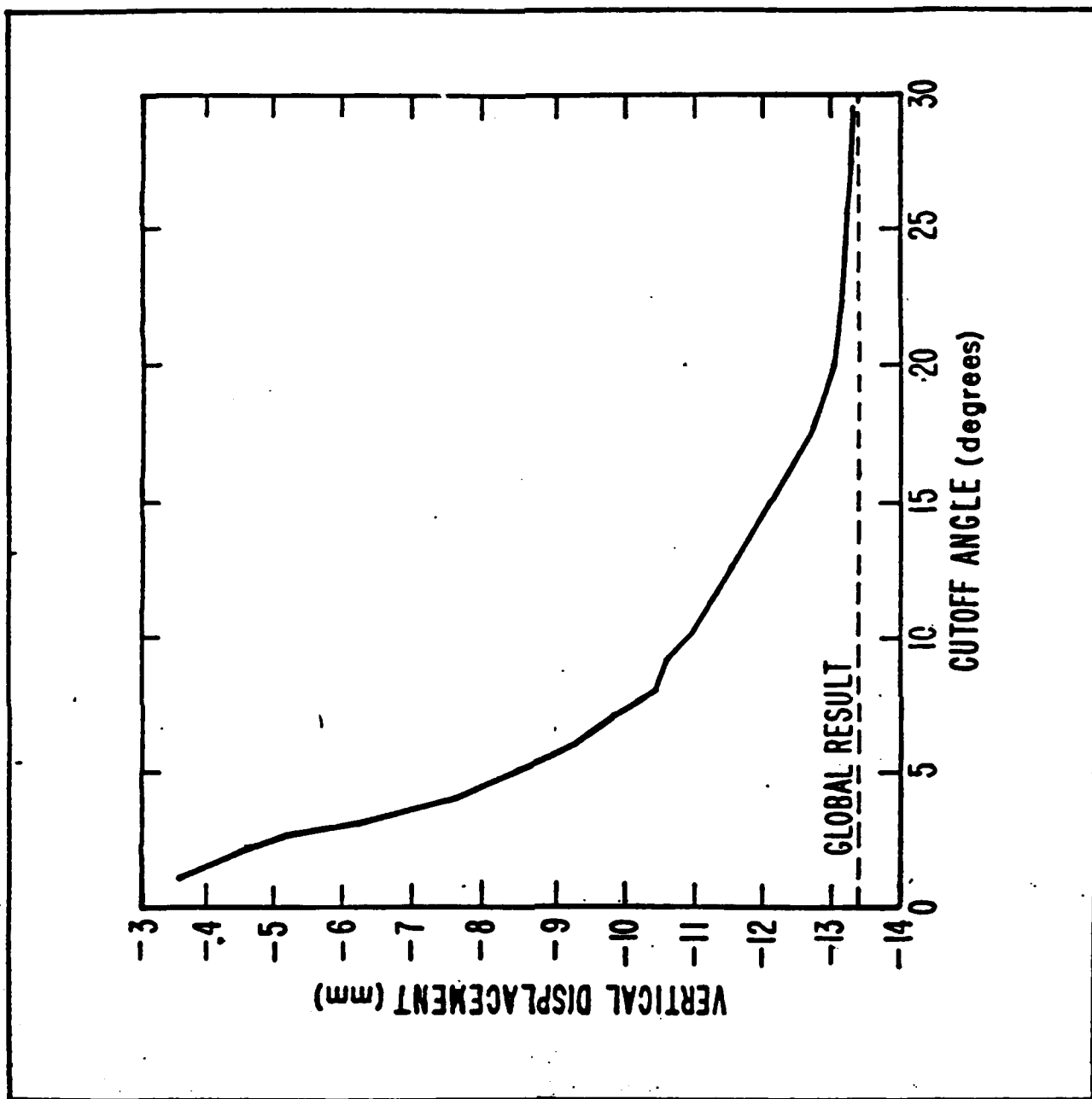
Figure II.4
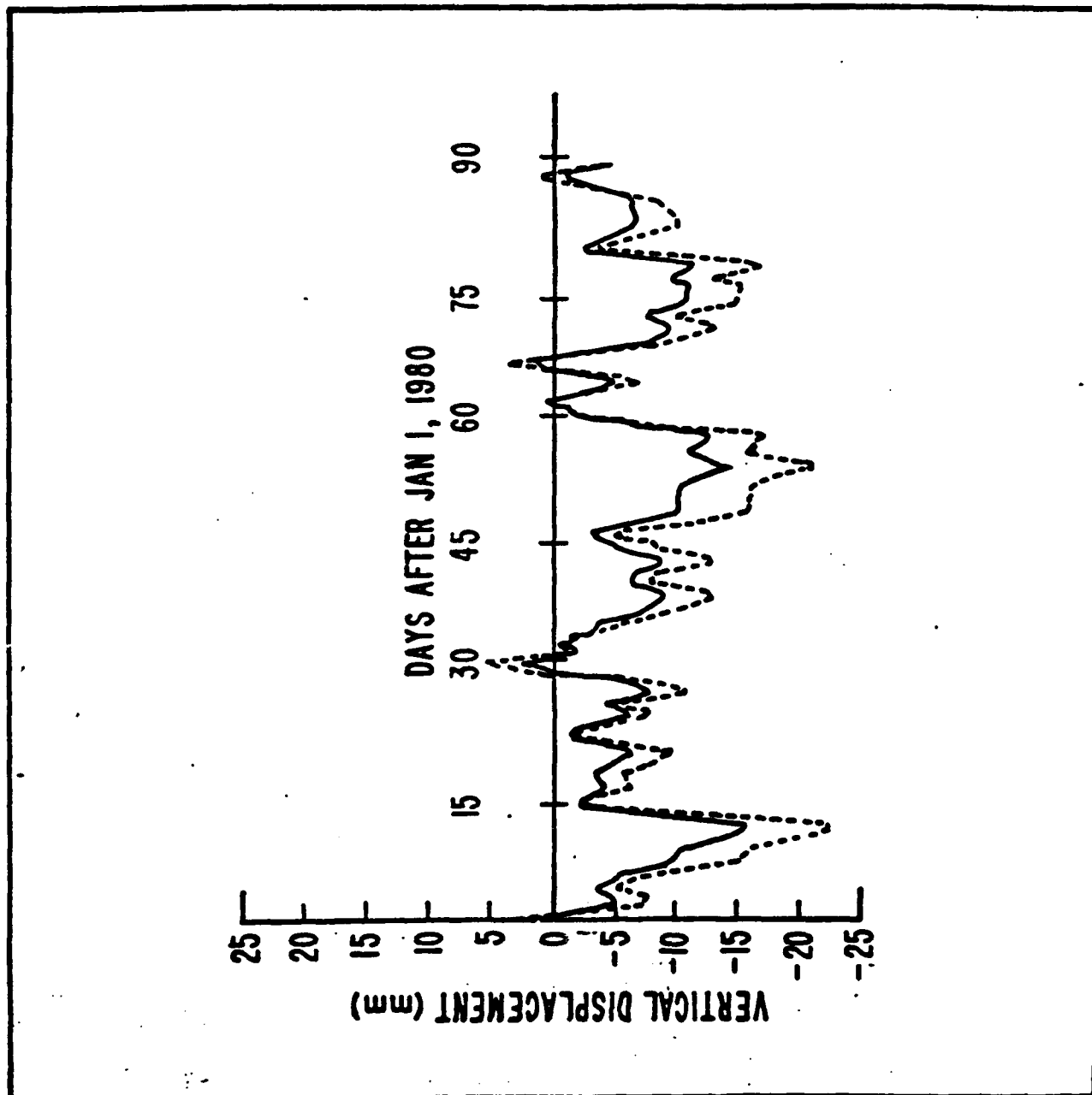
15

Figure II.5

16

Figure II.6

17

Figure II.7

18

CHAPTER III

THE EARTH'S FORCED NUTATIONS: GEOPHYSICAL IMPLICATIONS

INTRODUCTION

The Earth's nutational motion consists of periodic tipping of the Earth in space and is caused by the gravitational attraction of the Sun and Moon. The motion occurs at discrete frequencies of, as seen from the Earth, one cycle per day modulated by the orbital frequencies of the Sun and Moon. The periods are close to diurnal because the Sun and Moon rise and set once a day.

For many applications nutations are a nuisance since if they are not adequately removed they can degrade solutions for other parameters. However, recent observational results from Very-Long-Baseline-Interferometry (VLBI) have demonstrated that nutations can be important in their own right in providing a probe of the Earth's interior. In this chapter, we review nutation theories and, in an appendix, we extend those theories to include an Earth with a non-hydrostatic equilibrium state. We discuss the geophysical implications of the observational results.

A REVIEW OF THE THEORY

The goal of a nutation theory is to estimate the nutation amplitude as a function of frequency. The amplitude depends on frequency because the forcing from the Sun and Moon depends on frequency, and because the Earth's response to forcing is different at different frequencies. Finding the forcing as a function of frequency (in fact, finding the frequencies themselves) is a celestial mechanics problem, and requires accurate solutions for the orbital motion of the Moon and Earth [Kinoshita, 1977]. Modelling the Earth's response as a function of frequency is a geophysical problem, and it is that problem that will be addressed in this chapter.

The gravitational potential energy from the Sun and Moon can be expanded in Earth-based coordinates as a sum of complex spherical harmonics (Y_l^m). Each coefficient in that sum can be further expanded as a sum of terms which vary harmonically with time. Only Y_2^1 terms contribute to the nutational motion. We write an individual Y_2^1 term as

$$V = f(\omega)e^{i\omega t}r^2 Y_2^1(\theta,\lambda) \tag{1}$$

where ω is the frequency, θ and λ are the co-latitude and eastward longitude, $f(\omega)$ is a scalar amplitude, and Y_2^1 is normalized so that the integral of $|Y_2^1|^2$ over the unit sphere is 1. The values of ω and $f(\omega)$ are determined by the orbital motion.

Under very general conditions, the response of the Earth to the potential (1) can be expanded as a sum of the Earth's normal mode eigenfunctions [Wahr, 1981a], so that the nutation amplitude, ζ is

$$\zeta = e^{i\omega t}\sum_i \frac{B_i}{\omega-\omega_i} \tag{2}$$

Here, the sum over i is over all normal modes, ω_i is the eigenfrequency of the i'th mode, and B_i depends on the i'th eigenfunction and (linearly) on f. One implication of (2) is that the amplitude is large if the forcing frequency, ω, is close to an eigenfrequency.

Although the sum in (2) is, in principle, over every one of the Earth's normal modes, almost all of the important contributions come from just two modes, both with frequencies in the diurnal band. One of these modes, called the tilt-over-mode (TOM), is simply a tipping of the Earth in space with no associated deformation. The motion is exactly equivalent to tipping the coordinate system in the opposite direction. The period of the TOM is infinite as seen from non-rotating inertial space, and so is

19

exactly one sidereal day as seen from a sidereally rotating system.

The more interesting of the two diurnal modes contributing to (2) is the free core nutation (FCN). This mode involves tipping the mantle and fluid core in opposite directions. Because the core-mantle boundary is not exactly spherical, the mantle and core push against each other when they tip, and the resulting pressure acts to restore the core and mantle to their untipped state. There are also gravitational restoring forces due to the interaction between the aspherical density distributions of the core and mantle. The result is a free periodic motion, the FCN, with a frequency equal to one cycle per day plus a small term dependent on the strength of the core-mantle coupling. That coupling depends on the aspherical shape and density distribution of the core, as described below. For an Earth where the shape and density are assumed to be consistent with a state of hydrostatic pre-stress, the frequency is ω_{FCN} = 1+1/460 c/d [Wahr, 1981b].

The TOM contributions to the nutation amplitudes in (2) are much larger than the FCN contributions. The reason is that for the TOM, the factor B_i in (2) depends on the total torque on the Earth from the Sun and Moon at the frequency ω. For the FCN, B_i is sensitive, instead, to the difference between the torques per unit moment of inertia, acting on the core and mantle (and to deformation terms of about the same order). The Sun and Moon do not provide nearly as large a differential torque as they do a total torque.

The TOM contributions are not particularly interesting. The TOM resonance merely reflects the fact that the longer (as seen from inertial space) you torque an object, the more it tips. The FCN contributions, though, are of geophysical importance since they are sensitive to the poorly known shape and aspherical density distribution of the core. To consider those contributions in detail, it is usual to remove the TOM contribution from the sum in (2), and then to divide the remainder by the TOM contribution. This last division removes the scalar amplitude, $f(\omega)$, from the remainder, so that the results reflect only the geophysically interesting part of the signal. This normalized "admittance" is shown in Figures III.1 and III.2 as a function of frequency. The theoretical results (the solid line) use eigenfrequencies and eigenfunctions computed for a hydrostatically pre-stressed Earth. Although the results shown are computed using several modes in the sum (2) [Wahr, 1981b], almost all of the contributions come from the FCN. The resonance at the FCN eigenfrequency of 1+1/460 c/d is clearly evident.

Also shown in Figures III.1 and III.2 are recent VLBI observational results [Herring et al., 1986] for the nutation amplitudes at a few important frequencies. The TOM resonance has been removed from the observational results and then divided into the remainder, in order to compare with the theoretical results (the observations have also been corrected for the effects of oceans as described below). The vertical bars on the observational results reflect the published errors.

The agreement between the theory and the observations is, in general, good. The disagreement at the prograde fortnightly frequency is observationally significant but, in absolute terms, is only a few tenths of a milli-arcsecond. The agreement at the prograde semi-annual frequency looks from Figure III.1 to be reasonably good, but, as we shall see below, there could be a disagreement of up to 1 milli-arcsecond after correcting for mantle anelasticity and non-hydrostatic core structure.

First, however, there is an even larger discrepancy at the retrograde annual frequency (see the enlarged comparison in Figure III.2). The observed annual admittance lies well above the theoretical result, and the difference in absolute terms is about 2 milli-arcseconds. The results in Figures III.1 and III.2 suggest that the FCN eigenfrequency should be larger than the value of 1+1/460 c/d predicted using the hydrostatic assumption. In fact, Gwinn, et al. [1986] used the observational results to conclude that ω_{FCN} = 1+1/433 c/d. (Although the annual discrepancy could also be resolved by adjusting the FCN value of B_i in (2), that adjustment would cause substantial discrepancies at other frequencies.)

What does this increase in eigenfrequency imply about the Earth? The theoretical results shown in Figures III.1 and III.2 do not include the effects of oceans (although the observational results have been corrected for the oceans), of mantle anelasticity, or of non-hydrostatic pre-stress and structure. These effects are discussed below.

20

The Oceans

Oceans affect nutation amplitudes through surface loading. The Sun and Moon cause diurnal tides in the oceans at exactly the nutation periods. Those ocean tides load the Earth and cause further nutational motion. Thus, the effects of oceans can be perceived as modifying the driving force for nutations. In that case, the force can no longer be written in terms of a Y_2^1 potential, as in (1). Oceanic corrections require some understanding of the loading force, and that requires, at the very least, reliable ocean tide models. Wahr and Sasao [1981] used diurnal tide models to estimate the oceanic corrections, and their results have been removed from the VLBI observations to give the results shown in Figures III.1 and III.2.

Mantle Anelasticity

Mantle anelasticity and non-hydrostatic structure affect the nutations by modifying the Earth's response to external forcing, rather than by contributing to the forcing itself. To understand their contributions, it is necessary to describe nutation models in more detail.

Existing nutation models fall into two categories, referred to here as numerical and semi-analytical. Both types of models involve the solution of the same infinite set of coupled ordinary differential equations. And, both types of models derive approximate solutions by truncating the equations. In the numerical method [Wahr, 1981b; see also Smith, 1977] the truncation is less severe and more terms are kept than in the semi-analytical method (see, for example, Jeffreys and Vicente [1957]; Molodensky [1961]; Sasao et al. [1980]). Thus, the advantage of the numerical method is that it is apt to be more accurate. The advantages of the semi-analytical methods are (1) they are easier to implement; and (2) the results are more readily understood in terms of the Earth's physical parameters. Furthermore, the results from the semi-analytical models appear to agree well with those from the numerical method.

The semi-analytical results of Sasao et al. [1980] for B_{FCN} and ω_{FCN} are:

$$B_{FCN} = -\sqrt{15/2\pi}\ \frac{A_f}{A_m}\ (e-\gamma)\frac{f(\omega)}{\Omega} \tag{3}$$

$$\omega_{FCN} = \left[1+\frac{A}{A_m}\ (e_f-\beta)\right]\Omega \tag{4}$$

where A, A_f, A_m are the equatorial moments of inertia of the Earth, core, and mantle; $e = (C-A)/A$ and $e_f = (C_f-A_f)/A_f$ are the dynamical ellipticities of the Earth and core (C and C_f are the polar moments of inertia of the Earth and core); and γ and β represent the effects of deformation within the mantle and core ($\gamma<e$ and $\beta<e_f$). The results shown in (3) and (4) were derived by Sasao, et al. [1980] assuming the inner core is fluid, and that the Earth's equilibrium state is one of hydrostatic pre-stress.

Mantle anelasticity affects these results by modifying γ and β. Those parameters become complex, leading to phase lags in the nutations. Even larger are the effects on the real part of those parameters. The main source of uncertainty when modelling the anelastic corrections is the uncertainty in mantle Q at diurnal periods. Seismic information is pertinent to much shorter periods. On the other hand, this suggests that perhaps the nutation results could be used to learn about mantle Q in this frequency regime.

Wahr and Bergen [1986] and Dehant [1988] used a variety of anelastic models and assumptions to estimate the effects on nutation amplitudes. They found that, in general, the contributions to B_{FCN} in (2) were more important than the contributions to ω_{FCN}. The model results shown in Figures III.1 and III.2 are corrected for Wahr and Bergen's anelastic estimates and the results are shown in Figures III.3 and III.4. Also shown, in Figure III.5, is a comparison between the out-of-phase components inferred from the VLBI results (corrected for the effects of oceans) and the predicted results due to anelasticity. For a dissipationless Earth, the out-of-phase components would be zero. The vertical bars associated with the anelastic results in these figures reflect the uncertainty in the value of mantle Q at diurnal periods. The figures suggest that the present VLBI results are, in principle, nearly accurate enough to

21

discriminate between various mantle Q results. However, the effects of anelasticity do not resolve the disagreements between the observations and the theory. In fact, they tend to make the agreement for the in-phase amplitudes (Figs. 3 and 4) worse. Thus, before the nutation results can be used to learn about anelasticity, it will first be necessary to understand the reasons for the large discrepancy.

Non-hydrostatic Structure

The most likely explanation for the difference between the observed and theoretical ω_{FCN} is that the Earth is not hydrostatically pre-stressed. In the Appendix, we extend the semi-analytical model of Sasao et al. to include an Earth which is not hydrostatically pre-stressed (although we, too, assume the inner core is fluid). In particular, the core-mantle boundary and density distribution within the Earth can have an arbitrary spherical harmonic expansion. We find, though, that B_{FCN} and ω_{FCN} are still given by equations (3) and (4). Thus, the effect of the non-hydrostatic pre-stress on ω_{FCN} can be computed by estimating the non-hydrostatic contributions to e_f in (4). Since e_f depends only on the Y_2^0 spherical harmonic components of the core-mantle boundary shape and of the core's internal density, the observational results for ω_{FCN} constrain only those particular spherical harmonic coefficients.

The VLBI results for ω_{FCN} suggest that e_f is about 5% larger than the hydrostatic value [Gwinn et al., 1986]. Suppose the radius of the core-mantle boundary as a function of θ and λ is

$$r(\theta,\lambda) = a \left[1 + \sum_{l=1}^{m=l} \sum_{m=-l} a_l^m Y_l^m(\theta,\lambda) \right] \tag{5}$$

where a is the mean core radius, and the Y_l^m are normalized so that the integral of $|Y_l^m|^2$ over the unit sphere is 1. We have found numerically [J. Wahr and D. de Vries, unpublished manuscript], that unless there is a thin, low density boundary layer at the top of the core, e_f is approximately equal to the ellipticity of the core mantle boundary, ε_c, where $a_2^0 = -(2/3)\varepsilon_c$. (If there is a low density boundary layer, then e_f could also depend critically on the shapes of the equi-density surfaces inside the core.) Thus, in the absence of such a boundary layer, the nutation results constrain the Y_2^0 component of the boundary. They imply, in fact, that ε_c is about 5% larger than the hydrostatic value, and suggest a non-hydrostatic topography on the boundary of about 1/2 km.

When the value $\omega_{FCN} = 1 + 1/433$ c/d is used in (2) in place of the hydrostatic result $1 + 1/460$ c/d, large differences occur at other frequencies, as well. For example [Gwinn, et al., 1986], the theoretical retrograde 18.6-year amplitude is decreased relative to the IAU adopted value by about 2 milli-arcsecond. This amplitude is also decreased by about 1 milli-arcsecond due to the oceans and about .5 milli-arcsecond by anelasticity.

The theoretical prograde six-month term is increased by about .4 milli-arcseconds due to the change in ω_{FCN}. In fact, the VLBI result for this term disagrees with the theoretical amplitude by about 1 milli-arcsecond, after correcting for the effects of the oceans and anelasticity, and using $\omega_{FCN} = 1 + 1/433$ c/d. Similarly, there is a discrepancy for the prograde fortnightly term of about .3 milli-arcseconds between the VLBI results and the adjusted theory. It is not clear, at present, what is responsible for the fortnightly and semi-annual discrepancies.

CHAPTER III REFERENCES

Dahlen, F.A., *Geophys. J. Roy. Astr. Soc.*, **32**, 203, 1973.

Dehant, V., in *Earth Rotation and Reference Frames*, eds. Babcock, A., and G.A. Wilkins, 1988.

Gwinn, C.R., T.A. Herring, and I.I. Shapiro, *J. Geophys. Res.*, **91**, 4755, 1986.

Herring, T.A., C.R. Gwinn, and I.I. Shapiro, *J. Geophys. Res.*, **91**, 4745, 1986.

Jeffreys, H., and R.O. Vicente, *Mon. Not. R. Astr. Soc.* **117**, 162, 1957.

Kinoshita, H., *Cel. Mech.*, **15**, 277, 1977.

Lieske, J., T. Lederle, W. Fricke, and B. Morando, *Astron. Astrophys.*, **58**, 1, 1977.

Molodensky, M.S., *Commun. Obs. R. Belg.*, **288** , 25, 1961.

Saito, M., *J. Phys. Earth*, **22**, 123, 1974.

Sasao, T., S. Okubo, and M. Saito, in *Proceedings of IAU Symposium no. 78 "Nutation and the Earth's Rotation"*, eds. Fedorov, E., M. Smith, and P. Bender, D. Reidel Publishing Co., Dordrecht, 1980.

Smith, M.L., *Geophys. J. Roy. Astr. Soc.*, **50**, 103, 1977.

Smith, M.L., and F.A. Dahlen, *Geophys. J. Roy. Astr. Soc.*, **64**, 223, 1981.

Wahr, J.M., *Geophys. J. Roy. Astr. Soc.*, **64**, 651, 1981a.

Wahr, J.M., *Geophys. J. Roy. Astr. Soc.*, **64**, 705, 1981b.

Wahr, J.M. and T. Sasao, *Geophys. J. Roy. Astr. Soc.*, **64**, 747, 1981.

Wahr, J., and Z. Bergen, *Geophys. J. Roy. Astr. Soc.*, **87**, 633, 1986.

Wahr, J., and D. de Vries, *Geophys. J. Roy. Astr. Soc.*, 1989 (submitted).

Woodhouse, J.H., and F.A. Dahlen, *Geophys. J. Roy. Astr. Soc.*, **53**, 335, 1978.

CHAPTER III APPENDIX: Nutation Amplitudes for a
Non-hydrostatically Pre-stressed Earth

Previous nutation models have assumed the Earth is hydrostatically pre-stressed. Among the implications of this assumption is that the core-mantle boundary and all surfaces of constant density within the core and mantle are elliptical. Thus, the departure of those surfaces from spherical symmetry is proportional to the single spherical harmonic $Y_2^0(\theta,\lambda)$.

It is quite likely, though, that surfaces of constant density in the Earth and surfaces of discontinuity, such as the core-mantle boundary, have non-hydrostatic shapes. The Y_2^0 components of these surfaces are apt to differ from the hydrostatic values, and there are apt to be components with other Y_l^m angular dependence. Since the FCN is critically dependent on pressure coupling acting across the core-mantle boundary (and, to a lesser extent, gravitational coupling between the core and mantle), the FCN contribution to the eigenfunction expansion (2) could be affected.

In this appendix, the FCN contribution is modelled without assuming hydrostatic equilibrium in the mantle. Instead, the mantle is allowed to possess a small, arbitrary deviatoric pre-stress, and so surfaces of constant material properties and surfaces of discontinuity (such as the core/mantle boundary) within the mantle can have arbitrary shape. The core, however, is not permitted to have a deviatoric pre-stress (the core, after all, is a fluid even at seismic periods). As a result, the density distribution in the core is uniquely determined by the shape of the core-mantle boundary and by the gravitational potential from the mantle acting on the core. Thus, the constant density surfaces in the core need not coincide with the surfaces predicted for an everywhere hydrostatically pre-stressed Earth. The derivation, below, extends the semi-analytical model of Sasao, et al. [1980] to include these non-hydrostatic modifications, and to more fully justify a number of the necessary approximations. As in the model of Sasao, et al. [1980], we assume the inner core is fluid.

Consider a reference frame fixed to the mantle and rotating with it. For nutational motion at frequency ω, the rotation vector of the frame is defined as $\Omega\hat{z} + \Omega m_o(\hat{x}+i\hat{y})e^{i\omega t}$, where the nutational motion of the mantle is described by m_o, and where $m_o \ll 1$. For the forced nutations, the ratio $(\omega-\Omega)/\Omega$ is small. We will consider this ratio to be first order in ε, where ε is some measure of the departure of the Earth from spherical symmetry. This assumption is reasonable for the annual nutations (the terms with the largest discrepancy between theory and observation), where $|(\omega-\Omega)/\Omega| \cong 1/365$. It is less accurate for the fortnightly nutations, where $|(\omega-\Omega)/\Omega| \cong 1/13.7$.

Denote the luni-solar tidal force by $-\rho\nabla V$, where V is the luni-solar tidal potential given by equation (1) in the text. The equations of motion in the hydrostatically pre-stressed core are [Sasao, et al.,

$$\rho[-\omega^2 s + 2^i \omega \Omega \times s] = -\rho \nabla(\phi_1 + V) - \nabla P_E - \rho_1 \nabla \Phi - \Omega^2 \rho m_0 [(\hat{x} + i\,\hat{y})z\,(\Omega - \omega)$$
$$+\hat{z}(x + iy)(\Omega + \omega)] \tag{A1}$$
$$\nabla^2 \phi_1 = 4\pi G \rho_1$$

where s is the displacement field in the core; ϕ_1, P_E, and ρ_1 are the Eulerian perturbations in gravitational potential energy, pressure, and density, respectively; $\Omega = \Omega\hat{z}$ is the mean rotation vector of the Earth; and ρ and Φ are the initial density and total potential energy (gravitational plus centrifugal) and can have arbitrary angular dependence, except that surfaces of constant ρ must be surfaces of constant Φ in the core. There are, also, equations relating ρ_1 and P_E to s, which are not shown here. And, there are similar, although more complicated, differential equations describing displacements in the mantle, which are also omitted here. The mantle equations must explicitly include any assumed non-hydrostatic pre-stress (see Woodhouse and Dahlen [1978] for the complete mantle and core equations and for the boundary conditions).

For nutational motion, the displacement field in the core has the form

$$s(r) = \Omega\theta_0(\hat{x} + i\,\hat{y}) \times r + s_d(r) \tag{A2}$$

where θ_0 represents the mean nutational motion relative to the mantle, and s_d, which represents the deformation of the core, is first order in ε compared with the θ_0 term (see, for example, Sasao, et al. [1980]). Taking $(\hat{x} - i\,\hat{y}) \cdot [r \times (\text{equation}(A1))]$ and integrating through the core, and using (A2) for s, gives an angular momentum equation for the core:

$$2i\Omega^2 A_f m_0 + 2\omega\Omega^2 A_f \theta_0 \frac{\Omega - \omega}{\Omega}$$
$$= (\hat{x} - i\,\hat{y}) \cdot \int_{core} r \times \left[-\rho\nabla(\phi_1 + V) - \nabla P_E - \rho_1 \nabla \Phi \right] . \tag{A3}$$

Here, A_f is the core's principal moment of inertia in the equatorial plane; and $c^f_- = c^f_{13} - ic^f_{23}$, where the c^f_{ij} are perturbations in the core's inertia tensor due both to the deformational displacements, s_d, and to the rotational motion, θ_0 (the components of the inertia tensor change when the aspherical core is rotated with respect to the coordinate system). The terms on the right hand side of (A3) include the pressure and gravitational torques on the core from the mantle, and the gravitational torque on the core from the luni-solar tidal force.

All terms in (A3) are second order in ε relative to θ_0. As an example, ϕ_1 has contributions from the deformation, s_d, and from the rotational motion, described by θ_0. The contributions to ϕ_1 from the deformation are first order, because s_d is first order. The contributions from θ_0 are caused by rotating the Earth's unperturbed gravity field through the angle θ_0. These rotational contributions are also first order, because there is no change in gravity if the unperturbed field is spherically symmetric. Thus, ϕ_1 is a first order quantity. Furthermore, the integral of $\rho r \times \nabla\phi_1$ is 0 no matter what ϕ_1 is, if both the core shape and the internal density in the core are spherically symmetric. Thus, $\int_{core} r \times \rho \nabla\phi_1$ is second order.

As a second example, $\Omega\omega \equiv \Omega^2$ is a first order quantity (the unperturbed centrifugal force is order ε times the unperturbed gravitational force), as is $(\Omega - \omega)/\Omega$. Thus, the θ_0 term in (A3) is second order. And, as a third example, m_0 is first order compared with $\Omega\theta_0$ (m_0 represents motion of the mantle rotation axis as seen from the mantle and is of order $(\Omega - \omega)\theta_0$) so that $\Omega^2 m_0$ is second order. Finally, for completeness, we note here that V, P_E, ρ_1, Φ, and c^f_- are all first order relative to θ_0.

A comparable angular momentum equation for the entire Earth, after dropping all terms third order or smaller, is

$$2i\Omega^2 A m_0 = 2(\omega - \Omega) A_f \Omega^2 \theta_0 + \sqrt{15/2\pi}\, i\, (C - A)\, f\,(\omega) \tag{A4}$$

where C and A are the principal moments of inertia for the entire Earth, $f(\omega)$ is the scalar amplitude of the tidal potential (see equation (1) in the text), and the last term on the right hand side of (A4) represents the luni-solar torque on the Earth.

Next, c^ℓ_- and the right hand side of (A3) can be related to θ_o. Use (A2) in (A1) and separate the resulting vector equations into spheroidal and toroidal scalar equations. Similarly, separate the mantle differential equations and the boundary conditions into toroidal and spheroidal scalar equations. Then, consider only the spheroidal equations, ignore all terms in these equations that are second order or smaller in ϵ, and solve the entire system on a computer. In the core, for example, the first order spheroidal equations derived from (A1) are the scalar components of

$$\rho_0 \nabla(\phi_1 + V) + \nabla P_E + \rho_1 \nabla \Phi_0 = \left[i\, \theta_o \Omega^3 \sqrt{8\pi/15} \right] \rho_0 \nabla(r^2 Y^1_2) \tag{A5}$$

where ρ_0 and Φ_0 are the spherically symmetric parts of ρ and Φ. (One of the consequences of the truncation to first order is that m_o does not appear in (A5).)

The first order differential equations in the mantle corresponding to (A5) in the core, are the usual set of spheroidal equations describing tidal deformation of a spherical, non-rotating, static, and hydrostatically pre-stressed mantle (see, for example, Saito [1974]). Although, in principle, there is an apparent spheroidal force in the mantle which depends on m_o, that force is second order and so can be ignored in the first order deformation equations. All first order boundary conditions within the core and mantle and at the outer surface are also equivalent to the boundary conditions for a spherical, non-rotating, hydrostatically pre-stressed Earth.

In effect, then, all deformation terms can be computed by solving the static equations of motion for a spherical, non-rotating, hydrostatically pre-stressed Earth, subject to an apparent force proportional to $\rho_0 \nabla(r^2 Y^1_2)$, but with different proportionality constants in the core and mantle. In the core, the apparent force is proportional to θ_o and $f(\omega)$ (see (1) for a definition of $f(\omega)$). In the mantle, the apparent force is proportional only to $f(\omega)$. Neither the non-hydrostatic pre-stress in the mantle nor any of the Earth's aspherical structure enters explicitly into any of the first order deformation equations. Their effects are included only through the integrals on the right hand side of (A3).

Because the apparent force in the core is proportional to $\rho_0 \nabla(r^2 Y^1_2)$ and because the first order deformation equations are spherically symmetric, ρ_1, P_E, and ϕ_1 have $Y^1_2(\theta,\lambda)$ angular dependence. Using this angular dependence, (A5) yields directly

$$P_E(r,\theta,\lambda) = \rho_0(r) \left[\left[i\Omega^3 \theta_o \sqrt{8\pi/15} - f(\omega) \right] r^2 Y^1_2(\theta,\lambda) - \phi_1(r,\theta,\lambda) \right] \tag{A6}$$

$$\rho_1(r,\theta,\lambda) = \frac{\partial_r \rho_0(r)}{\partial_r \Phi_0(r)} \left[\phi_1(r,\theta,\lambda) + \left[f(\omega) - i\Omega^3 \theta_o \sqrt{8\pi/15} \right] r^2 Y^1_2(\theta,\lambda) \right] .$$

Using (A6) in (A3) and doing the integrals gives a result accurate to second order of

$$2i\Omega^2 m_o + 2\Omega^2 \theta_o(\Omega - \omega) + \frac{ic^\ell_- \Omega^2}{A_f} = -2\Omega^3 \theta_o e_f \tag{A7}$$

where $e_f = (C_f - A_f)/A_f$ is the dynamical ellipticity of the core (C_f is the polar moment of inertia of the core).

Define the dimensionless, real parameters β and γ so that

$$c^\ell_- = \beta 2A_f\, i\Omega\theta_o - \gamma A_f \sqrt{15/2\pi}\, f(\omega)/\Omega^2 . \tag{A8}$$

β and γ can be determined by solving the deformation equations on a computer. Using (A4) and (A8) in (A7) and solving for the core rotation angle θ_o, gives

$$\theta_o = \frac{i\sqrt{15/8\pi} \frac{A}{A_m}(e - \gamma)f(\omega)/\Omega^2}{\omega - \Omega\left[1 + \frac{A}{A_m}(e_f - \beta)\right]} \tag{A9}$$

where $e = (C - A)/A$ is, to lowest order, the dynamical ellipticity of the Earth, and A_m is the principal moment of inertia of the mantle.

The nutation amplitude observed at the Earth's outer surface is (see Sasao and Wahr [1981, eq. 3.20])

$$\zeta = \frac{\Omega}{\Omega-\omega}m_o . \tag{A10}$$

Using (A4) to relate m_o to θ_o, and (A9) to relate θ_o to $f(\omega)$, (A10) reduces to

$$\zeta = \left[\frac{\dfrac{e}{\Omega-\omega}}{\omega - \left[1 + \dfrac{A}{A_m}(e_f - \beta) \right]} \right] \sqrt{15/8\pi}\, \frac{f(\omega)}{\Omega} . \tag{A11}$$

The $e\Omega/(\Omega-\omega)$ term in (A11) represents the TOM resonance. The other term in (A11) is the FCN resonance, and can be written as $B_{FCN}/(\omega-\omega_{FCN})$, where B_{FCN} and ω_{FCN} are given by equations (3) and (4) in the text.

Although this result was derived here without assuming a hydrostatically pre-stressed mantle, it is identical in form to the hydrostatic result. The dynamical ellipticity, e_f, depends on the Y_2^0 component of the core-mantle boundary shape, and on the Y_2^0 terms in the density stratification inside the core. The dependence of ω_{FCN} on the internal density stratification is due to the effects of gravitational torques between the core and mantle, represented by the $\rho\nabla\phi_1$ and $\rho_1\nabla\phi$ terms on the right hand side of (A3). The dependence on the boundary structure is due to pressure torques at the core/mantle boundary, represented by the ∇P_E term in (A5). There is no dependence, to this order of approximation, on any other Y_l^m terms in the aspherical structure. Similarly, e depends on the Y_2^0 density structure throughout the Earth, and is well determined from independent observations of the Earth's precession (see, for example, Lieske et al. [1977]). The factors β and γ represent the effects of deformation and are insensitive, to this order, to aspherical structure. Sasao et al. [1980] found that β is about 25% of the hydrostatic value of e_f. For a hydrostatically pre-stressed Earth, $\omega_{FCN} \cong (1 + \frac{1}{460})$ cycles per day.

26

CHAPTER III FIGURE CAPTIONS

Figure III.1. A comparison between theoretical nutation results from Wahr (1981b) (solid line) and VLBI observational results from Herring, et al. (1986) (vertical bars). The results are normalized, as described in the text, to form admittances. The lengths of the vertical bars represent the observational errors.

Figure III.2. An expanded view of the 1+1/365 term in Figure III.1. There is significant disagreement between theory and observation. The discrepancy suggests the FCN eigenfrequency should be larger than the theoretical value.

Figure III.3. The theoretical nutation admittances for an anelastic Earth from Wahr and Bergen (1986). The vertical bars for the anelastic results reflect the uncertainty in mantle Q at diurnal periods. Also shown are the theoretical results for an elastic Earth (solid line) and the VLBI results.

Figure III.4. The anelastic admittance and observational result for the 1+1/365 nutation. Anelasticity worsens the agreement between observation and theory.

Figure III.5. The out-of-phase components for the nutations. Both the VLBI results (solid lines) corrected for the oceans and the anelastic contributions (dashed lines) are shown. The vertical bars for the anelastic results reflect uncertainty in mantle Q at diurnal periods. The out-of-phase components should be zero for a dissipationless Earth.
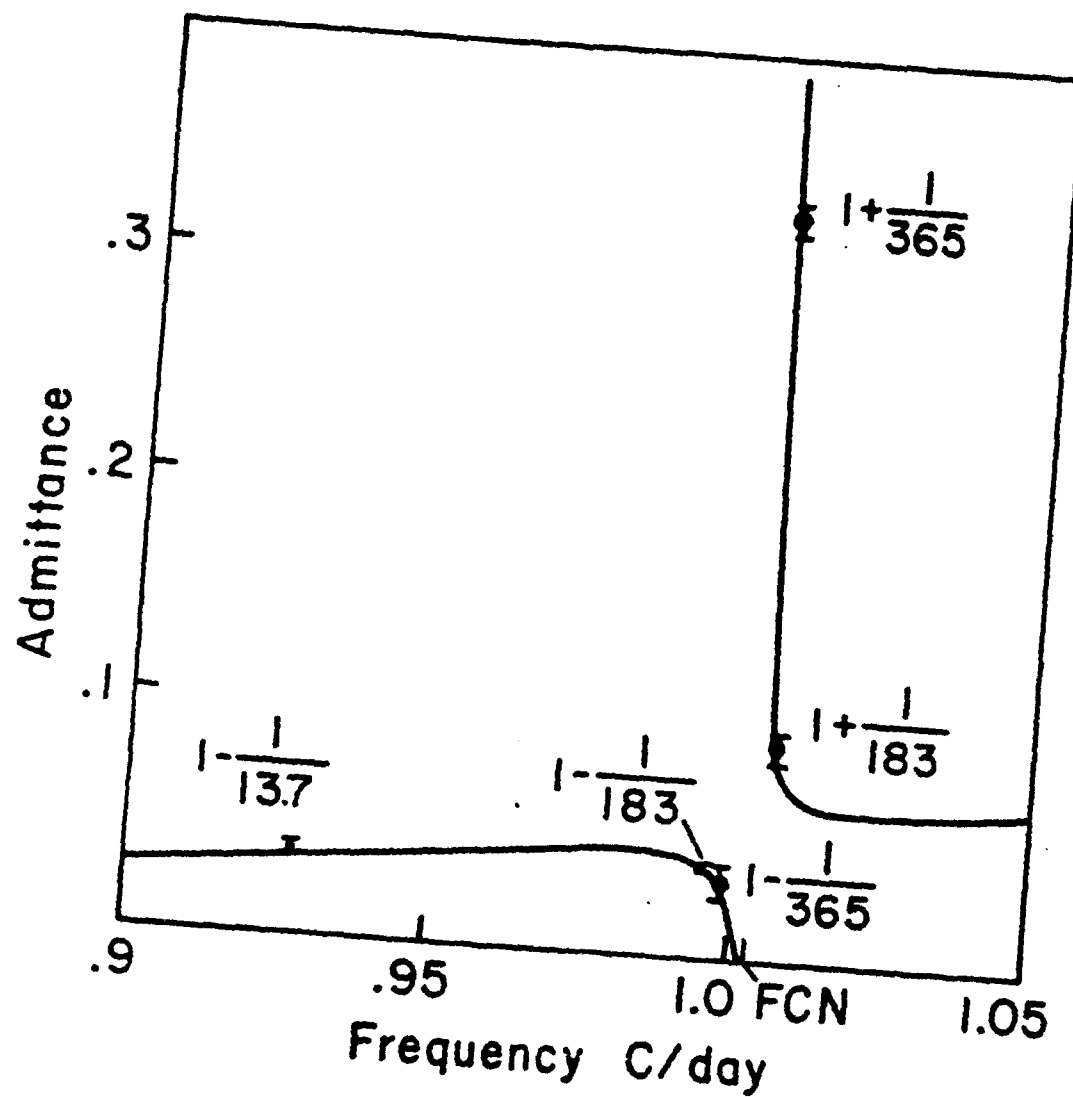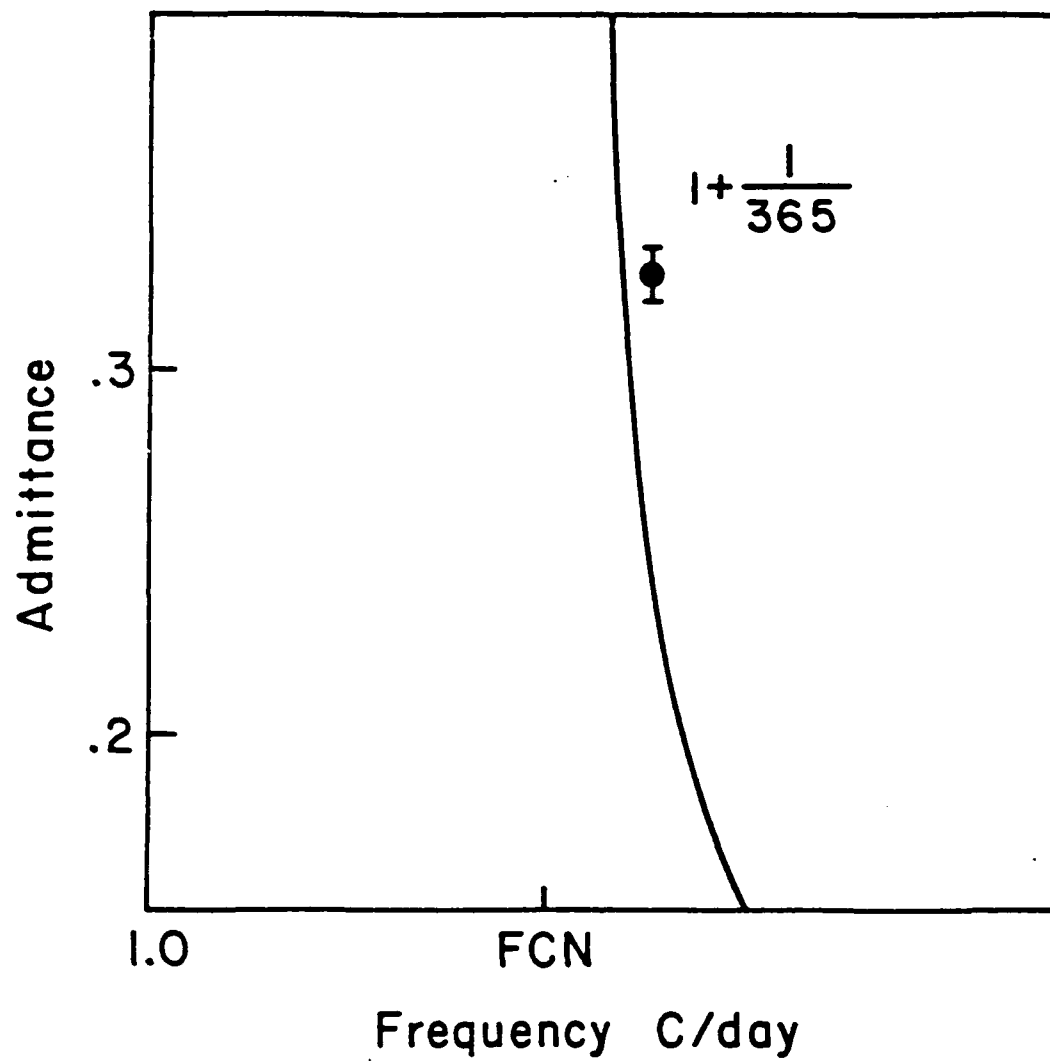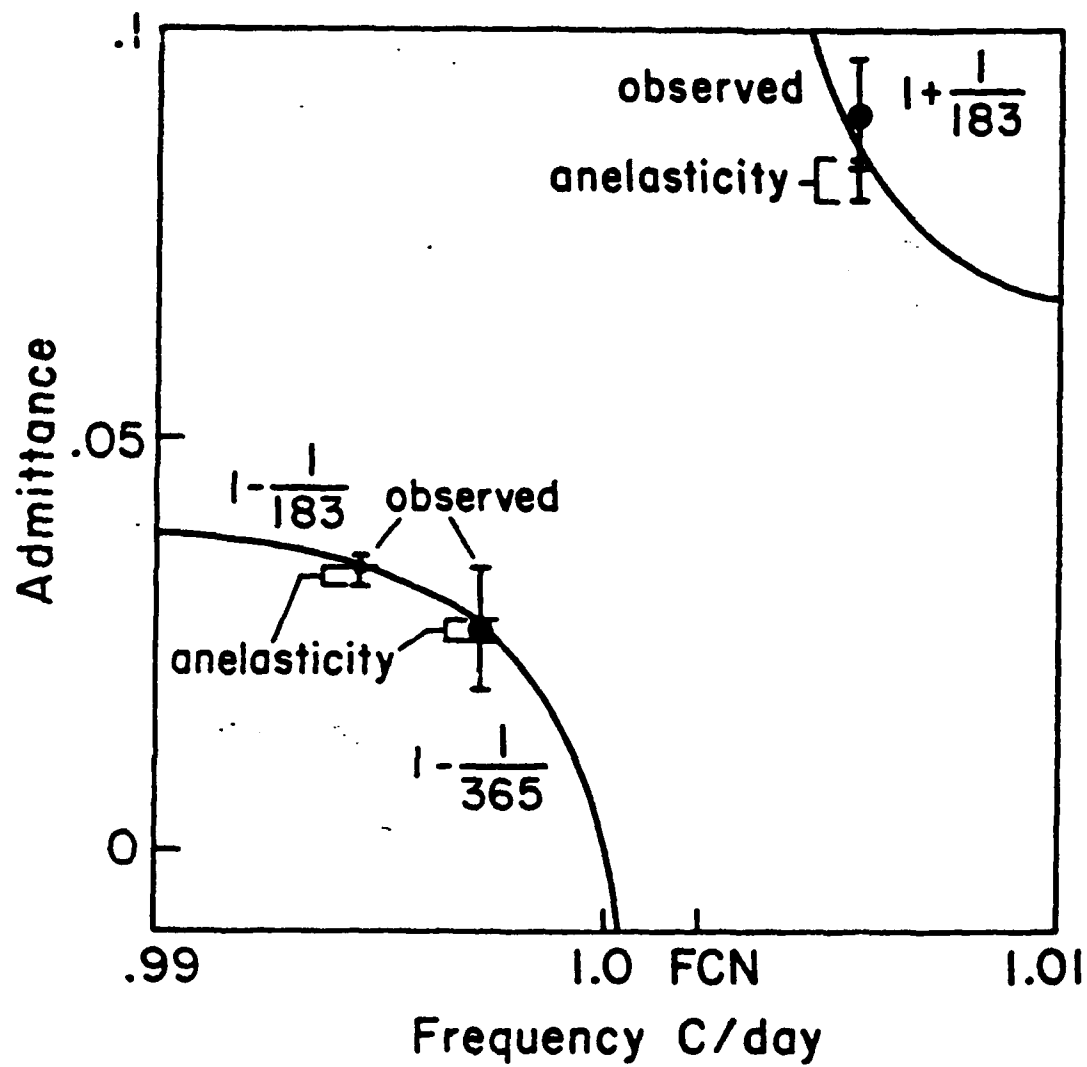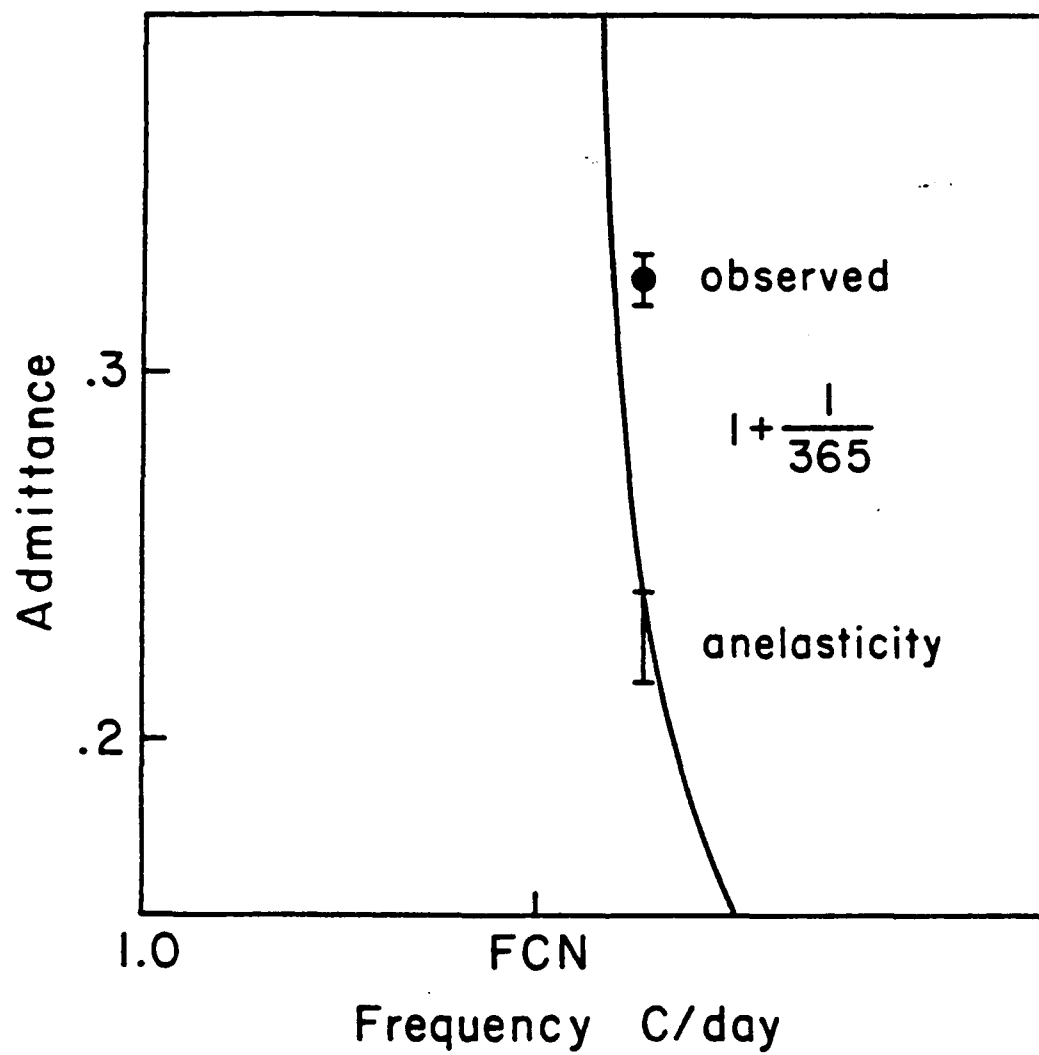
Figure III.1
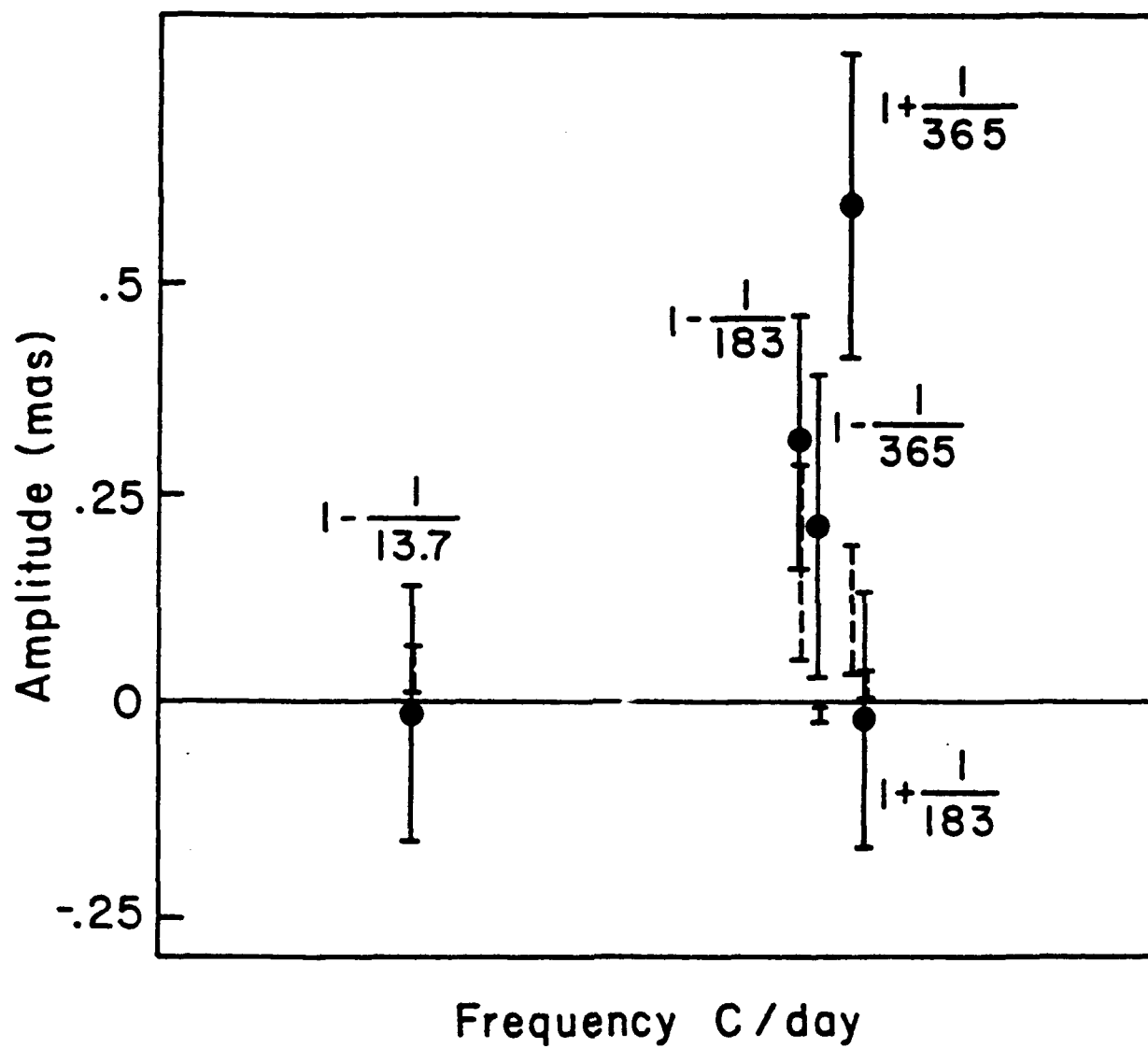
28

Figure III.2

Figure III.3

Figure III.4

31

Figure III.5

CHAPTER IV

THE POSSIBILITY OF LATERAL STRUCTURE INSIDE THE CORE AND ITS IMPLICATIONS FOR NUTATION AND EARTH TIDE OBSERVATIONS

SUMMARY

We show that there can be lateral structure inside the fluid core caused by gravitational forcing from the mantle, from the inner core, or from topography on the core/mantle or inner core/outer core boundaries. We describe a method for calculating the internal structure, given knowledge of the forcing. We discuss the possible effects of this structure on results for the core/mantle boundary topography inferred from observations of the earth's forced nutations and diurnal earth tides. We consider the possible implications of a thin, low density fluid layer at the top of the core.

1 INTRODUCTION

There has been considerable, recent effort in the geophysics community to understand more about the structure and the dynamical and material properties at the core/mantle boundary. Constraints on the boundary shape and on the near-boundary structure come from numerous sources, including seismic imaging with body waves [eg. Gudmundsson, et al., 1986; Creager and Jordan, 1986; Morelli and Dziewonski, 1987] and free oscillations [eg. Ritzwoller, et al, 1986; Giardini, et al, 1987], geoid modelling [eg. Hager, et. al., 1985; Forte and Peltier, 1987; Zhang and Yuen, 1987], and earth rotation and other geodetic studies [eg. Gwinn, et al, 1986; Levine, et al., 1986; Neuberg, et al., 1987; Wahr and de Vries, 1989; Hide, et al., 1989]. In many cases there is a possible ambiguity in the interpretation of the observations: do the data reflect the effects of core/mantle boundary topography alone, or are there also effects of structure within the core or lower mantle? Often, the possibility of lateral structure inside the core is simply ignored. (A comment on notation: the earth is primarily an ellipsoid, with ellipticity determined by the hydrostatic response of the earth to the centrifugal force associated with its rotation. Surfaces of constant density and boundary surfaces for a hydrostatic earth have the shape $r = r_0(1 + \varepsilon(r_0)Y_2^0(\theta,\lambda))$, where r_0 is the mean radius of the surface, $Y_2^0(\theta,\lambda)$ is a spherical harmonic, and θ and λ are the co-latitude and eastward longitude, respectively. The dimensionless function, $\varepsilon(r_0)$, is determined by solving Clairaut's differential equation - see, for example, Jeffreys [1976]. Throughout this chapter, the word "hydrostatic" will refer to this contribution to the earth's lateral stratification. The words "structure" and "topography" will denote the departure of a constant density surface and of a boundary, respectively, from the hydrostatic shape.)

Stevenson [1987] concludes that surfaces of constant material properties inside the fluid core should closely coincide with surfaces of constant potential, and his results have occasionally been invoked to justify the assumption of no internal structure. But, there is no guarantee that the constant potential surfaces are, themselves, free of structure. In fact, the structure of constant potential surfaces inside the core should partly reflect the topography at the core/mantle boundary. More precisely, the constant potential surfaces inside the fluid core can be modelled, as described below, from knowledge of the constant potential surfaces at the mean radii of the core/mantle and inner core/outer core boundaries. And, because of the density contrast across those boundaries, the potential at a boundary radius is affected by the boundary topography.

Depending on the type of observation and on the amplitude of the internal structure, the results of ignoring that structure when inverting for core/mantle boundary topography could be significant. For example, Wahr, et al. [1987] inverted core-phase travel times to infer the long wavelength spherical harmonic coefficients of the boundary topography for two cases. In one case, structure inside the core was ignored, which is equivalent to assuming that surfaces of constant potential inside the core coincide

with the hydrostatic surfaces. In the other case, the core/mantle boundary was assumed to be a surface of constant potential. In the latter case, the structure of the internal equipotential surfaces depends directly on the amplitude of the boundary topography (see section 2 below), and can be large for large topography. The boundary topography obtained by Wahr, et al. using core-refracted phases was substantially different for these two cases at the very longest wavelengths: ie. for the $Y_l^m(\theta,\lambda)$ spherical harmonic coefficients for $l \leq 3$. The coefficients were larger, sometimes by several times, for the case when the internal structure was included. The assumption that the boundary is an equipotential surface is likely to cause an overestimate of the internal structure (see below). Still, the effects of the assumed structure were large enough, particularly for inversions of PKIKP data, to suggest that the effects of more moderate internal structure could also be important.

It is easy to understand why the amplitudes inferred from travel time studies are apt to be larger when structure is included. Suppose the core/mantle boundary is elevated at some point Q. Then, a PKP ray passing through the boundary at Q has an increased travel time because fast mantle material in the vicinity of Q has been replaced by slower core material. If internal core structure is present, surfaces of constant wave velocity in the core beneath Q would likely be elevated, as well. The effect of this internal structure is that core material at any level beneath Q has been pushed upwards, and replaced by the slightly faster core material immediately below. This tends to decrease the travel time of the ray, thus partially offsetting the effects of the boundary topography. If the effects of internal structure are not included in the inversion, the inversion algorithm interprets the reduced travel time perturbations as due to smaller topography.

The effects of the induced internal structure have been found to be less important for free oscillation inversions (J. Woodhouse, personal communication; G. Masters, personal communication). The reason for this difference is probably that the free oscillation kernels (the functions that represent the dependence of the eigenfrequencies on structure) are oscillatory functions of radius inside the core. Since, as we shall see, induced structure inside the core tends to have the same sign at all radii, the effects on the eigenfrequencies would tend to cancel. On the other hand, core-phase travel time kernels have the same sign everywhere: an increase in wave speed anywhere along the path reduces the travel time. Thus, the effects of core internal structure at different radii tend to add constructively.

In Section 2, we will describe the relevant equations, and their solutions, for the problem of computing the structure inside the core. In Section 3, we will discuss the implications of our results for the problem of inferring core/mantle boundary topography from observations of the luni-solar nutations and diurnal earth tides. The results from those observations provide a constraint on the the core's moments of inertia which, in turn, can be related to the $Y_{l=2}^{m=0}$ coefficients of the core/mantle boundary topography and of the structure within the core. We will describe the sensitivity of the results to different assumptions about the internal structure. We will discuss the possible effects of a thin, low density fluid layer at the top of the core, such as might result from gravitationally-induced convection in the core. Section 4 summarizes the results, and includes a discussion of whether there is likely to be significant internal structure. We conclude that significant structure is not implausible, and, at the very least, it should not be dismissed out-of-hand when confronted with unexpected seismic anomalies.

2 THEORY

Stevenson [1987] concludes that dynamical forces originating within the fluid core are incapable of supporting any appreciable internal structure. Thus, if sizable structure exists, it must, instead, be due to external forcing from the mantle or inner core. In this section, we describe a method for computing the structure, given knowledge of the external forcing.

There are at least two possible ways of approaching this problem. One is to start with the result for a static fluid that, within the fluid core, surfaces of constant density are surfaces of constant potential. This leads directly to the construction of an integral-differential equation for the spherical harmonic coefficients of the structure which, after suitable differentiation, reduces to Clairaut's differential equation. This is the usual method of deriving Clairaut's equation [see, for example, Jeffreys, 1976].

The second method uses the Eulerian equations of motion for a static fluid to derive a differential equation directly. Boundary conditions are also obtained. The differential equations derived using

34

these two methods are identical. But, with the first method it is the integral-differential equation that determines the unknown constants in the general solution to Clairaut's equation; in the second method it is the boundary conditions. Here, we will use the second method.

2a. Forcing From the Mantle and Core/Mantle Boundary

There are two ways in which the mantle can perturb the constant density surfaces inside the fluid core. First, any non-hydrostatic core/mantle boundary topography can cause deformation inside the fluid core by constraining the outer fluid boundary to have a given shape. We will denote the increase in the radial coordinate of the boundary at the angular position (θ, λ) by

$$h^M(\theta, \lambda) = a \sum_{l,m} h^M_{l,m} Y^m_l(\theta, \lambda) \tag{1}$$

where a is the mean core/mantle boundary radius. Throughout this chapter, the complex spherical harmonics, Y^m_l, are assumed to be normalized so that

$$\int_{sphere} Y^m_l(\theta, \lambda) \bar{Y}^{m'}_{l'}(\theta, \lambda) \sin\theta \, d\theta \, d\lambda = \delta_{l,l'} \, \delta_{m,m'}. \tag{2}$$

Second, non-hydrostatic mass anomalies in the mantle can produce a gravitational force inside the core which deforms the constant density fluid surfaces. These mass anomalies would include any lateral variation in the density field inside the mantle, and any anomaly due to a change in the shape of the core/mantle boundary. For example, if the boundary is elevated in some region, then light mantle material in that region has been replaced by heavier core material, and so there is a net positive surface mass anomaly. If the elevation of the boundary is $h^M(\theta, \lambda)$, then the effective surface mass density is:

$$\sigma(\theta, \lambda) = (\rho(a_-) - \rho(a_+)) \, h^M(\theta, \lambda) \tag{3}$$

at $r = a$, where a_+ and a_- represent the values of r just outside and just inside, respectively, the core/mantle boundary, and $\rho(a_+)$ and $\rho(a_-)$ are the mantle and fluid core densities, respectively, at the boundary.

To describe the effects of the mass anomaly inside the mantle (ie. above the core/mantle boundary), we define the gravitational potential energy per unit mass caused by the non-hydrostatic density field inside the mantle as

$$V^M(\theta, \lambda) = \sum_{l,m} V^M_{l,m}(r) \, Y^m_l(\theta, \lambda) \tag{4}$$

2b. Forcing From the Inner Core and Inner Core/Outer Core Boundary

There can be similar forcing of the fluid outer core by the solid inner core. We describe this forcing in terms of the inner core/outer core boundary topography

$$h^{IC}(\theta, \lambda) = b \sum_{l,m} h^{IC}_{l,m} Y^m_l(\theta, \lambda) \tag{5}$$

where b is the mean radius of the inner core/outer core boundary, and in terms of the gravitational

35

potential energy per unit mass

$$V^{IC}(r,\theta,\lambda) = \sum_{l,m} V_{l,m}^{IC}(r)\, Y_l^m(\theta,\lambda) \qquad (6)$$

caused by the non-hydrostatic density distribution inside the inner core (ie., beneath the inner core/outer core boundary).

2c. The Response of the Fluid Core

How does an initially spherically-symmetric fluid respond to V^M, V^{IC}, h^M, and h^{IC}? Let

$$\phi(r,\theta,\lambda) = \sum_{l,m} \phi_{l,m}(r)\, Y_l^m(\theta,\lambda) \qquad (7)$$

be the total gravitational potential in the fluid. So,

$$\phi_{l,m} = V_{l,m}^M + V_{l,m}^{IC} + V_{l,m}^{OC} \qquad (8)$$

where the $V_{l,m}^{OC}$ are the spherical harmonic coefficients of the potential caused by the perturbed density inside the fluid core and by the surface mass anomalies due to the perturbed inner core/outer core and core/mantle boundaries (for example, due to $\sigma(\theta,\lambda)$ in (3) for the perturbed core/mantle boundary).

If we can find $\phi_{l,m}$ ($\phi_{l,m}$ is unknown because the fluid core contributions to $V_{l,m}^{OC}$ are unknown), we can infer the structure of constant density surfaces inside the fluid from the static-limit requirement that constant density surfaces coincide with surfaces of constant potential. This requirement implies that if

$$r = r_0\left[1 + \sum_{l,m} \varepsilon_{l,m}(r_0)\, Y_l^m(\theta,\lambda)\right] \qquad (9)$$

describes the constant density surface with mean radius $r=r_0$, then

$$\varepsilon_{l,m}(r) = -\frac{\phi_{l,m}(r)}{rg(r)} \qquad (10)$$

where $g(r)$ is the unperturbed gravitational acceleration.

Dahlen [1974; equation 6.2] finds that in the static limit, $\phi_{l,m}$ is a solution to:

$$\partial_r^2\phi_{l,m} + \frac{2}{r}\partial_r\phi_{l,m} - \left[\frac{l(l+1)}{r^2} + \frac{4\pi G}{g}\,\partial_r\rho\right]\phi_{l,m} = 0 \qquad (11)$$

where $\rho=\rho(r)$ is the unperturbed density. Equation (11) is the differential equation for internal structure. It is equivalent to Poisson's equation ($\nabla^2\phi = 4\pi G\,\delta\rho$), where the source density ($\delta\rho$) is the perturbation in the core's density distribution (use (10) in (30), below). Clairaut's differential equation for $\varepsilon_{l,m}(r)$ can be obtained by using (10) in (11).

The $\phi_{l,m}$ also satisfy internal and external boundary conditions. At internal boundaries

$$\phi_{l,m}(r_-) = \phi_{l,m}(r_+) \tag{12}$$

$$\partial_r\phi_{l,m}(r_-) - \phi_{l,m}(r_-)\frac{4\pi G\rho(r_-)}{g(r_-)} = \partial_r\phi_{l,m}(r_+) - \phi_{l,m}(r_+)\frac{4\pi G\rho(r_+)}{g(r_+)}$$

where r_- and r_+ represent the values of r just inside and outside the boundary [Dahlen, 1974; equation (63)].

To find the external boundary conditions, note that if $\phi_{l,m}(r)$ is continued across the core/mantle boundary ($r = a$) into the mantle, then both $\left[\phi_{l,m}(r)\right]$ and $\left[\partial_r\phi_{l,m}(r) + 4\pi G\rho(r) \, r \, h_{l,m}^M\right]$ are continuous across that boundary [Dahlen, 1974, equation (52)]. These continuity conditions can be replaced by a single, inhomogeneous boundary condition at $r = a$ for $\phi_{l,m}$ just below the boundary, as follows. Note that $V_{l,m}^{OC}$, $V_{l,m}^M$, $V_{l,m}^{IC}$, $\partial_r V_{l,m}^M$, and $\partial_r V_{l,m}^{IC}$ are all continuous across $r=a$. ($\partial_r V_{l,m}^M$ would not be continuous if we had defined $V_{l,m}^M$ to include the effects of the density anomaly associated with core/mantle topography.) Also, $\partial_r V_{l,m}^{OC}$ satisfies

$$\partial_r V_{l,m}^{OC}(a_-) + 4\pi G\left[\rho(a_-)-\rho(a_+)\right] a \, h_{l,m}^M = \partial_r V_{l,m}^{OC}(a_+) \tag{13}$$

$\partial_r V_{l,m}^{OC}$ is discontinuous, because we have defined $V_{l,m}^{OC}$ so that it includes the potential from the perturbed core/mantle and inner core/outer core boundaries.

By using $V_{l,m}^{OC} = \phi_{l,m} - V_{l,m}^{IC} - V_{l,m}^M$, and noting from the radial dependence of solutions to Laplace's equation that

$$\partial_r V_{l,m}^M(r) = \frac{l}{r}V_{l,m}^M(r) \qquad \text{for } r < a$$

$$\partial_r V_{l,m}^{IC}(r) = -\frac{l+1}{r}V_{l,m}^{IC}(r) \qquad \text{for } r > b \tag{14}$$

$$\partial_r V_{l,m}^{OC}(r) = -\frac{l+1}{r}V_{l,m}^{OC}(r) \qquad \text{for } r > a$$

we can transform (13) to

$$\partial_r\phi_{l,m}(a) + \frac{l+1}{a}\phi_{l,m}(a) = \frac{2l+1}{a} V_{l,m}^M(a) - 4\pi G\left[\rho(a_-)-\rho(a_+)\right] a \, h_{l,m}^M \tag{15}$$

Here, $\partial_r\phi_{l,m}(a)$ is the value of $\partial_r\phi_{l,m}(r)$ just below the core/mantle boundary ($\phi_{l,m}$ and $V_{l,m}^M$ are continuous across $r=a$, and so are the same on both sides of the boundary). A similar derivation for the inner core/outer core boundary gives:

$$\partial_r\phi_{l,m}(b) - \frac{l}{b}\phi_{l,m}(b) = -\frac{2l+1}{b} V_{l,m}^{IC}(b) - 4\pi G\left[\rho(b_+)-\rho(b_-)\right] b \, h_{l,m}^{IC} \tag{16}$$

where $\rho(b_+)$ and $\rho(b_-)$ are the outer core and inner core densities, respectively, at the inner core/outer core boundary, and $\partial_r\phi_{l,m}(b)$ is the value of $\partial_r\phi_{l,m}$ just above the inner core/outer core boundary.

Thus, $\phi_{l,m}$ in the fluid core is found by solving the ordinary differential equation (11), together with the external boundary conditions, (15) and (16), and using the continuity conditions, (12), at any internal boundary. Note that the forcing parameters, $V_{l,m}^M$, $V_{l,m}^{IC}$, $h_{l,m}^M$, and $h_{l,m}^{IC}$, are present in the external boundary conditions but not in the differential equation or the internal continuity conditions.

The boundary conditions (15) and (16) suggest that the fluid core structure has the same radial dependence for forcing from the boundary topography term, $h_{l,m}^M$, as from the applied potential coefficient $V_{l,m}^M$ (similarly for $h_{l,m}^{IC}$ and $V_{l,m}^{IC}$). The reason is that the forcing from $h_{l,m}^M$, like the forcing from $V_{l,m}^M$, is actually gravitational. By fixing the perturbed surface of the core to have the shape specified by h^M, we are introducing the effective surface mass density, (3), at $r=a$, which acts gravitationally on the material inside the fluid core and deforms it.

In some cases there may be more useful ways to parameterize the forcing than in terms of the boundary topography and applied gravitational potential coefficients. One particularly simple alternative is to use, instead, the Y_l^m coefficients of the equipotential surface at the inner and outer core boundaries as the forcing parameters. A problem with this alternative is that the shape of an equipotential surface depends on the structure inside the fluid core, which is assumed here to be unknown. Still, as we shall see, this choice of parameterization can be convenient for physical interpretation and is particularly useful when inverting for the structure.

To include this parameterization, let

$$d^M(\theta,\lambda) = a\sum_{l,m}\varepsilon_{l,m}(a)Y_l^m(\theta,\lambda) \tag{17}$$

$$d^{IC}(\theta,\lambda) = b\sum_{l,m}\varepsilon_{l,m}(b)Y_l^m(\theta,\lambda)$$

represent the increase in the radial coordinates of the equipotential (and equidensity) surfaces at the core/mantle and inner core/outer core boundaries, respectively. Then, the boundary conditions (15) and (16) are replaced by the much simpler conditions (using (10))

$$\phi_{l,m}(a) = -ag(a)\varepsilon_{l,m}(a) \tag{18}$$

$$\phi_{l,m}(b) = -bg(b)\varepsilon_{l,m}(b) \tag{19}$$

2d. Approximate Solutions

Suppose the fluid core was homogeneous, with uniform density $\rho(r) = \rho_0$. Then, the general solution to the differential equation (11) would be

$$\phi_{l,m} = D\left[\frac{r}{a}\right]^l + E\left[\frac{a}{r}\right]^{(l+1)} \tag{20}$$

so that, using (10) with $g(r) = \frac{4}{3}\pi G\rho_0 r$ (we assume the inner core also has uniform density ρ_0),

$$\varepsilon_{l,m}(r) = F\left[\frac{r}{a}\right]^{l-2} + G\left[\frac{a}{r}\right]^{(l+3)} \tag{21}$$

where the constants F and G are proportional to D and E.

The solution for an inhomogeneous fluid core is, of course, more complicated. We have solved (11) numerically using $\rho(r)$ from earth model PREM [Dziewonski and Anderson, 1981], and then using perturbations of PREM obtained by inserting a thin, low density layer at the top of the fluid core, such as might result from compositional convection in the core (see section 3, below, for the motivation for including such a boundary layer). We find, in all these cases, that $\varepsilon_{l,m}(r)$ has very close to the same radial dependence as does the homogeneous solution (21). The gravitational potential, $\phi_{l,m}$, agrees less

38

well with the homogeneous result (20). But, by using (21) in (10), we can obtain a reasonably accurate approximation for $\phi_{l,m}$:

$$\phi_{l,m} \approx -\left[F\left(\frac{r}{a}\right)^{l-2} + G\left(\frac{a}{r}\right)^{(l+3)}\right] g(r)r \tag{22}$$

where F and G are constants that must be determined from the boundary conditions. Using (22) either in (15) and (16) or in (18) and (19), depending on the type of boundary conditions being considered, and solving for F and G, we obtain results for the internal structure coefficient $\varepsilon_{l,m}(r)$ that agree well with the more accurate numerical solution to (11). For example, we find that for boundary conditions (18) and (19) with $\varepsilon_{l,m}(a) = 1$ and $\varepsilon_{l,m}(b) = 0$ (imposed structure at the core/mantle boundary and none at the inner core/outer core boundary), and for every $l \leq 10$, the result for $\varepsilon_{l,m}(r)$ at any radius, r, derived using the approximate form (21) agrees with the numerical solution using PREM to better than 2% of the value of $\varepsilon_{l,m}(a)$ ($\varepsilon_{l,m}(a)$ is the maximum value of $\varepsilon_{l,m}(r)$ for these boundary conditions). The agreement for (18) and (19) with $\varepsilon_{l,m}(a) = 0$ and $\varepsilon_{l,m}(b) = 1$ (imposed structure at the inner core/outer core boundary) is better than 11% of $\varepsilon_{l,m}(b)$ ($\varepsilon_{l,m}(b)$ is the maximum value of $\varepsilon_{l,m}(r)$ in this case).

As a special case which will be considered in more detail in the next section, suppose the inner core behaves like a fluid over long time periods. Then, we can extend our model and compute the response of the entire (outer plus inner) core to forcing from the mantle alone. In that case, $\phi_{l,m}$ must satisfy the differential equation (11) for $0 \leq r \leq a$, it must be finite when $r=0$, and it needs to satisfy boundary conditions only at $r=a$: either (15) or (18). For either boundary condition, the homogeneous solutions

$$\varepsilon_{l,m}(r) = F\left(\frac{r}{a}\right)^{l-2} \tag{23}$$

$$\phi_{l,m}(r) = -F\left(\frac{r}{a}\right)^{l-1} g(r)a$$

are found to closely approximate the solutions to the differential equation (11) for realistic $\rho(r)$. For boundary condition (15),

$$F = \frac{4\pi G \rho(a_-)\, a\; h_{l,m}^M - V_{l,m}^M(a)(2l+1)/a}{2(l-1)g(a) + 4\pi G a \rho(a_-)} \tag{24}$$

For boundary condition (18):

$$F = \varepsilon_{l,m}(a) \tag{25}$$

These homogeneous results are identical to the exact solutions for $l=1$ no matter what the functional form of $\rho(r)$. For $1 < l \leq 10$, they provide estimates for $\varepsilon_{l,m}(r)$ which are accurate to better than 2% of $\varepsilon_{l,m}(a)$ ($\varepsilon_{l,m}(a)$ is the maximum value of $\varepsilon_{l,m}(r)$ in this case).

The result (24) for F implies that the response of the core to $V_{l,m}^M(a)$ increases with decreasing $\rho(a_-)$. As an extreme case, $\varepsilon_{l=1,m}(r)$ is inversely proportional to $\rho(a_-)$. This behavior is readily understood physically, as follows. A $V_{l=1,m}^M(a)$ term represents a uniform force on the core. Because of this force, the surfaces of constant density inside the core are all displaced the same amount along the direction of the force, as shown in Figure IV.1. This displacement causes the layer at the outer surface of the core to develop the asymmetrical shape shown in Figure IV.1: extra mass on one side, a reduction in mass on the other. This mass asymmetry provides an additional gravitational force on the core interior,

39

which opposes the force from $V_{l=1,m}^M$. The displacements in the core increase until these two forces exactly cancel. Since the asymmetry in the surface mass distribution is proportional to $\rho(a_-)\epsilon_{l=1,m}(a)$, and since the gravitational force from the layer is proportional to the mass asymmetry, then $\epsilon_{l=1,m}(a)$ is inversely proportional to $\rho(a_-)$. The dependence of $\epsilon_{l,m}(a)$ on $\rho(a_-)$ for $l > 1$ can be understood similarly.

3 THE NUTATION AND EARTH TIDE CONSTRAINT

3a. Constraints on the Core's Inertia Tensor

The free core nutation (FCN) is a normal mode of the earth, with an approximately diurnal period and with an eigenfunction consisting primarily of a relative rotation between the core and mantle. The mode has been modelled semi-analytically for an earth with slightly aspherical, but otherwise arbitrary structure, and for an inner core which is assumed to be fluid [see, eg. Wahr and de Vries, 1989]. The FCN eigenfrequency in that case is found to depend on the dynamical ellipticity of the core:

$$e = (C-A)/A \tag{26}$$

where C and A are principal moments of inertia of the core. The effects on the eigenfrequency of a solid inner core are small [de Vries and Wahr, 1989], and need not concern us, here.

If

$$\delta\rho(r,\theta,\lambda) = \sum_{l,m}\delta\rho_l^m(r)Y_l^m(\theta,\lambda) \tag{27}$$

is the aspherical density distribution inside the core, then the contribution to e from the non-hydrostatic structure and topography is

$$\delta e = -\frac{2\sqrt{\pi/5}}{A}\left[a^5 h_{2,0}^M\rho(a_-) + \int_0^a \delta\rho_2^0(r)r^4 dr\right] \tag{28}$$

so that δe depends only on the Y_2^0 components of boundary topography and internal structure.

The luni-solar forced nutations and diurnal earth tides occur at frequencies close enough to the FCN eigenfrequency to be significantly affected by the mode. Their amplitudes have been used to constrain the eigenfrequency [see, eg., Gwinn, et al., 1986, for nutation results; Levine, et al, 1986, and Neuberg, et al., 1987, for tidal results]. The nutation and earth tide results for the eigenfrequency are consistent with each other, and imply a value for e about 5% in excess of the hydrostatic value. The VLBI nutation estimates, which currently provide the most accurate results for the eigenfrequency, imply that the contribution to e from non-hydrostatic internal core structure and core/mantle boundary topography is

$$\delta e = 1.22 \times 10^{-4} \tag{29}$$

with an uncertainty of about ± 10% [Gwinn, et al., 1986]. Since

$$\delta\rho_l^m(r) = -r\epsilon_{l,m}(r)\partial_r\rho(r) \tag{30}$$

then (28) and (29) imply the following constraint on $h_{2,0}^M$ and $\epsilon_{2,0}(r)$:

40

$$\frac{2\sqrt{\pi/5}}{A}\left[a^5 h_{2,0}^M \rho(a_-) - \int_0^a r^5 \epsilon_{2,0}(r)\partial_r\rho(r)dr\right] = -1.22\times10^{-4} \qquad (31)$$

3b. Implications for Core/Mantle Boundary Topography

Consider the situation described at the end of Section 2, where the entire core responds as a fluid to forcing from the mantle and core/mantle boundary. Parameterizing the internal structure in terms of the equipotential surface components, $\epsilon_{l,m}(a)$, we find that

$$\epsilon_{2,m}(r) = \epsilon_{2,m}(a) = \text{constant} \qquad (32)$$

is a good approximation to the $l=2$ numerical solution for realistic density $\rho(r)$, particularly for large r. The large r results are especially important here because the integrand in (31) includes a factor of r^5, which results in heavy weighting of large r values. The r^5 factor also permits us to ignore the possible effects of independent structure in the inner core.

Using (32) in the constraint (31), and integrating by parts gives:

$$\frac{3}{4}\sqrt{5/\pi}\ \epsilon_{2,0}(a) + \frac{2\sqrt{\pi/5}\ \rho(a_-)a^5}{A}\left[h_{2,0}^M - \epsilon_{2,0}(a)\right] = -1.22\times10^{-4} \qquad (33)$$

When evaluated numerically, this result, (33), gives a combined constraint on $\epsilon_{2,0}(a)$ and $h_{2,0}^M$ which agrees to better than 1% with the constraint obtained using more accurate numerical solutions for $\epsilon_{2,0}(r)$ in (31). The advantage of (33) is that its dependence on $\rho(a_-)$ is clear.

Results for PREM

Using values of $\rho(a_-)$ and A that are consistent with the PREM density distribution, (33) reduces to the constraint:

$$h_{2,0}^M + .077\ \epsilon_{2,0}(a) = -1.39\times10^{-4} \qquad (34)$$

Note that (34) is a constraint primarily on the boundary topography coefficient, $h_{2,0}^M$. There is little sensitivity to the structure of the equipotential surface, $\epsilon_{l,m}(a)$ (ie. .077 is much less than 1), because: (1) the components of the core's inertia tensor (in this case, C and A) are much more sensitive to the density distribution in the outer regions of the core than to the density distribution in the interior (the r^5 dependence in (31)); and (2) PREM has little radial density contrast through the outer region of the core, and so it doesn't much matter what the shapes of the constant density surfaces are. The constraint is strongly sensitive to the topography coefficient, $h_{2,0}^M$, because there is a large contrast in the core density across the core boundary: from about 9.9 gm/cm^3 just below the boundary to 0 gm/cm^3 above (0 gm/ cm^3 because there is no core material above the core/mantle boundary).

Unless the equipotential surface at $r=a$ has Y_2^0 structure which is many times the size of the Y_2^0 boundary topography, the result (34) gives approximately

$$a\ h_{2,0}^M \approx \frac{1}{2}\ \text{km} \qquad (35)$$

41

Effects of a thin, core boundary layer

The constraint on the boundary topography is different if there is a thin, low density fluid layer at the top of the core, such as might be caused by compositional convection. In that case, the sensitivity of the core's inertia tensor to the equipotential coefficient, $\varepsilon_{2,0}(a)$, is increased because of the larger radial stratification in the outer region of the core. At the same time, the sensitivity to boundary topography is decreased because of the smaller density contrast across the core/mantle boundary. In effect, some of the 9.9 gm/cm^3 core density contrast that occurs across the core boundary in PREM is transferred to one or more surfaces (or across a finite region) within the boundary layer. The larger the radius of one of those internal surfaces, the larger the effect on the inertia tensor of the density contrast across that surface. Thus, the importance of the $\varepsilon_{2,0}(a)$ term in the constraint must depend partly on the boundary layer thickness, as well.

In anticipation of these results, we define the dimensionless parameter:

$$\Delta = \frac{8\pi}{15} \frac{\rho(a_-)a^5}{A} \tag{36}$$

The core's principal moment, A, depends on the density and thickness of the boundary layer. But, that dependence is minimal. For example, suppose the boundary layer has thickness D, and suppose the density throughout the layer is smaller than the PREM density distribution by an amount $\delta\rho$ = constant. Then, for $D \ll a$:

$$A \approx A_0 - Da^4\delta\rho 8\pi/3 \tag{37}$$

where A_0 is the PREM value of A and is approximately 9.12×10^{43} gm cm^2. To estimate the possible effects of D, note that the density in the boundary layer is unlikely to be less than about 5.6 gm/cm^3, which is the PREM density at the bottom of the mantle, and so $\delta\rho \leq 9.9 - 5.6 = 4.3$ gm/cm^3. We find numerically:

$$A \approx A_0\left[1 - \frac{Da^4\delta\rho 8\pi/3}{A_0}\right] \leq A_0\left[1 - 2.0\frac{D}{a}\right] \tag{38}$$

This result shows that as long as the boundary layer is much thinner than the core radius ($D \ll a$), $A \approx A_0$, and so A is relatively insensitive both to the boundary layer density and to the thickness. Thus, the only important dependence of Δ on the boundary layer is through $\rho(a_-)$ in the numerator of (36). If we assume that $\rho(a_-)$ is no larger than the PREM density at the top of the core, and no smaller than the PREM density at the bottom of the mantle, then

$$0.522 \leq \Delta \leq 0.928 \tag{39}$$

With the parameter Δ, (33) reduces to

$$h_{2,0}^M \Delta + \varepsilon_{2,0}(a)(1-\Delta) = -1.29 \times 10^{-4} \tag{40}$$

(Using the PREM result, $\Delta = 0.928$, in (40), we obtain (34).)

Consider the following two examples. First, consider the extreme case that the core/mantle boundary is an equipotential surface. Then $\varepsilon_{l,m}(a) = h_{l,m}^M$, and (40) reduces to

42

$$h^M_{2,0} = -1.29 \times 10^{-4} \tag{41}$$

There is no dependence on Δ in (41). The reason is that in this example the internal boundary layer structure has the same (θ, λ) dependence as the core/mantle topography. So, it doesn't matter whether the 9.9 gm/cm^3 density contrast is spread out across the top layers of the core or is all concentrated right at the boundary; the effects on the inertia tensor are the same.

Second, suppose there is no $l=2$, $m=0$ structure inside the core, so that $\varepsilon_{2,0}(a) = 0$. Then, (40) reduces to:

$$h^M_{2,0}\Delta = -1.29 \times 10^{-4} \tag{42}$$

It is clear from (42) that the nutation and earth tide constraint is able to accommodate larger $h^M_{2,0}$ values if Δ is smaller than the PREM value. Smaller Δ (ie. smaller $\rho(a_-)$) implies that there is a smaller density contrast across the core/mantle boundary, and so the boundary topography must be larger to cause a given perturbation in the inertia tensor. If Δ is equal to the minimum value of 0.522 (see equation (39)), then (42) implies that $h^M_{2,0} = 2.5 \times 10^{-4}$. This numerical result is probably the largest possible value of $h^M_{2,0}$ that is consistent with the assumption of no structure inside the core. It corresponds to Y^0_2 boundary topography of .87 km.

But, this last example $(\varepsilon_{2,0}(a)=0)$ is not the most extreme possibility. The nutation constraint for a core with a boundary layer can accommodate still larger boundary topography, if the internal structural parameter, $\varepsilon_{2,0}(a)$, is the same order as $h^M_{2,0}$ but with the opposite sign. For example, if we use the lower bound $\Delta = 0.522$ in (40), we obtain

$$h^M_{2,0} + .916\ \varepsilon_{2,0}(a) = -2.47 \times 10^{-4} \tag{43}$$

For $\Delta = 0.522$, roughly half the 9.9 gm/cm^3 density contrast occurs inside the core, where the contributions to the inertia tensor depend on $\varepsilon_{2,0}(a)$ instead of on $h^M_{2,0}$. This is why the constraint equation, (43), is as sensitive to the internal structure as to the boundary topography.

Suppose $h^M_{2,0}$ and $\varepsilon_{2,0}(a)$ have opposite signs. Then, the effects of the boundary topography on the inertia tensor are partially offset by the effects of the structure in the boundary layer, and both $h^M_{2,0}$ and $\varepsilon_{2,0}(a)$ can have large amplitudes and still satisfy the nutation/earth tide constraint. There can be large $l=2$ topography for Δ greater than 0.522, as well. However, note from (40) that the closer Δ is to 1, the larger $\varepsilon_{2,0}(a)$ must be to offset the effects of the boundary topography.

Although this combination of a low density boundary layer and roughly equal but opposite internal structure and topography could reconcile the nutation constraint with large topography, we are not presently advocating such a situation. For one thing, there is currently no compelling reason to believe that the $l=2$, $m=0$ boundary topography is much in excess of 1/2 km. For another, there are dynamical considerations that tend to argue against such a configuration. These arguments are presented at the end of the following section.

4 DISCUSSION

There are two parts to this chapter. In the first part, we show that there can be non-hydrostatic, laterally varying structure inside the outer core. Such structure could be caused by gravitational forcing from non-hydrostatic mass anomalies inside the mantle or inner core or from the density anomalies associated with non-hydrostatic core/mantle or inner core/outer core boundaries.

The differential equation for the core structural parameters, $\varepsilon_{l,m}(r)$, is given by (10) and (11). We consider two types of possible boundary conditions for this problem. The boundary conditions (15) and (16) are appropriate if the core boundary topography and the density distribution inside the mantle and inner core are known. The boundary conditions (18) and (19) are appropriate if the equipotential surfaces at the mean inner core and outer core radii are known.

43

It is unlikely that the equipotential surfaces at the boundaries would be known. After all, the potential depends partly on the density distribution inside the core and that is not known prior to solving the equations. If the inner and outer core boundaries could be assumed to be equipotential surfaces, then the $\varepsilon_{l,m}(a)$ and $\varepsilon_{l,m}(b)$ in (18) and (19) could be determined from knowledge of the boundary topography. However, this assumption is unlikely to be valid, because it would probably require unacceptably small values for the viscosity of the lower-most mantle (Brad Hager, personal communication).

Instead, the primary use of the boundary conditions (18) and (19), is in providing a convenient parameterization for the internal structure. One of the possible applications of the theory described here is to facilitate data inversions for the structure. Seismic travel time studies, for example, might be particularly useful. The results of this chapter show that inversions for core structure, unlike inversions for mantle structure, do not require solutions for the structure at different radii. Instead, the radial dependence of the structure inside the fluid core is determined by the differential equation, (11), and so the entire solution can be parameterized in terms of a set of boundary coefficients: the right hand sides of either (15) and (16) or of (18) and (19). The data can be inverted to find those coefficients. The boundary conditions (18) and (19) are particularly useful because of their simplicity.

The numerical solutions to the differential equation (11) are found to have an easily characterized, approximate radial dependence, given by (21). For short horizontal wavelengths (large l), the structure falls off rapidly with distance from the boundaries. For example, the structural amplitudes beneath the core/mantle boundary decrease with decreasing radius approximately as $(r/a)^{(l-1)}$ (the amplitude of the structure is $r\varepsilon_{l,m}(r)$, and $\varepsilon_{l,m}(r)$ is proportional to $r^{(l-2)}$: see equation (23)). This implies that there is not apt to be much short wavelength core structure away from boundaries. It helps explain the results of Wahr, et al. [1987], who found that their seismic travel time inversions for core/mantle boundary topography were relatively insensitive to assumptions about the internal structure at angular orders $l >$ 3. Note, also, that $(r/a)^{(l-1)}$ is a monotonic function of radius. As described in the Introduction, this helps explain why fluid core structure has a more important effect on travel times than on free oscillations.

In the second part of this chapter, we discuss the possible effects of fluid core structure on the interpretation of nutation and diurnal earth tide observations. Those observations constrain the core's dynamical ellipticity, which is related to the core's principal moments of inertia.

The moments of inertia can be affected by boundary topography and by internal structure. The sensitivity to the topography and structure depends on the radial density distribution at the top of the core. If the density is consistent with PREM, there is little sensitivity to internal structure. The PREM density varies slowly with radius in the outer region of the core, and so the shapes of the constant density surfaces are pretty much irrelevant. In this case, the results for the dynamical ellipticity mostly constrain the core/mantle boundary topography.

If there is a low density boundary layer at the top of the core, the inertia tensor is more sensitive to internal structure and less sensitive to the boundary topography. To understand this result, note that the outer surface of the boundary layer would coincide with the core/mantle boundary, while the shape of the boundary layer inner surface would depend on the internal structure. The smaller the density of the boundary layer, the larger the density contrast across the inner surface, and so the greater the sensitivity to internal structure. At the same time, a smaller boundary layer density means decreased sensitivity to the shape of the outer surface of the boundary layer: ie. to the core/mantle boundary topography.

The general result for the nutation/earth tide constraint is given by (40). The dimensionless parameter Δ in that equation depends on the density at the core/mantle boundary (see equation (36)), and is unlikely to have a numerical value outside the interval given in (39). Small values of the boundary layer density imply small values of Δ. The PREM density distribution ($\Delta = 0.928$), leads to an inferred Y_2^0 coefficient of the core/mantle boundary topography of about 1/2 km.

A larger numerical result for the topography is obtained if there is a low density boundary layer ($\Delta <$ 0.928) at the top of the core. Still, using the lower bound for Δ of 0.528, we find that the only way the Y_2^0 topography coefficient could be larger than .87 km, is if there is internal structure with the opposite sign of the boundary topography. In that case, contributions to the moments of inertia from the topography are partially offset by contributions from the structure at the bottom of the boundary layer.

As an example of how these constraints can be used, suppose we invert a seismic data set to learn about core/mantle boundary topography, and obtain an $l=2$, $m=0$ coefficient with an amplitude significantly larger than 1/2 km. Our result, then, is at odds with the nutation and earth tide constraint estimated using the PREM value of Δ. To reconcile our seismic coefficient with that constraint, we might be tempted to hypothesize the existence of a low density boundary layer at the top of the core, and of internal structure with a large amplitude but with the opposite sign of the boundary coefficients.

One problem we might encounter, though, is that the internal structure we are proposing could be inconsistent with the assumptions we made before we started our seismic inversion. And, the effects on our inversion of ignoring this structure could be important. For example, the $l=2$ topography coefficients inferred by Wahr, et al. [1987] from PKP travel times, differed by up to a factor of two depending on whether they assumed the core/mantle boundary was an equipotential surface or ignored internal structure entirely.

In fact, even the hypothesis of a boundary layer itself, without specifying any internal structure, could have consequences for our inversion. For example, the sensitivity of PKP travel times to core/mantle boundary topography depends on the velocity contrast across the boundary. And a core-side boundary layer could affect that contrast.

Is There Likely to be Significant Internal Structure?

An even more fundamental issue, is whether the combination of large opposing structure and topography and a low density fluid boundary layer is plausible, based on our understanding of mantle dynamics. In fact, the question of whether there could be any appreciable structure inside the core is clearly important for all applications of the results described in this chapter, whether the core has a low density boundary layer, or not.

What insight we can offer into this problem is based on preliminary results from Dehant and Wahr (in preparation), who compute the deformation of internal boundaries and the perturbation in the gravitational potential caused by internal loading, using methods similar to those employed by Richards and Hager [1984], Forte and Peltier [1987], and Zhang and Yuen, [1987]. The results are strongly dependent on the assumed characteristics of the D'' layer at the base of the mantle, and on whether there is a low density, fluid boundary layer at the top of the core. For example, if convection in the lower mantle penetrates all the way to the base of the mantle (ie. to the core/mantle boundary), if the viscosity of the D'' layer is not very much smaller than the viscosity of the rest of the lower mantle, and if there is no core-side boundary layer, then the $l=2$ structural coefficients ($\varepsilon_{2,m}(a)$) are roughly 20% of the $l=2$ topographic coefficients ($h_{2,m}^{M}$), for loads in the mid-mantle.

On the other hand, if there is a barrier to convection somewhere in the D'' layer above the core/mantle boundary, if the D'' layer has a significantly lower viscosity than the rest of the lower mantle, and if there is no low density fluid boundary layer at the top of the core, then a mid-mantle load could cause perturbations in $\varepsilon_{2,m}(a)$ and $h_{2,m}^{M}$ of roughly equal amplitudes but opposite signs. (The opposing signs of the boundary and equipotential surface in this case are analogous to a similar effect at the outer surface, discussed by Richards and Hager [1984], that occurs when there is a barrier to flow between the upper and lower mantles.) We note that the case of roughly equal amplitudes occurs because, for an internal load of given strength, the topography becomes small, and not because the internal structure becomes large.

Thus, it is possible that the induced structure could be as large or larger than the induced topography. This would occur, for mid-mantle loads, for a restricted but not implausible range of D'' parameter values. This suggests that the possibility of significant internal structure should not be dismissed out-of-hand when interpreting unexpected seismic anomalies.

If a low density boundary layer is included at the top of the core, the induced boundary topography is increased. The boundary tends to deform in response to an internal load, so that the total surface mass anomaly associated with the deformation equals some value that is determined by the amplitude and wavelength of the load. The surface mass anomaly, (3), is the product of the deformation (h^{M}) and the

45

density contrast across the boundary $(\rho(a_-) - \rho(a_+))$. If there is a low density boundary layer at the top of the core, then the density contrast is decreased, and so the topography must be correspondingly increased.

This argues against the combination of a low density boundary layer and roughly equal but opposite core structure and topography, introduced at the end of Section 3 as a way of reconciling large boundary topography with the nutation constraint. If the boundary layer density is low enough that there is only a small density contrast across the core/mantle boundary, then the load-induced topography on the boundary would almost certainly be much larger than the load-induced internal structure. We thus conclude that the nutation constraint is probably not compatible with $l=2$, $m=0$ boundary topography much in excess of .87 km (the result for $\Delta = .528$ and no internal structure). Furthermore, we emphasize that there is currently no compelling reason to believe that the $l=2$, $m=0$ topography is anything different than the 1/2 km result implied by the nutation/body tide observations using the PREM value of $\Delta = .928$.

CHAPTER IV REFERENCES

Creager, K.C. and T.H. Jordan, 1986; Aspherical structure of the core-mantle boundary from PKP travel times, *Geophys. Res. Lett.,* 13, 1497.

Dahlen, F.A., 1974; On the static deformation of an earth model with a fluid core, *Geophys. J. R. Astr. Soc., 36,* 461-485.

de Vries, D. and J. Wahr, 1989. (in preparation)

Dziewonski, A, and D.L. Anderson, 1981. Preliminary reference earth model, *Phys. Earth Planet. Inter., 25,* 297-356.

Forte, A.M. and Peltier, W.R., 1987. Plate tectonics and aspherical earth structure: the importance of poloidal-toroidal coupling, J. Geophys. Res., 92, 3645-3679.

Giardini, D., X.-D. Li, and J.H. Woodhouse, 1987; Three-dimensional structure of the earth from splitting in free-oscillation spectra, *Nature, 325,* 405-411.

Gudmundsson, O., R.W. Clayton, and D.L. Anderson, 1986. CMB topography inferred from ISC PcP travel times. *Trans. Am. geophys. Un., 67,* 1100.

Gwinn, C.R., Herring, T.A., Shapiro, I.I. 1986. Geodesy by radio interferometry: Studies of the forced nutations of the earth, 2. Interpretation. *J. Geophys. Res.* 91:4755-4766

Hager, B.H., R.W. Clayton, M.A. Richards, R.P. Comer, and A.M. Dziewonski, 1985. Lower mantle heterogeneity, dynamic topography and the geoid, *Nature, 313,* 541-545.

Hide, R., Clayton, R.W., B.H. Hager, M.A. Speith, and C.V. Voorhies, 1989. The determination of topographic core-mantle coupling from geophysical data. (in preparation)

Jeffreys, H., 1976. *The Earth,* Cambridge University Press, Cambridge, 574pp.

Levine, J., J.C. Harrison, and W. Dewhurst, 1986; Gravity tide measurements with a feedback gravity meter. *J. Geophys. Res., 91,* 12,835-12,841.

Morelli, A. and A.M. Dziewonski, 1987; Topography of the core-mantle boundary and lateral homogeneity of the liquid core, *Nature, 325,* 678.

Neuberg, J., J. Hinderer, and W. Zurn, 1987. Stacking gravity tide observations in central Europe for the retrieval of the complex eigenfrequency of the nearly diurnal free-wobble. *Geophys. J. R. astr. Soc., 91,* 853-868.

Richards, M.A., and B.H. Hager, 1984. Geoid anomalies in a dynamic earth. *J. Geophys. Res., 89,* 5987-6002.

Ritzwoller, M., G. Masters, and F. Gilbert, 1986; Observations of anomalous splitting and their interpretation in terms of aspherical structure, *J. Geophys. Res., 91,* 10203-10228.

Stevenson, D.J., 1987; Limits on lateral density and velocity variations in the earth's core, *Geophys. J. R. Astr. Soc., 88,* 311-319.

Wahr, J.M., and D. DeVries, 1989; in *Variations in Earth Rotation,* AGU Monograph Series, D. McCarthy, ed. (in press).

Wahr, J.M., Rodgers, A., and Billington, S., 1987. Core-mantle boundary structure from travel times, including the effects of fluid core structure, Trans. Amer. Geophys. U. (EOS), 68, 1487.

Zhang, S. and D.A. Yuen, 1987; Deformation of the core-mantle boundary induced by spherical-shell, compressible convection, *Geophys. Res. Lett., 14,* 899-902.

CHAPTER IV FIGURE CAPTIONS

Figure IV.1. An illustration of the response of the core to an applied $l = 1$ potential. The potential induces a uniform translation of the constant density surfaces inside the core. This causes the layer at the top of the core to have an aspherical shape, with extra mass on one side and a reduction of mass on the other. This density anomaly causes a gravitational force on the core interior which opposes the applied force.
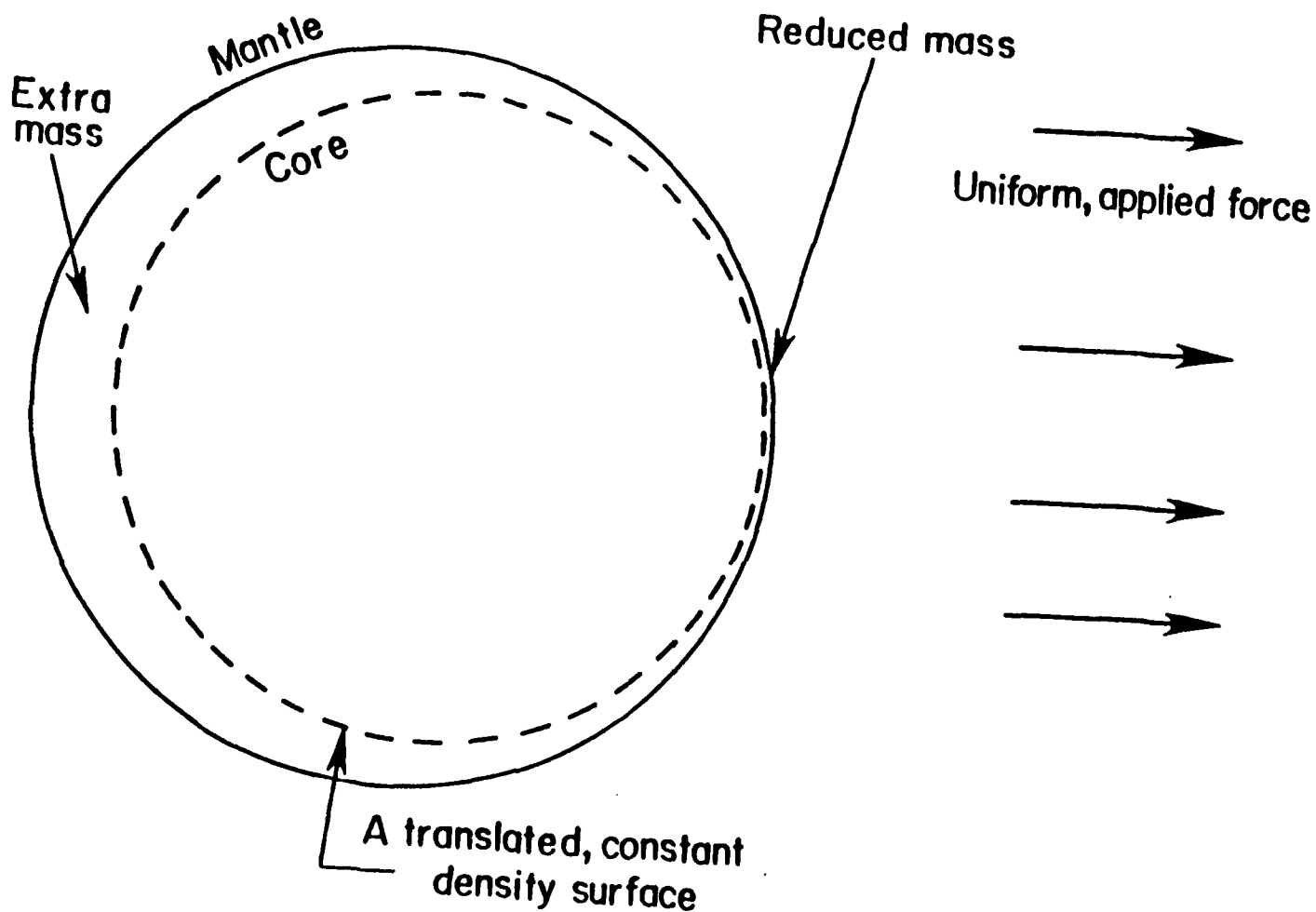
Figure IV.1

49

CHAPTER V

A COMPARISON OF NMC AND FNOC SEA LEVEL PRESSURE VALUES

SUMMARY

A comparison between values of sea level atmospheric pressure provided by the National Meteoro-logical Center and the Fleet Numerical Oceanographic Center was performed for time periods coin-cident with the SEASAT and GEOSAT Altimeter Missions. Global sea level pressure grids, each corresponding to one of three 3-day repeat orbits of the satellite, were generated for a spatial and tem-poral comparison. The results indicate that differences greater that 10 mbar are quite common in the southern ocean with offsets as large as 40 mbar in the Southern Pacific.

1. INTRODUCTION

To interpret satellite altimeter data in terms of wind generated currents, it is first desirable to remove pressure-driven variations in sea level from the data. This is usually achieved by assuming an inverted barometer response, which postulates an inverse relationship between sea level atmospheric pressure and sea surface height (-1.01cm/mbar). To apply this correction, it is necessary to adopt some model for sea level pressure over the global ocean as a function of time. For the SEASAT and GEOSAT altime-ter data, along track estimates of the pressure are obtained by interpolating between global sea level pressure grids provided by the Fleet Numerical Oceanographic Center (FNOC).

The accuracy of these pressure corrections depends critically on the accuracy of the FNOC pressure data. In this chapter we compare those data with pressure fields provided by the National Meteorologi-cal Center (NMC) for a time periods corresponding to the SEASAT and GEOSAT Altimeter Missions. Spatial and temporal differences between the data sets are calculated and plotted.

2. METHOD

The FNOC data used in this comparison were obtained directly from the SEASAT and GEOSAT Geophysical Data Records (GDR). The original FNOC pressure fields are 63 x 63 gridded polar projec-tions of each hemisphere and are generated at three hour intervals for the northern hemisphere and at six hour intervals for the southern (Parke, 1980). Values of sea level pressure were interpolated in space and time from the grids to correspond to the altimeter's ground track. The NMC data used for comparison were obtained from the National Center for Atmospheric Research in Boulder, Colorado. These consist of sea level atmospheric pressure, given twice daily from September through October of 1978 and November through December of 1986, for a 2.5° x 2.5° grid over the earth's surface.

To calculate the differences between these two data sets, we partitioned the earth into a 2.5° x 2.5° grid system like that of the NMC data set. For each three day repeat orbit, every pressure value from the GDR was assigned to a grid cell as determined by its location on the satellite's ground track. All pressure values in each cell were then averaged. NMC values, representative of the time the satellite passed over a grid cell, were also averaged over the three day time period. Six 74 x 145 grids for each of the two data sets were generated to represent the September $15^{th} - 17^{th}$ orbit, the September $18^{th} - 20^{th}$ orbit, and the October $5^{th} - 7^{th}$ orbit of SEASAT and the November $16^{th} - 18^{th}$ orbit, the

November 19th – 21th orbit, and the December 1th – 3rd orbit of GEOSAT.

RESULTS

The FNOC and NMC global pressure grids for the September 15th – 17th orbit (Orbit A^{SEA}) of SEASAT were differenced and all areas with absolute offsets greater than 10, 20, and 30 mbar are shown in Figure V.1. Figure V.2 displays the offsets between these two data sets for the November 16th –18th orbit (Orbit A^{GEO}) of GEOSAT (Note that for the GEOSAT data the increments are in units of 5 mbar instead of the 10 mbar increments used for the SEASAT data). Large discrepancies exist over much of the southern ocean with differences of up to 34 and 16 mbar concentrated in the Southern Pacific for the SEASAT and GEOSAT missions respectively.

We wondered whether the discrepancies were time independent or not. To study this question, we used the NMC and FNOC pressure grids for the second orbit, (September 18th–20th, Orbit B^{SEA}, for SEASAT and November 19th–21th, Orbit B^{GEO}, for GEOSAT) and differenced them with the corresponding grids from Orbit A^{SEA} and Orbit A^{GEO} respectively. Again, the resulting NMC and FNOC grids were compared. The results, shown in Figure V.3 and Figure V.4, thus represent differences between the FNOC and NMC representations of the variability in pressure over only 3 days. There are many instances where the differences are greater than 10 mbar. The largest offset in the SEASAT data, 33 mbar, and the GEOSAT data, 21 mbar, are again located in the Southern Pacific.

An even larger discrepancy was found by subtracting the Orbit A^{SEA} pressure from the pressure fields for the October 5th–8th orbit (Orbit C^{SEA}). The resulting differences between the NMC and FNOC in that case reached 41 mbar in the Southern Pacific (Figure V.5). This result reflects differences in the predicted variability over roughly three weeks.

A differencing of the pressure fields for the December 1th–3rd orbit of GEOSAT (Orbit C^{GEO}) and Orbit A^{GEO} is shown in Figure V.6. The differences in this case reached almost 20 mbar in the Southern Pacific.

CONCLUSIONS

These results demonstrate large differences between the FNOC and NMC pressure fields over the southern ocean during the Fall of 1978 and the Winter of 1986, with the biggest discrepancies in the Southern Pacific. The differences, which are undoubtably related to the poor spatial coverage of radiosonde stations in the southern hemisphere (David Salstein, personal communication), are strongly time dependent. For example, the FNOC and NMC data sets were found to disagree by more than 30 mbar in their representation of pressure variability over only three days during the SEASAT experiment. Errors of this magnitude in the sea level pressure fields can cause errors of more than 30 cm when removing pressure-driven changes in sea level from satellite altimeter data. This can severely degrade altimeter estimates of wind-driven circulation in the southern ocean. Analysis of the more recent GEOSAT data indicate better agreement between the two data sets but the offsets are still large enough to warrant concern. These results suggest the need for a careful assessment of the sea level pressure fields provided by the various meteorological centers around the world, with emphasis on how those fields can be improved over the southern ocean.

CHAPTER V REFERENCES

Parke, M., G.H. Born, J.F. Scott, 1980; SEASAT: Altimeter Geophysical Algorithm Specifications, *JPL Tech. Pub. #622-226*.

CHAPTER V FIGURE CAPTIONS

Figure V.1: Differences in NMC and FNOC sea level pressure values for a time period corresponding to the first three day repeat orbit of SEASAT (September 15-17, 1978). The largest differences are concentrated in the Southern Pacific ocean and reach -34 mbar.

Figure V.2: Differences in NMC and FNOC sea level pressure values for a time period corresponding to the first three day repeat orbit of GEOSAT (November 16-18, 1986). The largest differences are concentrated in the Southern Pacific ocean and reach 16 mbar.

Figure V.3: Time dependent differences in the NMC and FNOC sea level pressure values. Data points were obtained by removing the pressure values of the first three day repeat orbit of SEASAT (September 15-17, 1978) from the second three day orbit (September 18-20). The largest value of the data plotted here is 33 mbar.

Figure V.4: Time dependent differences in the NMC and FNOC sea level pressure values. Data points were obtained by removing the pressure values of the first three day repeat orbit of GEOSAT (November 16-18, 1978) from the second three day orbit (November 19-21). The largest value of the data plotted here is 24 mbar.

Figure V.5: Same as Figure V.3 but with the first orbit having been removed from a later three day orbit (October 5-7, 1978) in the mission. The largest difference is -41 mbar.

Figure V.6: Same as Figure V.4 but with the first orbit having been removed from a later three day orbit (December 1-3, 1978) in the GEOSAT mission. The largest difference is -41 mbar. * Note that for Figure V.2, Figure V.4 and Figure V.6 the divisions are in increments of 5 instead of 10
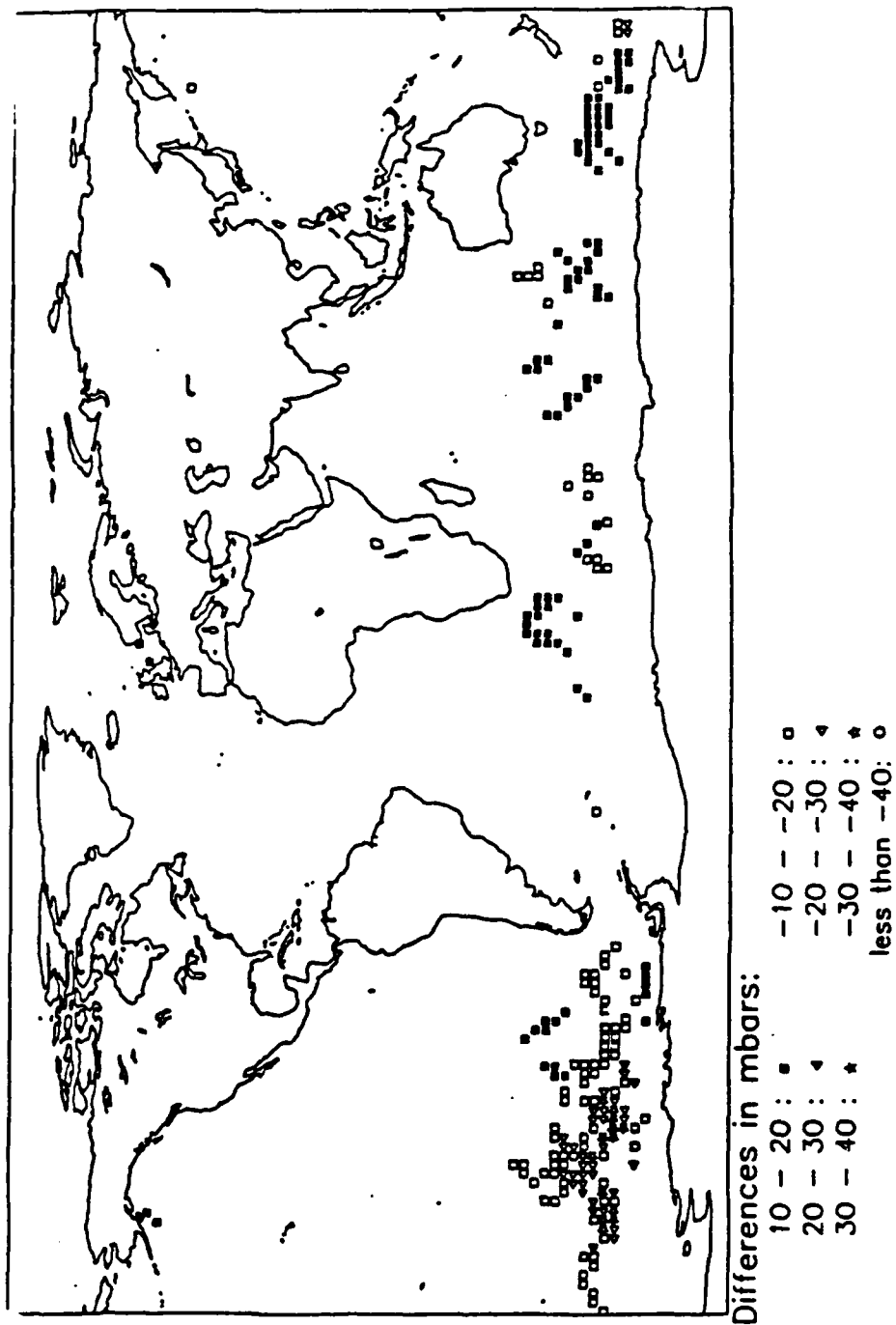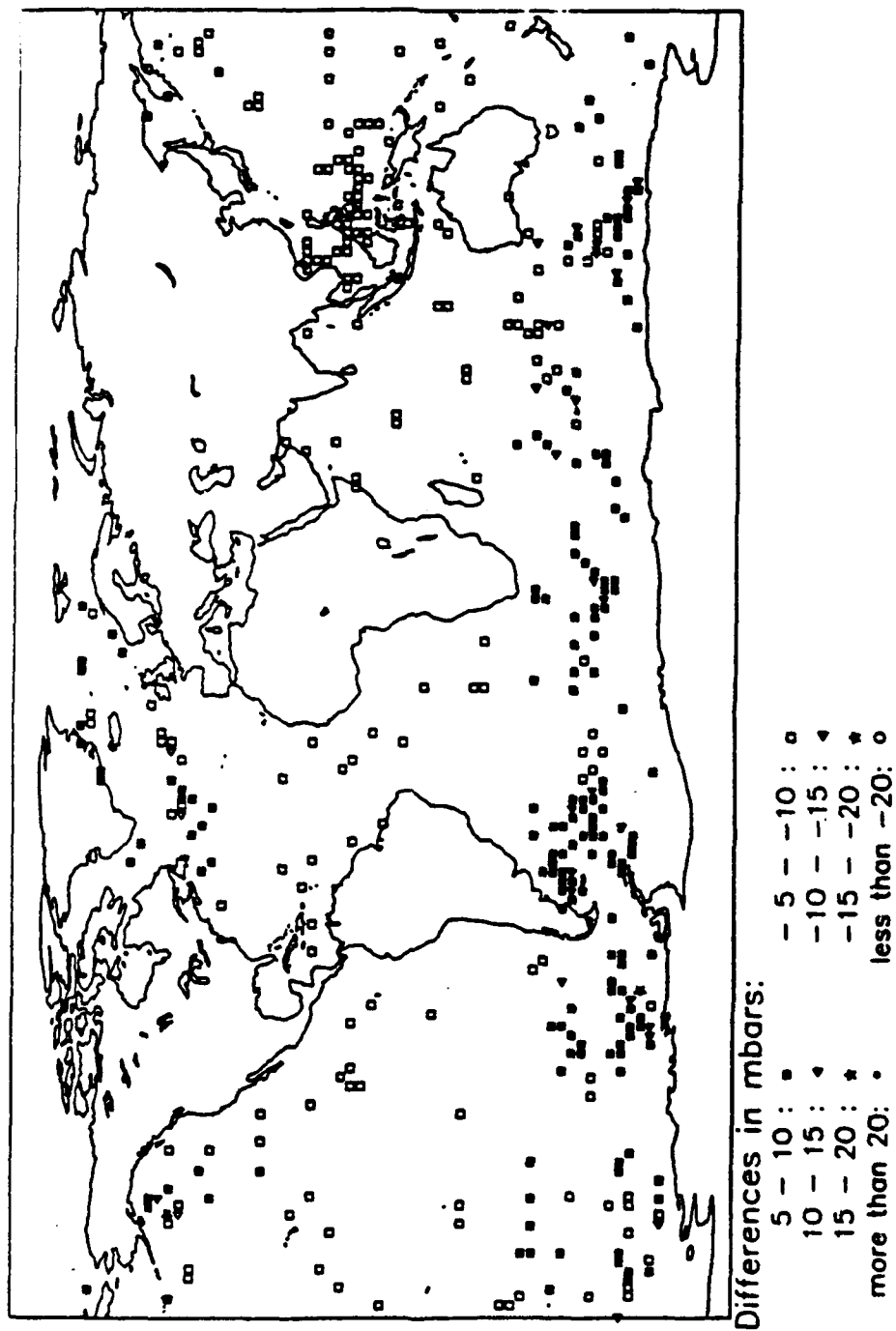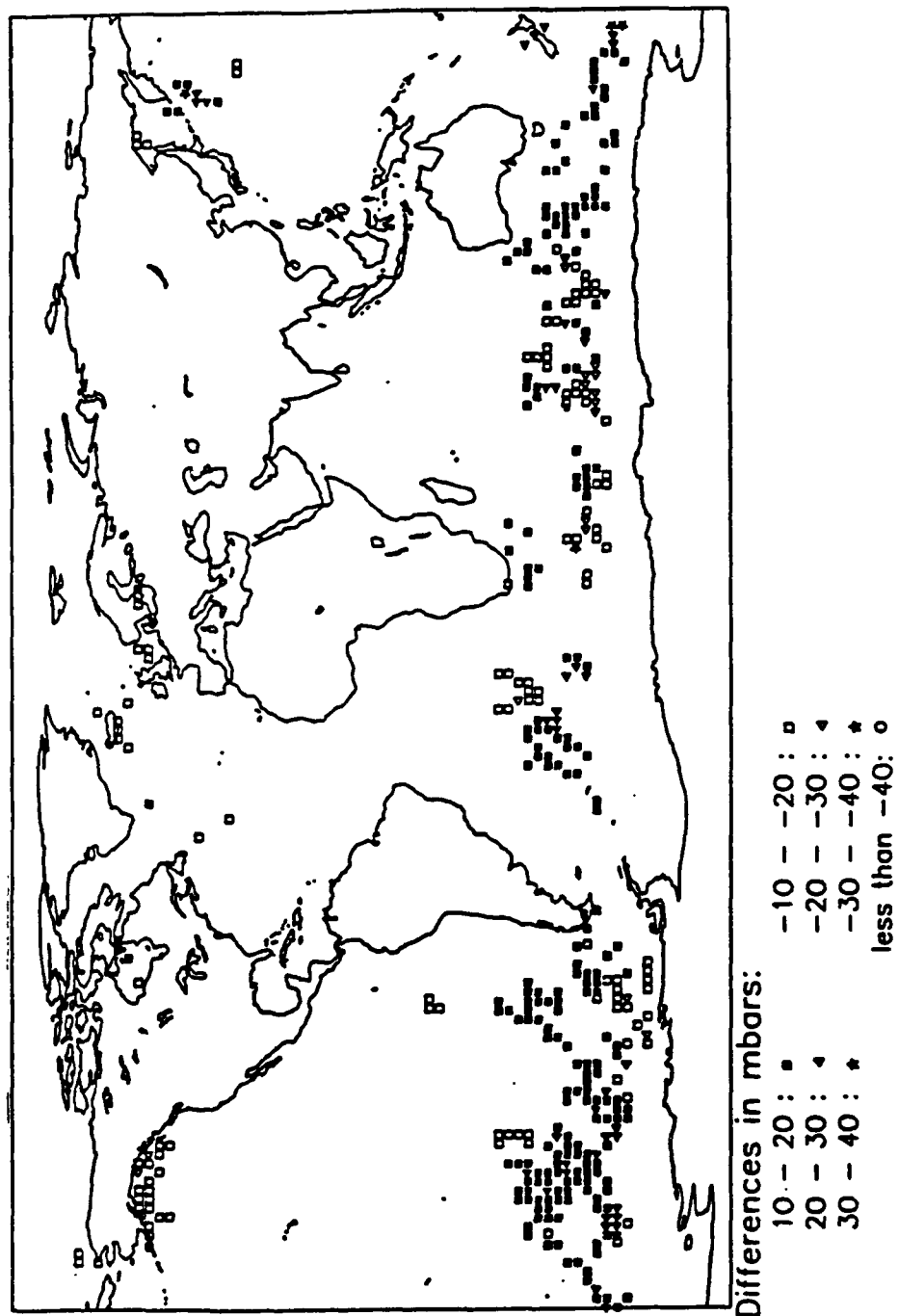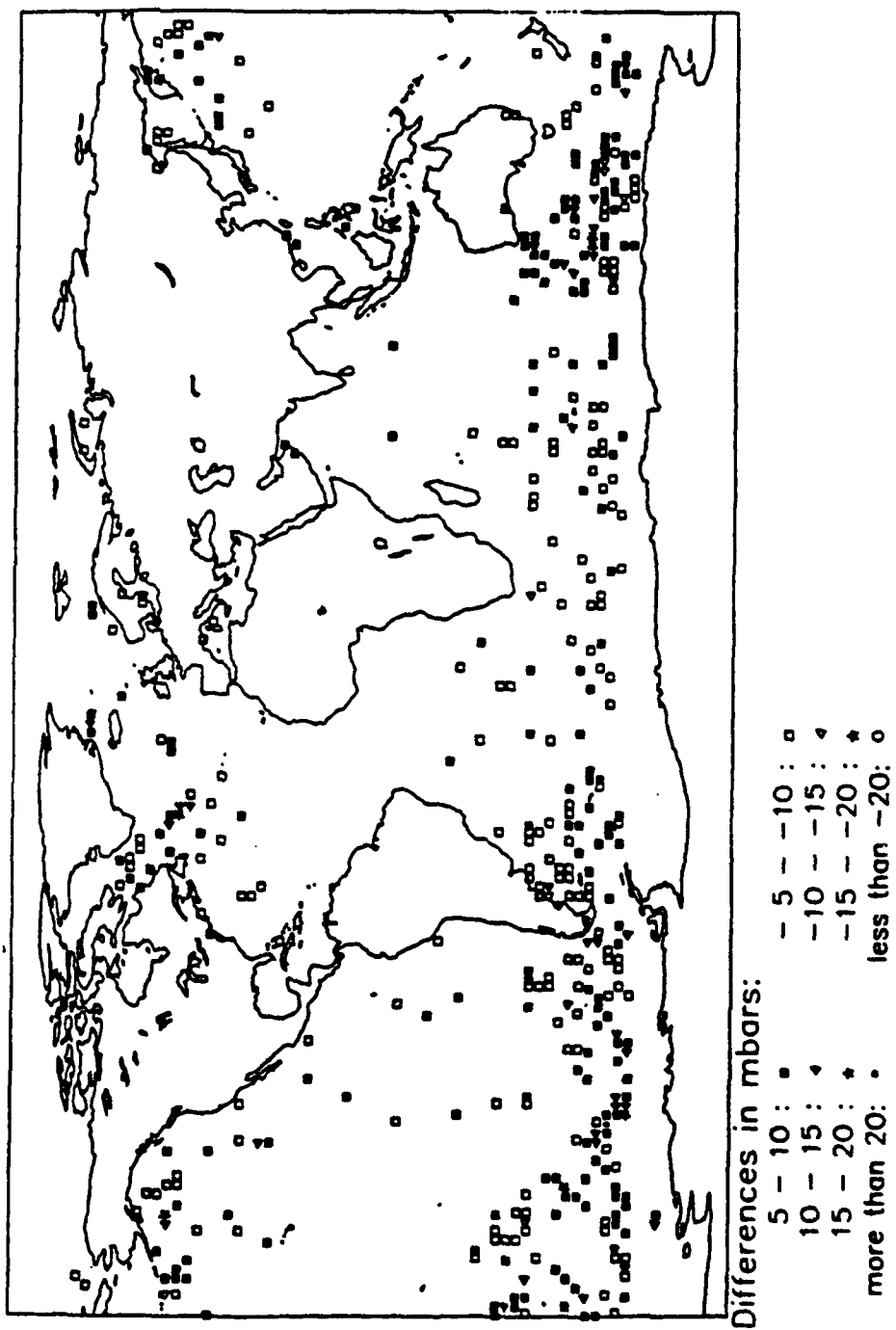
Figure V.1

53

Differences in mbars:
5 – 10 : ■
10 – 15 : ▼
15 – 20 : ★
more than 20: ●

– 5 – –10 : □
–10 – –15 : ▽
–15 – –20 : ☆
less than –20: ○

Figure V.2

Differences in mbars:

10 – 20 : ∎		–10 – –20 : ▫	
20 – 30 : ▼		–20 – –30 : ▼	
30 – 40 : ★		–30 – –40 : ★	
		less than –40: ○	

Figure V.3

Figure V.4

Figure V.5

Differences in mbars:

5 – 10 : ■   – 5 – –10 : □
10 – 15 : ▼   –10 – –15 : ▽
15 – 20 : ★   –15 – –20 : ☆
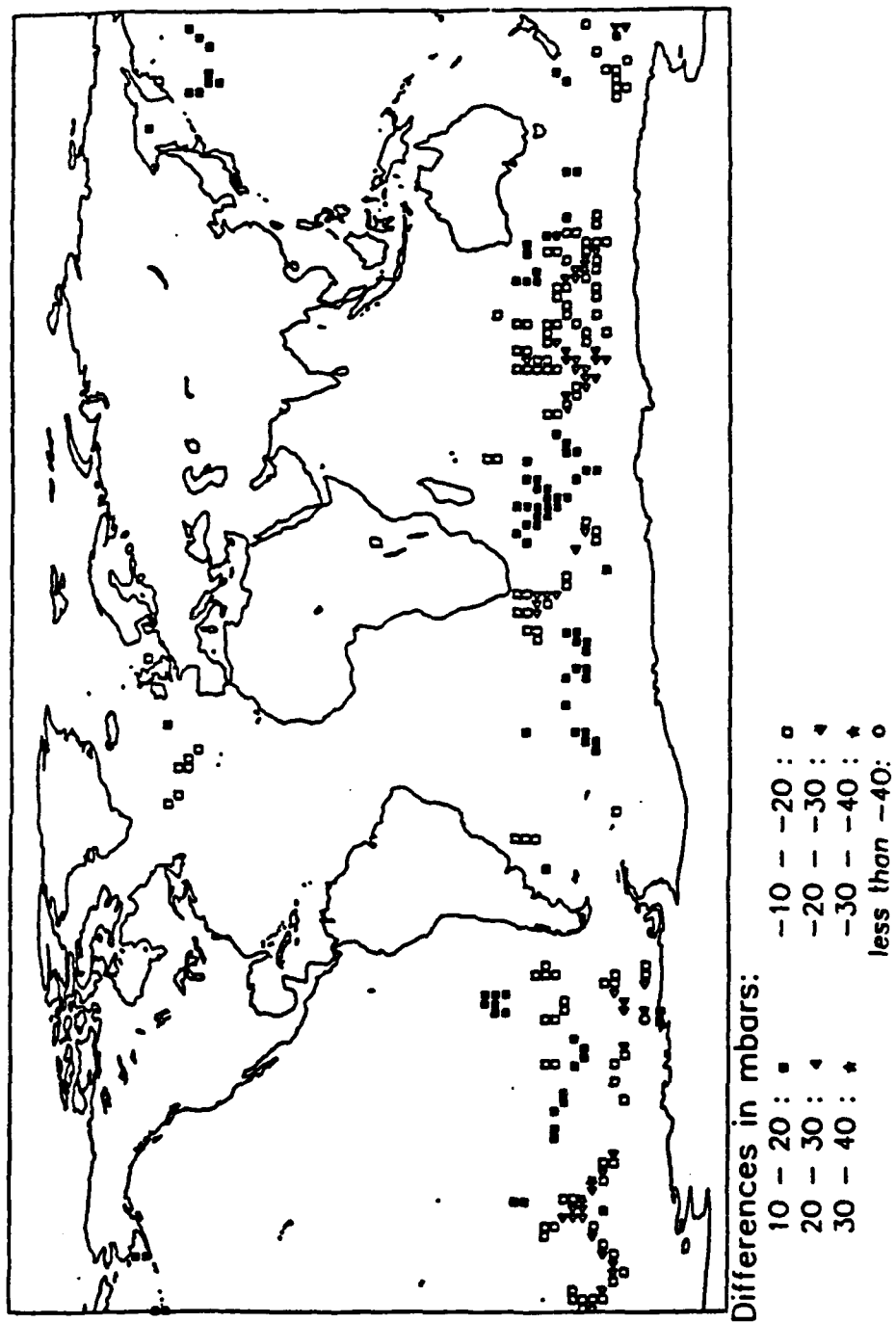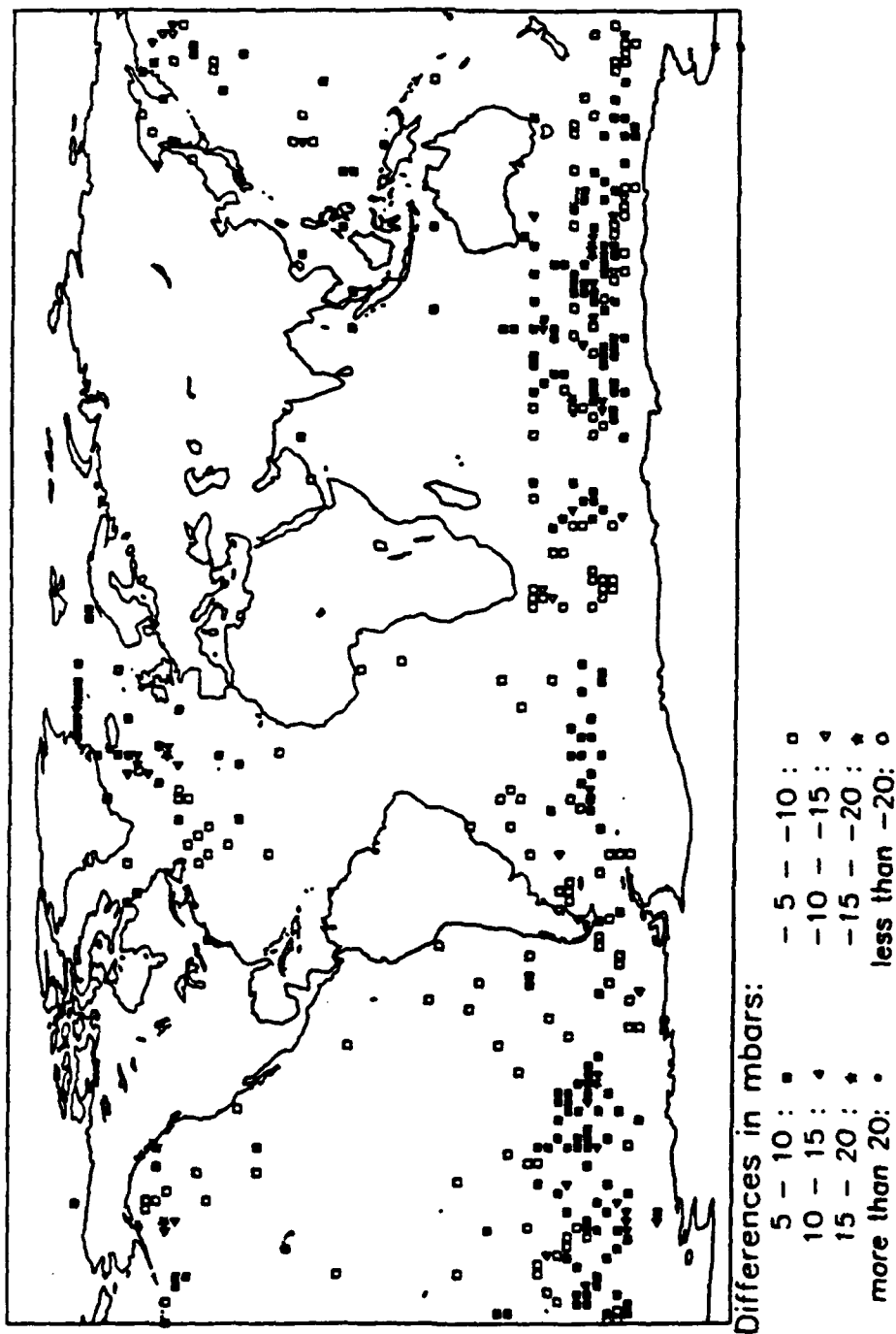more than 20: ●   less than –20: ○

Figure V.6

CHAPTER VI

SPECTROSCOPIC ANALYSIS OF GLOBAL TIDE GAUGE SEA LEVEL DATA

SUMMARY

Yearly and monthly tide gauge sea level data from around the globe are fitted to numerically generated tidal data to search for the 18.6 year lunar nodal tide and 14 month pole tide. Both tides are clearly evident in the results, with amplitudes and phases that are consistent with a global equilibrium response. Global atmospheric pressure data are fitted to global, monthly sea level data to study the response of the ocean to pressure fluctuations. The global response of sea level to pressure is found to be inverted barometer at periods greater than two months.

A large coherence at 437 days between pressure and sea level data is found for the North Sea, Baltic Sea and the Gulf of Bothnia. The results are not entirely conclusive, but they tend to support O'Connor's suggestion [1986] that the apparent enhanced pole tide in these basins may be due to meteorological forcing rather than to a basin-scale resonance.

Finally, global averages of tide gauge data, after correcting for the effects of post glacial rebound on individual station records, reveal an increase in sea level over the last 80 years of between 1.1 mm/yr and 1.9 mm/yr. As part of the process of removing the effects of post-glacial rebound, we fit those effects to the global tide gauge data and obtain very good agreement with results predicted from post-glacial rebound models. This tends to support the post-glacial model results and it suggests that the global tide gauge data are, indeed, capable of resolving changes in sea level at the mm/yr level.

INTRODUCTION

Long period ocean tides affect estimates of certain geophysical parameters, in some cases through oceanic contributions to the Earth's inertia tensor and, in others, through crustal deformation caused by the tidal loading. Two examples of such estimates are the use of satellite solutions for the earth's J_2 gravity coefficient to constrain mantle anelasticity at the lunar tidal period of 18.6 years, and the use of the observed period and damping of the Chandler wobble to estimate anelasticity at the 14 month wobble period.

The 18.6 year solid-Earth and ocean tides, related to the precession of the lunar nodes, cause an 18.6 year variation in J_2. Lambeck and Nakiboglu [1983] assumed the ocean tide was equilibrium (for an 'equilibrium' tide, the sea surface is a surface of constant potential) and used Rubincam's [1984] observed 18.6 year variability in J_2 to constrain the value of mantle anelasticity at this period. The result was surprisingly large. To help assess the importance of the equilibrium ocean tide assumption on the conclusion, we note that if the earth were assumed to be elastic, Rubincam's result would imply an 18.6 year ocean tide that was twice equilibrium. The J_2 result should continue to improve as more satellite data are acquired.

The Chandler wobble constraint on anelasticity [see, for example, Smith and Dahlen, 1981] depends critically on the response of the ocean to the incremental centrifugal force caused by the wobble. That response, called the pole tide, is known to affect the period and, if it were non-equilibrium, could contribute to the damping. In fact, a global departure from equilibrium of only 10 percent could have observable consequences. Theoretical models for the pole tide in the deep ocean suggest the pole tide should be equilibrium [O'Connor and Starr, 1983; Carton and Wahr, 1986; Dickman, 1988a]. However, the pole tide in the North and Baltic Seas and in the Gulf of Bothnia is apparently several times the

59

equilibrium value [Miller and Wunsch, 1973]. Wunsch [1986] postulated that this enhanced tide may be due to a local oceanic resonance in the region. Alternatively, O'Connor [1986] suggested that the apparent 14 month spectral peak could be caused by meteorological forcing and is not related to the pole tide.

The response of the ocean to variations in atmospheric pressure is another oceanographic disturbance with implications for solid earth geophysics. An inverted barometer response (ie. a 10 mm depression of sea level for every 1 mbar increase in pressure) is suggested by analytical models [see, eg., Wunsch, 1972; Munk and MacDonald, 1975; Dickman, 1988b]. The inverted barometer assumption has been invoked when studying the effects of atmospheric pressure on the Earth's rotation [see, eg., Munk and Hassan, 1961; Wilson and Haubrich, 1976; Merriam, 1982; Wahr, 1983] and when estimating the crustal deformation caused by pressure fluctuations [Rabbel and Zschau, 1985; Van Dam and Wahr, 1987]. The results in both cases are sensitive to the accuracy of this assumption. It is also important to understand the pressure response in order to interpret observed sea level variability in terms of wind-driven ocean currents. For example, oceanographers who process altimeter data to learn about the wind-driven response, usually remove an inverted barometer pressure response during data pre-processing.

Climate models that are used to study the effects of atmospheric greenhouse gasses predict an increase in the global temperature over the next century of from 1 to 4 degrees centigrade [Hansen, et al., 1981]. An increase of this magnitude could have numerous catastrophic effects, not the least of which would be a global rise in sea level due to a combination of melting polar ice caps and the thermal expansion of sea water. One of the important goals of global change studies is to improve our understanding of this variability in water storage.

There have been previous attempts to use tide gauge data to constrain the 18.6 year and 14 month tides [see, eg., Munk and Cartwright, 1966; Cartwright and Tayler, 1971; Miller and Wunsch, 1973; and Hosoyama, et al., 1976] the response of the ocean to atmospheric pressure [Chelton and Enfield 1986] and the global rise in sea level [Emery, 1980; Gornitz and Lebedeff, 1982; Barnett, 1983; Peltier, 1986]. These studies have primarily involved the analysis of data from individual tide gauges or, at most, from a small subset of all available stations.

In the present study, we combine tide gauge data from several hundred stations scattered around the globe, to test the hypotheses that the global 18.6 year and 14 month tides are equilibrium, and that the response to pressure is inverted barometer. Our tide gauge data set consists of monthly sea level values obtained from the Permanent Service for Mean Sea-Level (PSMSL), at Bidston, England [see Pugh and Faull, 1983a]. The distribution of the 721 stations over the globe is shown in [Pugh and Faull, 1983b]. In all cases, our observational results are consistent with these hypotheses. (Although the time resolution of the data limits the investigation of the pressure-driven response to forcing periods of greater than two months).

We investigate the possible causes of the apparently enhanced pole tide in the North Sea region. Our comparisons between tide gauge and pressure data tend to support the hypothesis that the spectral peak is due to narrow-band meteorological forcing in the region, rather than to a basin-scale resonance. Our conclusions, though, should be regarded as tentative, because the dominant meteorological forcing would be due to winds, but we did not include wind data in our analysis.

We also use the PSMSL data to constrain the global rise in sea level. Although our estimates vary somewhat, depending on how we restrict the data and correct for post glacial rebound [see eg., Peltier, 1986] we infer a global sea level rise of between 1.1 mm/yr and 1.9 mm/yr, with a preferred value of 1.75 mm/yr for stations in the regions covered by Peltier's model. In the process of correcting for the effects of post glacial rebound, we least squares fit Peltier's [1986] predicted vertical uplift to the data, and find very good agreement (ie. a fit with a value close to 1).

60

In this section, we describe two methods we use to help identify small signals in the global tide gauge data. We use the least squares fit technique to study the ocean's response to atmospheric pressure. And, we stack the data to investigate the 18.6 year tide and the 14 month tide. We use both techniques to study the global rise in sea level and the effects of post glacial rebound. We use the monthly PSMSL data to study the pole tide and the response to atmospheric pressure. We use yearly averages of the PSMSL data to study the 18.6 year tide and the global rise in sea level.

Least squares fit

Let $s_k(t)$ and $p_k(t)$ represent the time dependent fluctuations in sea level and in pressure at tide gauge k. Separate the observed sea level fluctuations into a component caused by the pressure, and a remainder, $\varepsilon_k(t)$, due to a combination of wind-driven fluctuations, tides, and observational noise. Suppose that the pressure-induced variability at an individual tide gauge depends on the past, present, and future values of pressure as measured at that gauge alone. (Except in cases where the arrival of pressure-driven waves precedes the arrival of the change in pressure, causality precludes dependence on the future, but by solving for that dependence we can partially assess the accuracy of our results.) Then, the most general linear relationship between s_k and p_k is:

$$s_k(t) = \int_{-\infty}^{\infty} A(\tau) p_k(t-\tau)\, d\tau + \varepsilon_k(t) \tag{1}$$

Here, $A(\tau)$ can be interpreted physically as a Green's function describing the response of the ocean to an impulsive pressure disturbance (the true Green's function would actually be more complicated than $A(\tau)$, since equation (1) assumes that sea level at any point is unaffected by pressure disturbances at other points). Since the ocean has a finite memory, $A(\tau)$ should approach zero for large τ.

Suppose that both $s_k(t)$ and $p_k(t)$ are discretized to a time series of monthly values, $t=t_i$, and suppose $A(\tau)$ is negligible for $|\tau| > Lt_i$, where L is an integer. If Δt is the sampling interval (equal to one month in our case), then (1) reduces to the discrete form:

$$s_k(t_j) = \sum_{i=-L}^{L} A(t_i) p_k(t_j-t_i)\Delta t + \varepsilon_k(t_j) \tag{2}$$

For an inverted barometer ocean, $A(0)$ would be -10.1 mm/mbar [see Wunsch, 1972], and all other $A(t_i)$ would be zero.

Suppose $A(t_i)$ is independent of the tide gauge location. This is equivalent to assuming that the ocean responds to pressure in the same way at every location. Then, we can estimate $A(t_i)$ for each t_i by least squares fitting to all PSMSL tide gauge data simultaneously. We can least squares fit each $A(t_i)$ individually, or all the $A(t_i)$ simultaneously. As an example, if each data point is given equal weight, regardless of where or when it was taken, and if M_k is the total number of months in the time series for tide gauge k, then the least squares fit for an individual $A(t_i)$ gives:

$$A(t_i) = \frac{\displaystyle\sum_{k=\text{gauge}} \sum_{j=1}^{M_k} s_k(t_j) p_k(t_j-t_i)}{\displaystyle\sum_{k=\text{gauge}} \sum_{j=1}^{M_k} p_k(t_j-t_i) p_k(t_j-t_i)} \tag{3}$$

As another application, the PSMSL data are simultaneously fit to theoretically predicted post glacial rebound data and to a global linear trend, to estimate the global rise in sea level and to help assess the rebound models. The rebound data are constructed from the linear trends predicted for each station by the models, and are identical to the PSMSL data in coverage and gaps. Whereas the effects of ice melting and thermal expansion on sea level is assumed here to be independent of position, the linear trends due to post glacial rebound are not. To the extent the rebound varies with position, it may be separated from the general increase in sea level by the simultaneous fit. The fit to the rebound model gives information on which stations should be included in the simultaneous fit, as described below. It also allows us to partially assess the accuracy of the rebound models, and of the global sea level rise inferred from the tide gauge data.

Stacking

The procedure of stacking multi-station data to enhance small signals has been used by seismologists to improve their estimates of the Earth's free oscillation eigenfrequencies [Gilbert and Dziewonski, 1975], and to search for short period oceanic normal modes in the Pacific [Luther, 1982]. Stacking is particularly useful in cases where the spatial dependence of the signal is known beforehand.

Suppose we want to test the hypothesis that the 18.6 year tide is equilibrium. The 18.6 year equilibrium amplitude at co-latitude θ, eastward longitude λ, and time t, has the form (using the corrected tables of tidal harmonics from Cartwright and Edden [1973]):

$$H(t,\theta,\lambda) = 27.94 \; \zeta(\theta,\lambda) \cos(\omega t + \phi) \qquad \text{mm} \qquad (4)$$

where ω is the frequency of the 18.6-year tide and ϕ is the phase at $t=0$. The function $\zeta(\theta,\lambda)$ represents the spatial dependence of the equilibrium tide, and would equal $(1+k-h)Y_2^0$ were it not for mass conservation of the oceans, sea floor loading, and gravitational self attraction (h and k are tidal Love numbers, and the spherical harmonic Y_2^0 is normalized so that the integral over the unit sphere of $|Y_2^0|^2$ is one). These latter effects cause the introduction of other spherical harmonics into $\zeta(\theta,\lambda)$ and increase the Y_2^0 component by about 10 percent. The function $\zeta(\theta,\lambda)$ can be found by iterative solution of equation (102) in Dahlen, [1976].

Once we have found $\zeta(\theta,\lambda)$, we least squares fit it to all the PSMSL tide gauge data at each time t (see equation 6, below). The average and the secular trend are removed from each station prior to the fit. The resulting time series of fit values is referred to here as a stack. The stack is spectrally analyzed to search for a peak at the 18.6 year frequency, ω. If a peak is found, its amplitude and phase can be compared with the results that would be expected for an equilibrium tide. To estimate these equilibrium results, an synthetic data set is constructed by replacing the PSMSL sea level value at every gauge and at every time by the estimated equilibrium value, $h(t,\theta,\lambda)$ in (4), at that same position and time. The synthetic data, like the PSMSL data, are stacked against the equilibrium spatial dependence $\zeta(\theta,\lambda)$ and the amplitude and phase of the spectral peak at 18.6 years are estimated.

Good agreement between these stacks of PSMSL and synthetic data is not enough to guarantee that the tide is equilibrium. It is desirable to also stack against other functions of θ and λ. For example, the equilibrium $\zeta(\theta,\lambda)$ for the 18.6 year tide is nearly proportional to $Y_2^0(\theta,\lambda)$. We stack against other spherical harmonics as well, up to degree 6. These additional stacks serve two purposes. First, by stacking the synthetic data we can assess the effectiveness of the stacking procedure. For instance, is the station coverage complete enough that different spherical harmonics are reasonably orthogonal? We find that it is. Second, by stacking the PSMSL data and looking at the spectra, we can further test the equilibrium assumption. For example, if the data are stacked against a spherical harmonic other than Y_2^0, and if the 18.6 year tide is equilibrium, then there should not be a notable peak at 18.6 years in the spectrum of the stack. Although we do not show results here for these other stacks, we find no evidence of 18.6 year peaks that stand significantly above the noise continuum for any stacks against pure spherical harmonics other than Y_2^0. We compare these PSMSL results with Y_l^m stacks of the synthetic

62

data, and find that the 18.6 year peaks in the synthetic stacks are also below the noise continuum of the PSMSL spectra. These results, then, are consistent with the equilibrium hypothesis. That hypothesis is addressed further, below, when we discuss the stacks against the equilibrium $\zeta(\theta,\lambda)$.

A similar procedure is used to investigate the 14 month pole tide. The equilibrium pole tide is generated from polar motion data (we use polar motion values from the International Latitude Observatory of Mizusawa; see Yumi and Yokoyama, 1980) according to:

$$H(t,\theta,\lambda) = \frac{-3\Omega^2 a^2}{2g} \, \mathrm{Re} \left[\left[m_1(t) + im_2(t) \right] \zeta(\theta,\lambda) \right]$$

(5)

Here, $m_1(t)$ and $m_2(t)$ are the $\hat{x}$ and $\hat{y}$ coordinates of the pole position (with magnitude up to one third of an arc second), Ω and a are the Earth's mean rotation rate and radius, and Re denotes the real part. The spatial dependence, $\zeta(\theta,\lambda)$, in (5) is complex, and so when it is least squares fit to the PSMSL data it gives a complex stack. In the absence of sea floor loading, gravitational self attraction, and mass conservation, $\zeta(\theta,\lambda)$ would equal $(1+k-h)Y_2^1(\theta,\lambda)$. As in the case of the 18.6 year tide, $\zeta(\theta,\lambda)$ is modified by about 10% due to these additional effects, and it can be estimated as described by Dahlen [1976]. Stacks against the equilibrium $\zeta(\theta,\lambda)$ are described below. Stacks of the PSMSL data against spherical harmonics other than Y_2^1 do not exhibit significant peaks at the 14 month pole tide period, and are consistent with Y_l^m stacks of the synthetic data.

For any of these examples, the least squares fit to form a stack can either be weighted or unweighted. One weighting procedure we find to be particularly useful involves stacking on a grid. The earth's surface is divided into grid elements, in our case either $10°$ latitude by $20°$ longitude or $15°$ latitude by $30°$ longitude. Sea level heights for each station (with secular trends and station averages removed) are multiplied by the equilibrium spatial dependence, $\zeta(\theta,\lambda)$, and the results are averaged over individual grid elements for a given time, t. A global average is then constructed by summing the grid averages. The final result is normalized by dividing by the global average of the equilibrium data. The resulting time series is the weighted stack.

For example, let $s_k(t)$ be the tide gauge reading for station k at time t, with the secular trend and station average removed. Let θ_k and λ_k be the co-latitude and eastward longitude of station k. Let $n_p(t)$ be the total number of gauge measurements in grid element p at time t, and suppose there are N grid points. Then, the complex gridded stack, $x(t)$, is defined as

$$x(t) = \frac{\displaystyle\sum_{p=1}^{N} \frac{1}{n_p(t)} \sum_{\substack{k=\text{gauges} \\ \text{in } p}} s_k(t) \, \zeta(\theta_k,\lambda_k)}{\displaystyle\sum_{p=1}^{N} \frac{1}{n_p(t)} \sum_{\substack{k=\text{gauges} \\ \text{in } p}} \zeta^*(\theta_k,\lambda_k) \, \zeta(\theta_k,\lambda_k)}$$

(6)

Here * denotes complex conjugation. This result, (6), is equivalent to a weighted least squares fit of ζ to the data at time t, and it reduces to an ungridded, unweighted stack when the grid elements are so small that $n_p(t) = 1$ for every p.

Individual station records exhibit considerable long period variability, most of it probably caused by forcing from surface winds. This makes it difficult to use a single tide gauge record to identify any of the long wavelength spectral features we are considering here. Stacking the individual stations against the spatial dependence of the equilibrium solution amplifies any signal with that spatial dependence, and this can significantly reduce the correlation with the wind-driven variability.

The use of a grid de-emphasizes areas with great concentrations of stations, such as northern Europe and Japan, by weighting them equally with areas of fewer stations. Gridding also tends to further reduce the contamination from long wavelength, wind-driven features. Roughly speaking, the contamination of the final stack is reduced when the wind-driven signal has wavelengths much longer than the grid size,

63

but is increased at shorter wavelengths.

For example, imagine a situation where there are 10 stations: 9 within grid element A and 1 within a far distant grid element B. If the wind-driven signal has a wavelength much longer than the grid size, then within grid element A that signal is highly correlated with the long wavelength feature we are interested in: both are nearly constant across the element. In that case, an ungridded stack would not effectively remove the wind-driven signal, since the stack would be dominated by the high correlation at the 9 stations within A. A gridded stack would be more effective, since then the 9 elements in A would be weighted equally with the 1 element in B, and thus the stack could more effectively exploit any differences between the signals at A and B.

On the other hand, since isolated stations contribute more heavily to a gridded stack, that stack is more sensitive to noise in those individual station records. The sizes of the grids used here are chosen to be large enough to minimize the effects of wind-driven fluctuations and of gaps in the grid averages, but smaller than the wavelength of the dominant spherical harmonic in the stacking function. The yearly data are stacked on a coarser grid than are the monthly data. In each case, the grid size that is selected is the one for which the background noise for the stack is minimized.

Subtracting the average tide gauge height for each station prior to a stack is necessary to establish a uniform benchmark for all stations. But, if a station does not report data over the entire time span of the stack, the computed station average is not the true average, and this can introduce systematic errors into the spectrum. (Of the 721 stations in the PSMSL data set, only 7 cover the entire interval between 1900 and 1979.) The frequency content of these errors depends on the time spans of the individual station data. The errors are likely to be important at periods close to and longer than the average of the station lengths. Although we have found no consistent way of eliminating these errors, we have attempted to minimize their impact by only including stations with data spans that are longer than the period of the signal we are looking for (at least when we can define that period). The pole tide results are not particularly sensitive to this problem since the average station length for all PSMSL stations is 29 years, which is many times the period of the tide.

Fitting and removing secular trends from stations prior to stacking is found to remove another source of error, as power associated with these trends can leak into the spectral band of interest. In addition, before any spectral analysis is performed on the final stacks, a secular trend and an average are removed from the final time series. (Even if trends and averages are removed from the individual station data, there can still be a trend and a non-zero average in the stacked data, if the stack is weighted, because an individual station does not, in general, report data over the entire time span of the stack.)

The spectral methods employed here to analyze a stack include finding conventional amplitude and coherence spectra, and using the more sophisticated multi-taper method developed by Thomson [1982] to minimize spectral leakage and adapted for geophysical applications by Lindbergh et al. [1987]. For the multi-taper technique, the data are multiplied by one of six prolate spheroidal sequences, or tapers, to create six time series. A spectrum is then constructed from the discrete Fourier transforms of each of these series following section 3, part 1, of Lindbergh, et al. [1987]. A statistical F-test provides a confidence estimate that an apparent periodicity in the spectrum is truly sinusoidal.

The conventional amplitude spectra shown here all employ a cosine taper. Following convention, we construct complex Fourier transforms as twice the real transform, and the amplitude spectrum is the absolute value of the complex Fourier transform. All of the amplitude spectra shown in the figures are overresolved. By this, we mean that the absolute amplitude is computed at more frequent intervals than the elementary bandwidths, in order to obtain a clearer idea of where the actual peaks lie. To find the coherence at frequency ω between two time series, the time series are multiplied by a cosine taper, and the average coherence across seven elementary bandwidths centered on ω is calculated according to (equation (5) of Wilson and Haubrich [1976]). With this choice for the coherence spectrum, we can be 95% confident that two series are correlated at ω, if the coherence at ω is larger than 0.43 . Other choices of tapers and bandwidths are possible [see Chao, 1988].

RESULTS

The response to pressure.

Figure VI.1 shows a plot of the least squares fit parameter, $A(\tau)$ (equation (3) with $t_i = \tau$), between sea level and atmospheric pressure, for lag times of up to $\pm$ 240 months. The pressure data are obtained from an objective analysis of global station pressure data for January, 1900 - April, 1973 [Wahr, 1983], and so we restrict the PSMSL data to this time period. Seasonal effects are removed from both sea level and pressure data sets prior to the fit.

All PSMSL stations during this time period are included in the fit shown in Figure VI.1, except for those in the North and Baltic Seas and in the Gulf of Bothnia. As shown below, the Baltic Sea and Gulf of Bothnia do not appear to be inverted barometer (although the North Sea does). Furthermore, by omitting these 3 shallow seas from the data, we end up using the same data subset in Figure VI.1 that we will use later to study the global pole tide.

The result for $A(0)$ is -10.1 mm/mbar for the fit shown in Figure VI.1. The results for all other $A(\tau)$ are close to zero, with an rms value of .5 mm/mbar. Consequently, we assign $\pm$ .5 mm/mbar to be the uncertainty in our estimate of $A(0)$. Since wind data were not analyzed, there is no way for us to separate the contribution of winds to the fit to pressure. There should be a temporal correlation between winds and pressure at each each tide gauge. Our hope is that there are enough stations over a wide enough area in the global average to break the spatial correlation between winds and pressure. Without wind data we cannot confirm that this has happened, but the results shown in Figure VI.1 are at least consistent with an inverted barometer response of the oceans to pressure at periods of two months and longer.

The response for zero lag for other sets of stations is as follows:

center, delim (), tab(!); l l c. Global oceans including all shallow basins:!$A(0)$= -12.1 $\pm$ .9 mm/mbar,!574 stations Northern hemisphere excluding North Sea region:!$A(0)$= -10.0 $\pm$ .5 mm/mbar,!407 stations Eastern hemisphere excluding North Sea region:!$A(0)$= -10.3 $\pm$ .7 mm/mbar,!234 stations Southern hemisphere:!$A(0)$= -10.9 $\pm$ 1.1 mm/mbar,!80 stations Western hemisphere:!$A(0)$= -9.9 $\pm$ .6 mm/mbar,!253 stations North Sea:!$A(0)$= -9.7 $\pm$ .9 mm/mbar,!26 stations Baltic Sea:!$A(0)$= -12.5 $\pm$ 1.3 mm/mbar,!42 stations Gulf of Bothnia:!$A(0)$= -16.2 $\pm$ 1.7 mm/mbar,!19 stations Mediterranean Sea:!$A(0)$= -14.4 $\pm$ 1.2 mm/mbar,!33 stations

In all these fits, the $A(\tau)$ for $\tau \neq 0$ are close to zero. The rms values for these other $A(\tau)$ are shown as the uncertainties for $A(0)$. Note that as the number of stations included in the fit decreases, the rms value for $A(\tau)$ with $\tau \neq 0$ increases.

These results include examples of shallow basins where the deviation from the inverted barometer response for $A(0)$ exceeds the rms value of the other $A(\tau)$'s. This does not necessarily imply a true non-inverted barometer response, because the rms value does not adequately represent everything that could bias the fit. In particular, wind-driven changes in sea level could be correlated with surface pressure, and thus could affect our estimate of $A(0)$ without contributing noticeably to $A(\tau)$ for $\tau \neq 0$. This is apt to be a particular problem when considering small regions at a time, such as the Baltic Sea and the Gulf of Bothnia, since then there is likely to be greater spatial coherence between the wind and pressure fields.

65

The pole tide.

Monthly tide gauge data are stacked, as described above, to study the pole tide. Before stacking the data, we remove the effects of atmospheric pressure, computed using the inverted barometer assumption. Again, we restrict our analysis to January, 1900 - April, 1973. We find that, for stations outside the North Sea, Baltic Sea, and Gulf of Bothnia, the removal of pressure affects the pole tide amplitude inferred below by about 10 percent.

In this and the succeeding analysis involving the pole tide, stations in the North and Baltic Seas and in the Gulf of Bothnia are removed from the data as there is an anomalously large spectral peak for this region at periods close to the pole tide period of 434 to 437 days [see, for example, Miller and Wunsch, 1973]. An equilibrium stack of 26 stations in the North Sea reveals the PSMSL amplitude at the 437 day period to be 3.6 times the equilibrium amplitude, for the 42 Baltic Sea stations the PSMSL amplitude is 6.2 times equilibrium, and for the 19 stations in the Gulf of Bothnia, the PSMSL amplitude exceeds the equilibrium amplitude by a factor of 9.

The beat period between the pole tide period and one year is approximately 60 months. To minimize the correlation with the annual period, we choose to include in our global analysis only those stations having greater than 60 months of data. This leaves us with 487 stations out of the original 721 in the full PSMSL data set.

Figure VI.2 (a) shows ungridded amplitude spectra for Y_2^1 stacks of these 487 stations. Figure VI.2 (b) shows the spectra of the stacks averaged on a $10°$ by $20°$ grid. Shown are the spectra for the PSMSL data, for the synthetic (ie. equilibrium) data, and for differenced data. The differenced data are generated by subtracting the synthetic time series from the PSMSL time series. Note that in Figure VI.2 the spectra for both the PSMSL data and the synthetic data show a double peak for the pole tide, with one peak at 427 days and the other at 437 days. This is a well known feature of the polar motion spectrum. Most of the signal contributing to this double peak is from data early in the time series. The two peaks are close enough together that their resolution requires most of the 74 years of the data span.

In both the gridded and non-gridded stacks the pole tide is clearly evident in the spectrum for the PSMSL data and there is good visual agreement with the synthetic data. The agreement is particularly good for the gridded results. In both cases, the differenced data does not have the characteristic double peak spectrum, indicating that the PSMSL stack is similar to the equilibrium stack in amplitude and phase.

To evaluate the agreement quantitatively, we compute amplitudes for both the PSMSL and the synthetic data sets. First, the amplitudes at the frequencies of the two apparent pole tide peaks are computed, and the results from the PSMSL data and synthetic data are compared. We find, for the ungridded data shown in Figure VI.2 (a), that the amplitude of the 427 day peak in the PSMSL data is .99 ± .28 times the synthetic amplitude, and that of the 437 day peak is .74 ± .27 times the synthetic.

We then repeat this procedure, but for the gridded stacks in Figure VI.2 (b). In this case, the 427 day and 437 day amplitude ratios are 1.01 ± .18 and .96 ± .17 respectively. The uncertainties for both the gridded and ungridded results are obtained from visual estimates of the signal-to-noise ratio at the pole tide frequency, and assuming the worst case: that the amplitudes of the signal and the noise are additive (in other words, that the noise is either in-phase or $180°$ out-of-phase with the signal). The background amplitude used to obtain the signal-to-noise ratio is 1.0 mm for both the ungridded and gridded stacks.

To estimate the phase difference between the PSMSL and the synthetic data and to obtain another estimate for the amplitude ratio, we fit the synthetic data to the PSMSL data using a complex constant, after a filter is used to extract, from both time series, the power in a spectral band centered over the two pole tide frequencies (.068-.073 c/mo). The power in the spectral band of interest is extracted so that the band at the annual period and the low frequency power does not affect the estimate of phase (there is a residual spectral peak centered around 1 c/yr, even though an annual term has been fit and removed from the data). The phase difference between the PSMSL and the synthetic data is small for both the gridded and ungridded stacks. The PSMSL leads the synthetic data in the ungridded stacks by $3° ± 50°$ and the overall amplitude ratio is .83 ± .27; roughly the average of the amplitude ratios taken for each

spectral peak separately. For the gridded data the PSMSL leads the synthetic data by $0° \pm 46°$ and the amplitude ratio is $.96 \pm .18$. A phase lead, δ, is defined here so that if the equilibrium tide is proportional to $\cos(\omega t - \lambda)$, where λ is eastward longitude and ω is the (positive) pole tide frequency, then the observed ocean tide is proportional to $\cos(\omega t - \lambda + \delta)$. Each degree of phase lead represents a time lead of approximately 1.2 days.

To estimate the uncertainty in the phase, we note that the amplitude uncertainty found from the signal-to noise ratio, as described above, mostly reflects the uncertainty in the in-phase component. We assume the uncertainty in the out-of-phase component is just as large, and compute the resulting bounds on the phase. This procedure results in a larger uncertainty than that predicted from the formal error of the fit.

We have also computed the multi-taper spectrum, as described above, for the gridded equilibrium stack. The results do not differ significantly from the conventional spectral results, probably because the cosine taper in the conventional spectra is sufficient to exclude the majority of spectral leakage into the pole tide band.

Taken together, the Y_2^1 stacks of monthly data suggest that the pole tide amplitude is $.9 \pm .3$ times the equilibrium amplitude, and that the actual ocean tide leads the equilibrium pole tide by $2° \pm 48°$.

The enhanced pole tide in the North Seas.

Figure VI.3 (a) shows untapered amplitude spectra of surface pressure, PSMSL sea level data, and the equilibrium pole tide stacked against Y_2^1, for the North Sea. The surface pressure results are obtained by multiplying the pressure data described above by the inverted barometer factor of 10 mm/mbar, and then replacing each tide gauge reading with the inverted barometer value at the time and location of that reading. Figures VI.3 (b) and (c) show the same spectra for the Baltic Sea and Gulf of Bothnia respectively. For these small seas, a Y_2^1 stack is not much different than a spatial average. The same spectra are plotted for the 487 stations that span the remainder of the globe in Figure VI.3 (d). In all the figures, amplitude is shown instead of power to compare the three disparate spectra most clearly. Note that in all three shallow seas, there is a pronounced sea level peak in the pole tide band, that stands well above the equilibrium results.

We have attempted to interpret the 14 month peak in the sea level data in terms both of meteorological forcing [O'Connor, 1986] and of a local oceanic resonance [Wunsch, 1986]. We formulate two hypotheses. One is that there is a resonance that amplifies the response of this region to external forcing. Such a resonance should affect both the pole tide and the response to meteorological forcing. The other hypothesis is that there is no local resonance, but that the spectral peak in sea level is due to a combination of an equilibrium pole tide and a static response to meteorological forcing (ie. an inverted barometer response to pressure and a response to local winds). We assume the winds are correlated with the pressure in this frequency band, so that the total stacked response of the ocean to the meteorology is proportional to the stacked pressure data across this frequency band.

To assess these two hypotheses, we first note that for the three shallow basins, there is a pressure peak at the 437 day period, close to coincident with the pole tide period. In fact, the peaks in the sea level spectra appear to line up reasonably well with peaks in the pressure spectra. There seems to be less agreement between the sea level and equilibrium pole tide spectra. On the other hand, for the global results there is good apparent agreement between sea level and the equilibrium pole tide, and less similarity between sea level and pressure.

Coherence results tend to support this observation. Coherence spectra between Y_2^1 stacks of sea level and pressure are shown in Figure VI.4 (a) for the North Sea, Figure VI.4 (b) for the Baltic Sea, and Figure VI.4 (c) for the Gulf of Bothnia. The reason for using stacks against Y_2^1 instead of simple averages, is for consistency with the global results. To minimize spectral leakage from the annual into the pole tide bands, seasonal averages have been removed from all data from which coherence spectra are generated. For all three shallow basins, there is a correlation above the 95 per cent confidence level between sea level and pressure in the frequency band of the pole tide (a coherence estimate greater than

67

0.43). The coherence is particularly strong over the Gulf of Bothnia. Although there is a 5% chance that the large coherence is spurious, it is interesting that it occurs in a frequency band where there are large amplitude spectral peaks in both pressure and sea level. Figure VI.4 (d) shows the same coherence spectrum for the Y_2^1 stack of 487 stations outside the North Sea region. There, the correlation between pressure and sea level in the pole tide band is somewhat below the 95 per cent confidence level. (There is a large coherence at a period of about 460 days, just left of the pole tide band.)

Note that for all three shallow seas, there are narrow band estimates of coherence between sea level and pressure above the 95 per cent confidence level at several frequencies outside the pole tide band. While it is not unusual for the oceans to be stressed by winds and pressure enough to show enhanced coherence at a particular frequency, what is coincidental is the existence of a normal mode of the earth (the Chandler wobble) near one of the peaks in the local pressure spectrum, and the fact that the meteorological forcing in this case is concentrated in a frequency band that is about as narrow as the pole tide peak.

In order to test for the existence of a high Q periodic signal in the atmosphere, a statistical F-test was calculated from the Thomson spectrum of the pressure signal for these three regions. In all three regions, the F-test value is greater than the 90 per cent confidence level, suggesting, without any clues as to the cause, that there is a periodic signal in the atmosphere this region with a period of 14 months. The F-test exceeds the 90 per cent confidence level in several other frequency bands as well.

We are not suggesting that this is evidence of a pole tide in the atmosphere. In fact, the 14 month pressure peak is not a unique feature of the pressure spectrum (see Figure VI.5 (c), below, where the 14 month peak for pressure does not stand out among the other peaks).

To test for the existence of a resonance response of the shallow basins, the sea level data for each basin are fit in the frequency domain to resonant pressure and polar motion responses. For example, let $y(\omega)$ be the Fourier transform of the stacked data. Since wind data are not included here, we attempt to account for the wind-driven response by assuming it is proportional to the response to pressure. Then, we parameterize $y(\omega)$ using:

$$y(\omega) = A \ p(\omega) + B \ r(\omega) + \frac{C \ p(\omega)}{\omega - \omega_o} + \frac{D \ r(\omega)}{\omega - \omega_o} + \varepsilon(\omega) \qquad (7)$$

Here, A and B are the factors that describe the static response to pressure and winds and to the polar motion forcing, respectively ($p(\omega)$ and $r(\omega)$ are the Fourier transforms of the pressure and equilibrium pole tide); C and D represent the resonant strengths for the meteorological forcing and the pole tide; ω_o is the proposed resonance frequency in the basin; and $\varepsilon(\omega)$ represents unmodeled effects, including noise. If the observed peak in the basin near the pole tide frequency band is due to wind forcing that is correlated with pressure, then C and D will be small, and $y(\omega)$ will be dominated by the static terms. If the observed peaks are due to a resonance, then C and D will not be small, and ω_o should, presumably, be close to the Chandler Wobble frequency.

First, we find the values of A, B, C, D, and ω_o that minimize $\varepsilon(\omega)$ in a least squares sense. The inversion for ω_o is non-linear, and so our procedure is to choose a great many values for ω_o near the pole tide frequency, and fit for A, B, C, and D for each of these ω_o. We then look for an ω_o which leads to a particularly pronounced decrease in the residuals. For all three basins, there are, indeed, pronounced reductions of the residuals when ω_o is near the 437 day peak in the pole tide band. But, we judge the results to be inconclusive, due to the high correlation between the two resonant terms and $B \ r(\omega)$: when ω_o is close to the pole tide period, it is difficult to separate the resonant term from the equilibrium tide.

Our second method of using (7) to test whether the data require an oceanic resonance, is to simultaneously fit and remove from the PSMSL stacks the non-resonant pressure and equilibrium pole tide (the terms proportional to A and B in eq. 7). We band-pass the data to extract the pole tide band, prior to the fit. Results from the fits suggest that the pole tide in these shallow seas is much closer to equilibrium than is suggested by simply comparing sea level with the equilibrium tidal amplitude. For example, the results of the North Sea fit imply that the pole tide has an amplitude of 1.2 ± 1.2 times the

68

equilibrium amplitude, and that the response to meteorology is 2.5 ± 1.3 times the inverted barometer pressure. For the Baltic Sea the fit to the equilibrium pole tide is 1.9 ± 2.1 fit to pressure is 5.4 ± 1.8. For the Gulf of Bothnia the fitted parameters are 1.7 ± 1.0 and 4.5 ± 0.4. These large formal errors on the fits are the direct result of large variances of small numbers of data points. The pole tide frequency band encompasses only 5 bin frequencies, hence the two-way fit has only 3 degrees of freedom. Note that none of the pole tide parameters are significantly different from unity. For any of these three basins, if the fitted pressure and pole tide are removed from the PSMSL stack, the spectrum of the residuals (not shown) exhibits none of the characteristics of the equilibrium pole tide spectrum.

To help assess how strongly the data require a pole tide amplitude greater than the equilibrium amplitude, we subtract the equilibrium pole tide from the data (parameter B in (7) is constrained to be unity), and then fit and remove the pressure (parameter A, alone) from the PSMSL stack. If the spectrum of the residuals show the characteristic double peak of the pole tide spectrum, then there is reason to suspect an amplified response. If not, then the fact that the amplitude of B exceeded unity in the previous fit may be attributed to noise leaking into that fit.

Figures VI.5 (a) and (b) show amplitude spectra of Y_2^1 stacks for the Baltic Sea and the Gulf of Bothnia. The sold line in each Figure VI.is the PSMSL data. The spectra of the PSMSL stack with pressure fitted and removed are the short dashed curves in Figures VI.5 (a) and (b). The long-dashed curves are the spectra of the residuals after subtracting the equilibrium pole tide (short dashed curve) and fitting and removing pressure from the PSMSL stack. The spectra show that the removal of non-resonant pressure removes the majority of the enhanced power at the pole tide frequency. The spectra of the residuals after subtracting the equilibrium pole tide and then fitting and removing pressure have a double peak but they do not follow the characteristic peaks of the equilibrium pole tide closely. The North Sea results (not shown) are similar.

The problems brought about by the lack of wind data in this analysis are illustrated in Figure VI.5 (c) which shows power spectra of Y_2^1 stacks of pressure (the dashed line) and PSMSL data (the solid line) over the Baltic Sea for a wide frequency band. The peak at the pole tide frequency in the pressure spectrum is evident, but it is not appreciably larger than other pressure peaks. On the other hand, the peak in the pole tide band for the PSMSL data does stand above other peaks in this red spectrum. We can also infer there is something unusual happening in the pole tide band from the least square fit coefficients given above. For example, we have seen that the fit to pressure for the Baltic Sea gives 5.4 ± 1.8 across the pole tide band alone, but that it gives 1.2 ± .1 if the data are not band-passed prior to the fit.

Why is there such a large peak in sea level but not in pressure at the pole tide frequency? There are several possible explanations. It could be that there is a broad oceanic resonance across this band that amplifies the response to the meteorology. Perhaps the wind forcing, but not the pressure, is especially large in this frequency band. Or, maybe the wind is more highly correlated with pressure in this band, so that the wind-driven and pressure-driven responses tend to add constructively.

We conclude that, overall, our results are most consistent with the hypothesis that meteorological forcing near the pole tide frequency is responsible for most of the spectral peak in sea level at 434-437 days. We emphasize that the PSMSL data that lie in the North sea region are limited to the basin perimeters and have small numbers of stations, that we did not examine wind data, and that the frequency band of interest is narrow. We are, thus, not willing to conclusively rule out resonance as a mechanism for the enhanced spectral peak in these basins.

The 18.6 year tide.

Yearly tide gauge data are stacked against the equilibrium 18.6 year tide for all 260 stations outside the Baltic Sea that reported at least 19 years of data. The Baltic Sea is the only geographic area where long period noise (there is a spectral peak at 22-23 years in the Baltic Sea) so seriously masks the 18.6 year signal as to affect the estimated phase of a global stack. We identify the Baltic Sea as a particularly noisy region as follows. First, annual and 18.6 year amplitudes are fitted and removed from the data. Then, the standard deviation for the stacked data set is calculated, and we obtain σ=39.5 mm.

69

The majority of stations with outliers greater than 3 σ are located in the Baltic Sea. The σ for the all stations outside the Baltic Sea is 34.8 mm. Data outliers are not removed from any of the 260 stations outside the Baltic Sea, as they do not affect the results for either the pole tide or the 18.6 year tide enough to justify subjectively altering the data by their removal.

Figure VI.6 shows PSMSL and synthetic stacks against the equilibrium $\zeta(\theta,\lambda)$ in the time domain. A variation of approximately 16-20 years may be seen in the PSMSL stack. Figure VI.7 (a) shows the amplitude spectra of ungridded equilibrium stacks. An 18.6 year peak stands out clearly above the noise in the PSMSL data, and has an amplitude 1.2 times the synthetic amplitude. The PSMSL results also show pronounced peaks at 13.3 and 11 year periods. The spectrum of the difference between the the synthetic and PSMSL data shows that most of the discrepancy between the PSMSL and synthetic data at the 18.6 year period may be attributed to noise, as the amplitude at the 18.6 year period is well below the noise continuum. The results suggest that the PSMSL and synthetic data agree well in both amplitude and phase at the 18.6 year period. Amplitude spectra for a stack against the equilibrium $\zeta(\theta,\lambda)$ on a 15° by 30° grid is shown in Figure VI.7 (b). The use of a coarse grid improves the agreement between the PSMSL and synthetic amplitude at 18.6 years.

A statistical F-test of the multi-taper spectrum of the unweighted, ungridded data is shown in Figure VI.8. (The multi-taper spectrum, itself, is not shown here. It gives results similar to those shown in Figure VI.7.) The F-test shows that we can be 95% percent confident that the 18.6 year signal of the PSMSL data is sinusoidal. Note that the 13.3 and 11 year peaks are not as prominent in the F-test results.

The phase of the difference between the time series is found by fitting an 18.6 year sinusoid to both the PSMSL and the synthetic signals and comparing their phases. The uncertainty for the amplitude is estimated as described above for the pole tide results, and is calculated here using an estimated noise level of 5 mm for both the gridded and ungridded stacks. The results are:

Ungridded PSMSL is 1.18 ± .22 times the synthetic;
   PSMSL leads by 1°±30°
Gridded PSMSL is 1.07 ± .22 times the synthetic
   PSMSL lags by 10° ± 30°

We combine these results to estimate an amplitude for the 18.6 year tide of 1.13 ± .22 times the equilibrium tide, and the phase of the tide to be equal to the equilibrium phase within a 30° uncertainty. A 30° phase difference corresponds to a time lead or lag of 19 months.

The agreement between the PSMSL and synthetic 18.6 year spectral peaks is not overly sensitive to the removal of blocks of stations (with the exception of the Baltic Sea stations, which have already been removed) or to the use of time spans different from 1900-1979. For example, when all stations in other inland seas are removed from the data set, the amplitude at 18.6 years is found to be affected by an amount that is within the range of the quoted uncertainties, although the frequency content of the noise does change.

The global rise in sea level

An observed secular sea level change at an individual station is not, by itself, evidence of a global rise in sea level. There could also be secular variations due to post-glacial rebound, local tectonic motion, or a shift in the wind-driven oceanic circulation pattern. The effects of these additional secular changes should be reduced in averages of global data. It is difficult, though, to adequately remove the effects of post-glacial rebound by averaging alone [Peltier, 1986]. Apparent changes in sea level at individual stations due to post-glacial rebound can be as large as 8.5 mm/yr, as is the case in the Gulf of Bothnia. And, a disproportionately large percentage of tide gauges are in the northern hemisphere, close to the centers of rebound. Large numbers of stations also lie in tectonically active areas, and no reliable model exists that allows us to remove the crustal motion from all these stations.

We digitized the rebound results from Peltier's [1986] post glacial rebound models for North America and northern Europe, and from Wagner and McAdoo [1986] for the remainder of the globe. In

order to assess global sea level changes most accurately, we simultaneously fit the entire data set to a linear trend and to an synthetic data set consisting of a set of trends predicted for each station by the combined rebound models as described above.

In order to establish a uniform benchmark for each station, a line is fit to each station and the y-intercept of this line is subtracted from each station record before the simultaneous fit. The intercepts subtracted from each record in this way are not the true intercepts for those stations having less than 80 years of data. For those subsets of stations containing many short records, this introduces a systematic error into the final trend. For example, if a station record having only a few years of data contains power at periods greater than the record length, the truncated periodic signals are correlated with the secular variability, and any true secular trend over several decades could be masked or even reversed.

On the other hand, if we restrict the data set to only those stations having 80 years or more of data, there might not be enough stations to optimally average out the secular variability caused by sources other than the global sea level rise. To compromise, we first construct a subset of the data that includes all stations with at least N years of data, where N is greater than 1 but probably less than 80. We choose N so that when we simultaneously fit the rebound and sea level rise to the data, the post glacial rebound fit parameter is close to 1.

For an initial data set, we choose N=37. This leaves us with 120 stations, and the simultaneous fit results in a rebound coefficient of .9. The increase in sea level revealed by the fit is 1.2 ± .1 mm/yr. The uncertainty is the rms value of the time series of global, yearly averages of all 120 stations, after the rebound is removed. A post glacial coefficient of .9 is a good indication both that the post glacial models are giving reasonable results, and that the global tide gauge data are capable of resolving linear trends on the order of millimeters per year.

In fact, we have been able to improve the fit by further restricting our global data set. First, we exclude 23 additional stations from regions of the globe having significant tectonic activity (all stations on the west coast of North America and Japan). When the 97 remaining stations in this reduced data set are simultaneously fit to the rebound data and the global sea level rise, the rebound coefficient is .94 and the rise in sea level is 1.6 ± .12 mm/year.

We further exclude all stations south of 30° north latitude. The post glacial rebound in this area is small and is reasonably the same everywhere (and so it is not easily separable from a global rise in sea level), and is strongly dependent on assumptions about the Pleistocene de-glaciation of Antarctica. This final data set consists of 84 stations, all with at least 37 years of data, situated north of 30° N latitude and away from Japan and the west coast of North America. The post glacial rebound data for all these stations are estimated from the results of Peltier's [1986] model. For these stations, the fit to the rebound model is especially good at .994 and the fit to the linear trend is 1.75 ± .13 mm/yr over the last 80 years. This trend is shown in Figure VI.9.

From these three results, we estimate a global sea level rise during the last 8 decades of between 1.1 and 1.9 mm/yr, with a preferred value near 1.75 mm/yr. And, because the post glacial fit parameter is so close to 1, we tentatively conclude that the effects of post-glacial rebound are well described by current models, and that the tide gauge data are capable of resolving global linear trends at the millimeter per year level.

CONCLUSIONS

By stacking global tide gauge data, we can significantly improve the signal-to-noise ratio for long period tides, compared with results obtained from single station records. We find that the 18.6 year tide and the pole tide are clearly evident above the noise in the spectra for the equilibrium stacks. The peaks are not evident in stacks against other pure spherical harmonics. The observed amplitude and phase for the 18.6 year tide are consistent with the assumption of global equilibrium. The amplitude and phase of the pole tide are close to the equilibrium amplitude and phase for all regions outside the North Sea, Baltic Sea and Gulf of Bothnia. In these basins, the enhanced tide appears to be more

71

consistent with narrow band meteorological forcing centered about the pole tide frequency than to a resonant response of the oceanic basin, although the results are not entirely conclusive. We find that in all regions except the Baltic Sea and Gulf of Bothnia, the oceanic response to atmospheric pressure are consistent with inverted barometer hypothesis for periods longer than two months. Our conclusions are based on the assumption that by using many stations, we were able to break the correlation between winds and pressure. This cannot be confirmed without including wind data in our analysis.

Finally, by simultaneously fitting the global the global sea level data to a linear trend and data prepared from a combined post-glacial rebound model, we conclude that the global rise in sea level over the last several decades was between 1.1 and 1.9 mm/year, with a preferred value near 1.75 mm/yr. Furthermore, the good agreement with the results from the post glacial models suggest that those results are reasonably representative of the true uplift, and that the tide gauge data are capable of resolving global changes in sea level at the millimeter per year level.

CHAPTER VI REFERENCES

Barnett, T.P., Possible changes in global sea level and their causes, *Climate Change, 5,* 15-38, 1983.

Carton, J.A. and J.M. Wahr, Modeling the Pole tide and its Effect on the Earth's Rotation, *Geophys. J. R. astr. Soc., 84,* 121-138, 1986.

Cartwright, D.E. and R.J. Tayler, New Computations of the Tide-generating Potential, *Geophys. J. R. astr. Soc., 23,* 45-74, 1971.

Cartwright, D.E. and A.C. Edden, Corrected Tables of Tidal Harmonics, *Geophys. J. R. astr. Soc., 33,* 253-264, 1973.

Chao, B.F., Correlation of Interannual Length-of-Day Variation With El Nino/Southern Oscillation, 1972-1986, *J. Geophys. Res., 93* B7,7709-7715, 1988.

Chelton, D., D. Enfield, Ocean Signals in Tide Gauge Records, *J. Geophys. Res., 91,* 9081-9098, 1986.

Dahlen, F.A., The Passive Influence of the Oceans on the Rotation of the Earth, *Geophys. J. R. astr. Soc., 46,* 363-406, 1976.

Dickman, S.R., The self-consistent dynamic pole tide in non-global oceans, *Geophys. J., 94,* 519-543, 1988a.

Dickman, S.R., Theoretical Investigation of the Oceanic Inverted Barometer Response, *J. Geophys. Res., 93* 14,941-14,946, 1988b.

Emery, K.O., Relative Sea level from Tide-gauge records, *Proceedings of the National Academy of Sciences, 7,* 6968-6972, 1980.

Gilbert, F. and A.M. Dziewonski, An application of Normal Mode Theory to the Retrieval of Structural Parameters and Source mechanisms from Seismic Spectra, *Phil. Trans. R. Soc. A, 278,* 187-269, 1975.

Gornitz, V., Lebedeff, S., and Hansen, J., Global Sea Level Trend in the Past Century *Science, 215,* 1611-1614, 1982.

Hansen, J., D. Johnson, A. Lacis, S. Lebedeff, P. Lee, D. Rind, and G. Russel, Climate impact of increasing atmospheric carbon dioxide, *Science, 213,* 957-966, 1981.

Hosoyama, K., I. Naito, and N. Sato, Tidal admittance of pole tide, *J. Phys. Earth, 24,* 51-62, 1976.

Lambeck, K. and S.M. Nakiboglu, *Geophys. Res. Lett., 10,* 857-860, 1983.

Lindberg, C.R., J. Park, and D.J. Thomson, Multiple Taper Analysis of Terrestrial Free Oscillations, parts I and II, *Geophys. J. R. astr. Soc., 91,* 755-836, 1987.

Luther, D.S., Evidence of a 4-6 day Barotropic, Planetary Oscillation of the Pacific Ocean, *J. Phys. Ocean., 12,* 644-657, 1982.

Merriam, J.B., Meteorological excitation of the annual polar motion, *Geophys. J. R. astr. Soc., 70*, 41-56, 1982.

Miller, S.P., and C. Wunsch, The pole tide, *Nature Phys. Sci., 246*, 98-102, 1973.

Munk, W.H., and D.E. Cartwright, Tidal Spectroscopy and Prediction, *Phil. Trans. R. Soc. Lond., A, 259*, 533-581, 1966.

Munk, W.H., and E.M. Hassan, Atmospheric excitation of the earth's wobble, *Geophys. J. R. astr. Soc., 4*, 339-358, 1961.

Munk, W.H. and G.J.F. Macdonald, *The Rotation of the Earth,* Appendix, Cambridge University Press, Cambridge, MA, 323 pp, 1975.

O'Connor, W.P. and T.B. Starr, Approximate Particular Solutions for the Pole Tide in a Global Ocean, *Geophys. J. R. astr. Soc., 75*, 397-405, 1983.

O'Connor, W.P., The 14 Month Wind Stressed Residual Circulation (Pole Tide) in the North Sea, *NASA Technical Memorandum 87800,* 1986.

Peltier, W.R., Deglaciation-Induced Vertical Motion of the North American Continent and Transient Lower Mantle Rheology, *J. Geophys. Res., 91, B9*, 9099-9123, 1986.

Pugh, D.T. and H.E. Faull, *Monthly and Annual Mean Heights of sea Level, Permanent Service for Mean Sea-Level,* Institute of Oceanographic Sciences, Bidston Observatory, Birkenhead, Merseyside L43 7RA, England, 1983a.

Pugh, D.T. and H.E. Faull, Operational Sea-level Stations, *Intergovernmental Oceanographic Commission Technical Series, 23,* Institute of Oceanographic Sciences, Bidston Observatory, Birkenhead, Merseyside L43 7RA, England, 1983b.

Rabbel, W., and J. Zschau, Static deformation and gravity changes at the earth's surface due to atmospheric loading. *J. Geophys., 56,* 81-99, 1985.

Rubincam, D.P., Post Glacial Rebound Observed by Lageos and the effective viscosity of the lower mantle. *J. Geophys. Res., 89,* 1077-1088, 1984.

Smith, M.L. and F.A. Dahlen, The Period and Q of the Chandler Wobble, *Geophys. J. R. astr. Soc., 64,* 223-282, 1981.

Thomson, D.J., Spectrum Estimation and Harmonic Analysis, *Proceedings of the IEEE, 70, 9,* 1055-1096, 1982.

Van Dam, T. and J.M. Wahr, Displacements of the earth's surface due to atmospheric loading: effects on gravity and baseline measurements. *J. Geophys. Res., 92,* 1281-1286, 1987.

Wagner, C.A. and D.C. McAdoo, Time Variations in the Earth's Gravity Field Detectable With Geopotential Research Mission Intersatellite Tracking, *J. Geophys. Res., 91, B8,* 8373-8386, 1986.

Wahr, J.M. The effects of the atmosphere and oceans on the earth's wobble and on the seasonal variations in the length of day - 2. Results. *Geophys. J. R. astr. Soc. 74,* 451-487, 1983.

Wilson, C.R., Haubrich, R., Meteorological excitation of the earth's wobble. *Geophys. J. R. astr. Soc., 46,* 707-743, 1976.

Wunsch, C., Bermuda Sea Level in Relation to Tides, Weather, and Baroclinic Fluctuations, *Reviews of Geophys. and Space Phys., 10,* 1-49, 1972.

Wunsch, C., Dynamics of the North Sea Pole Tide Reconsidered, *Geophys. J. R. astr. Soc., 87,* 869-884, 1986.

Yumi, S. and K. Yokoyama, *Results of the International Latitude Service In a Homogeneous System,* Central Bureau of The International Polar Motion Service, International Latitude Observatory of Mizusawa, Mizusawa, Japan, 1980.

Figure VI.1. The coefficients, $A(\tau)$, of the least squares fit of sea level to atmospheric pressure for 487 stations outside the North and Baltic Seas and Gulf of Bothnia. Seasonal averages have been removed from both the pressure and sea level data. The response is consistent with the inverted barometer assumption for time lags of up to ± 240 months.

Figure VI.2   Amplitude spectra at the Chandler wobble frequency band for Y_2^1 stacks of 487 stations. The solid curve is for the PSMSL stack, the long dashed curve is for the synthetic (equilibrium) data and the short dashed curve is the spectrum obtained when the synthetic stack is subtracted from the PSMSL stack. The effects of pressure have been subtracted from the PSMSL data, assuming an inverted barometer response. The Chandler wobble is clearly evident in the PSMSL results, and its amplitude is close to equilibrium. Stations in the North and Baltic Seas and in the Gulf of Bothnia are not included in the stacks. (a) Ungridded. (b) 10° by 20° grid.

Figure VI.3   Amplitude spectra of Y_2^1 stacks of sea level, pressure, and the equilibrium pole tide (solid, short dashed, and long dashed curves respectively) for: (a) the North Sea (sea level is 3.6 times the equilibrium pole tide at the 437 day period); (b) the Baltic Sea (sea level is 6.2 times equilibrium at the 437 period); (c) the Gulf of Bothnia (sea level is 9 times equilibrium at the 437 day period); (d) the global oceans outside the North Sea region (the sea level and equilibrium spectra are in good agreement, and there is no prominent pressure peak in the pole tide frequency band). This figure differs from Figure VI.2 (b) in that, here, seasonal averages have been removed from the PSMSL data but pressure has not. The pressure data have been multiplied by 10 mm/mbar prior to constructing the stack. Note the similarity between the sea level and pressure spectra for each of the three shallow basins. In this figure and in Figure VI.4, the peaks in the pressure and sea level are as narrow as the pole tide band itself.

Figure VI.4   Coherence spectra for sea level versus pressure for Y_2^1 stacks of: (a) 26 North Sea stations; (b) 42 Baltic Sea stations; (c) 19 stations in Gulf of Bothnia; (d) 487 stations for global oceans outside the North Sea region. In all four parts of this figure, seasonal averages have been removed from sea level and pressure prior to constructing the coherence. There are several frequency bands where the coherence exceeds .43 (the 95 per cent confidence level), including the pole tide frequency band for the three shallow basins.

Figure VI.5   Amplitude spectra for Y_2^1 stacks from stations in the North Sea region. (a) Stacks for 42 stations in the Baltic Sea. The solid curve is PSMSL. The pressure is fitted and removed from the PSMSL data, giving the short dashed curve. The equilibrium tide is removed and the the pressure is fitted and removed to give the long-dashed curve. Note that the long-dashed curve does not follow the features of the equilibrium pole tide, which is the dash-dot curve near the bottom. (b) Same as (a), but for the 19 stations in the Gulf of Bothnia. (c) Stacks for the Baltic Sea, shown over a large frequency range. The solid curve is the PSMSL data, and the short dashed curve is the pressure. Both spectra show peaks in the pole tide band, but the PSMSL peak stands above all other spectral peaks, the pressure peak does not.

Figure VI.6   An ungridded Y_2^0 stack of 260 stations as a function of time. The 16-20 year variation in the PSMSL stack, solid curve, is discernible, as is increased noise early in the time span. The dashed curve is the stack of synthetic data.

Figure VI.7   Amplitude spectra for Y_2^0 stacks of 260 stations outside the Baltic sea. The solid curve is the spectrum for the PSMSL data, the long dashed curve is for the synthetic stack, and the short dashed curve is a spectrum of the difference between the two stacks (a) Ungridded. (b) 15° by 30° grid.

Figure VI.8   F-test derived from Multi-taper spectra for an ungridded Y_2^0 stack of the PSMSL signal. The F-test predicts with a 95 percent certainty that the 18.6 year peak is sinusoidal.

Figure VI.9   Linear trend for sea level for 84 stations having greater than 37 years of data that lie north of 30^0 north latitude and are not in tectonically active areas (Japan and the west coast of North America are excluded). Vertical motion at the surface is simultaneously fit to these data using a model of post glacial rebound from Peltier [1986]. The fit to this model is excellent for these stations at .994, and the fitted rate of global increase in sea level is $1.75 \pm .13$ mm/yr.
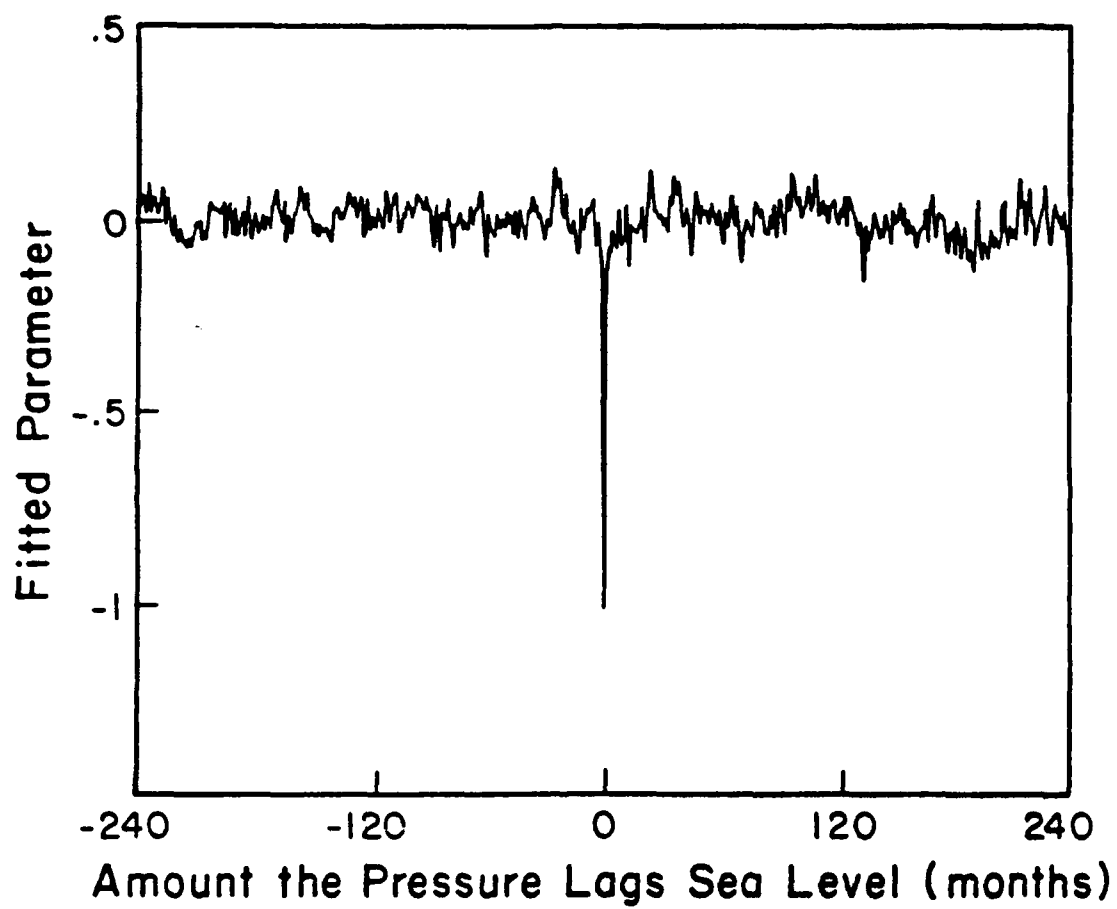
Figure VI.1

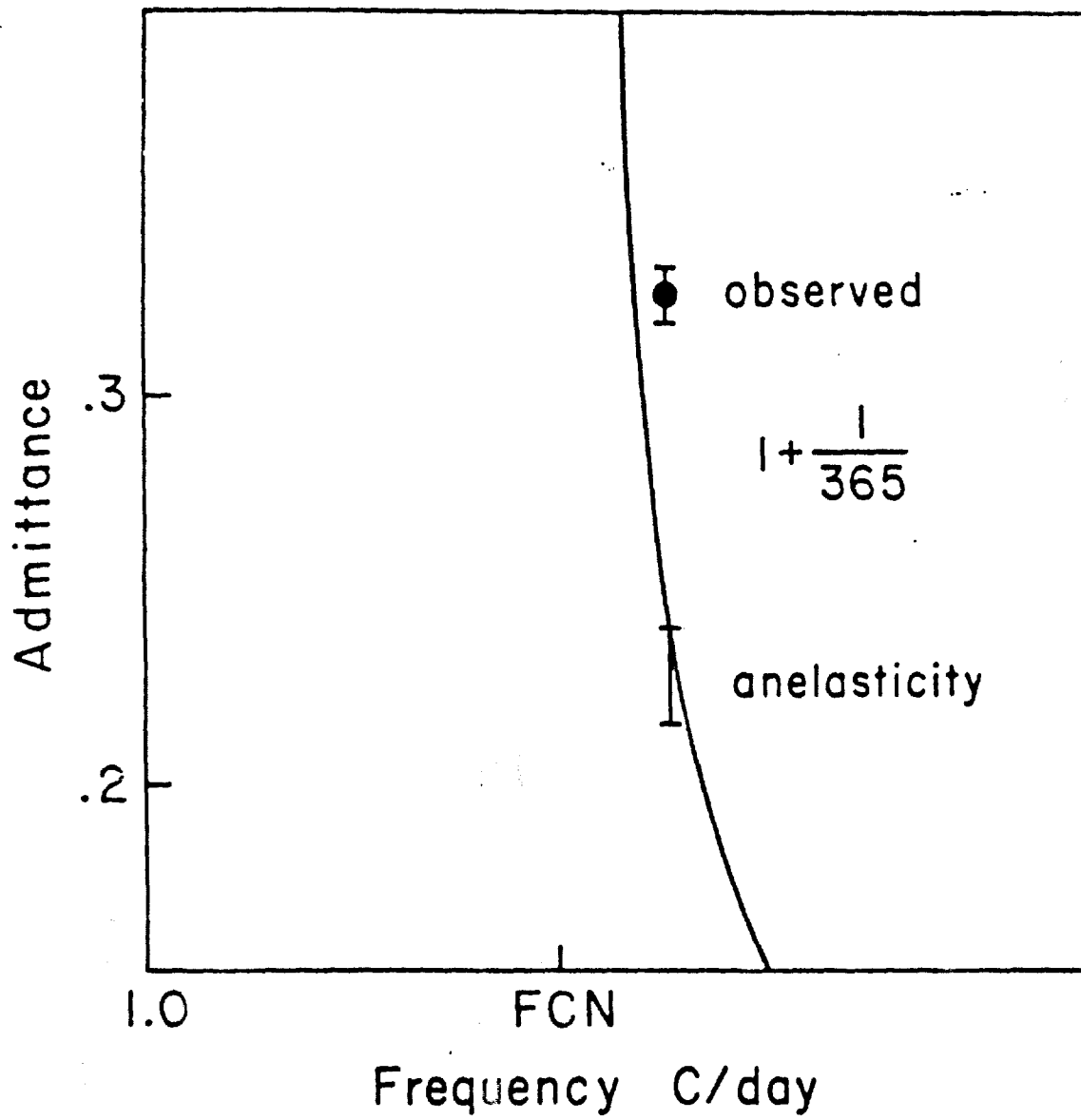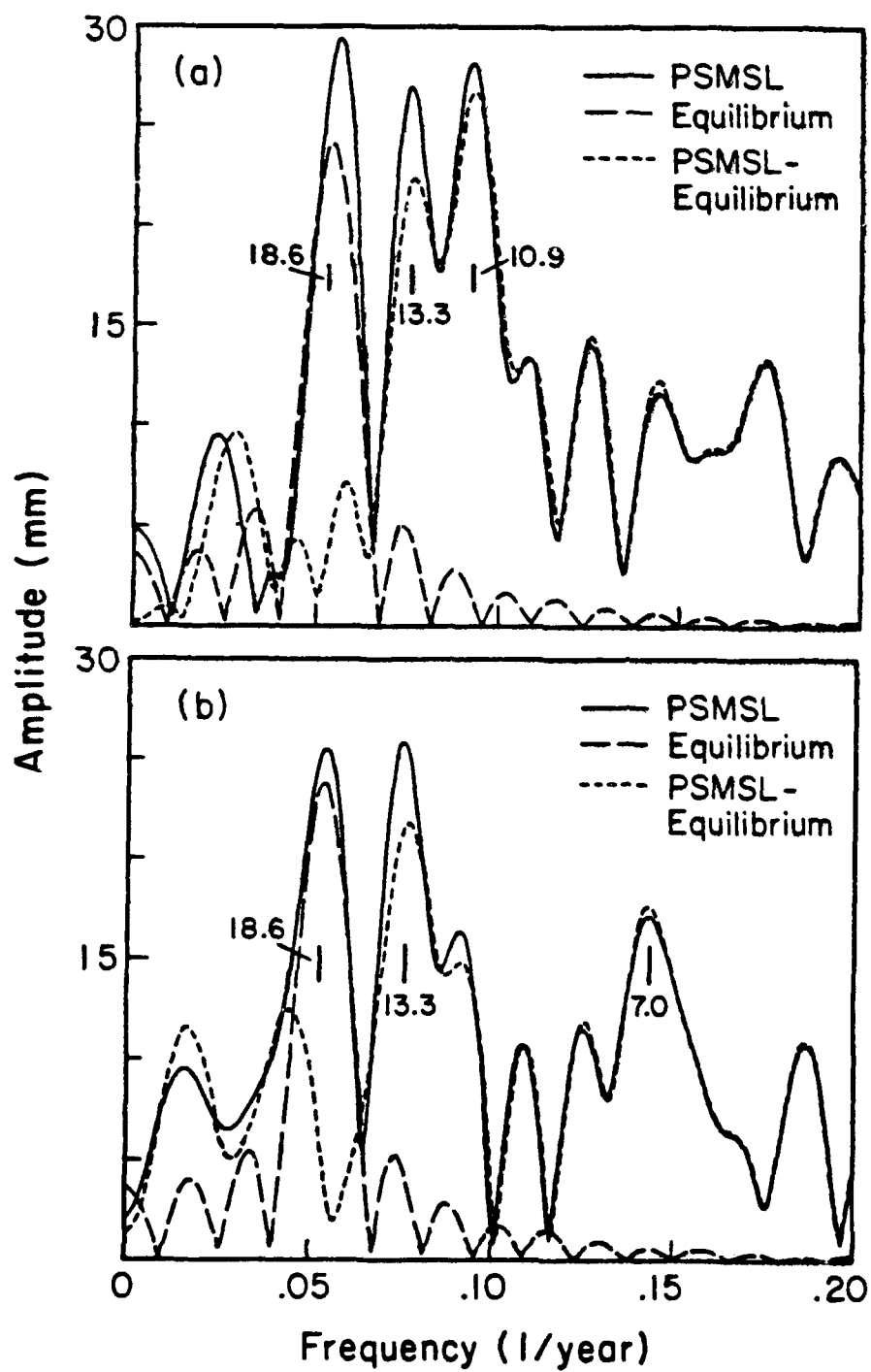Figure VI.2

77

Figure VI.3

78

Figure VI.4

79

Figure VI.5

80
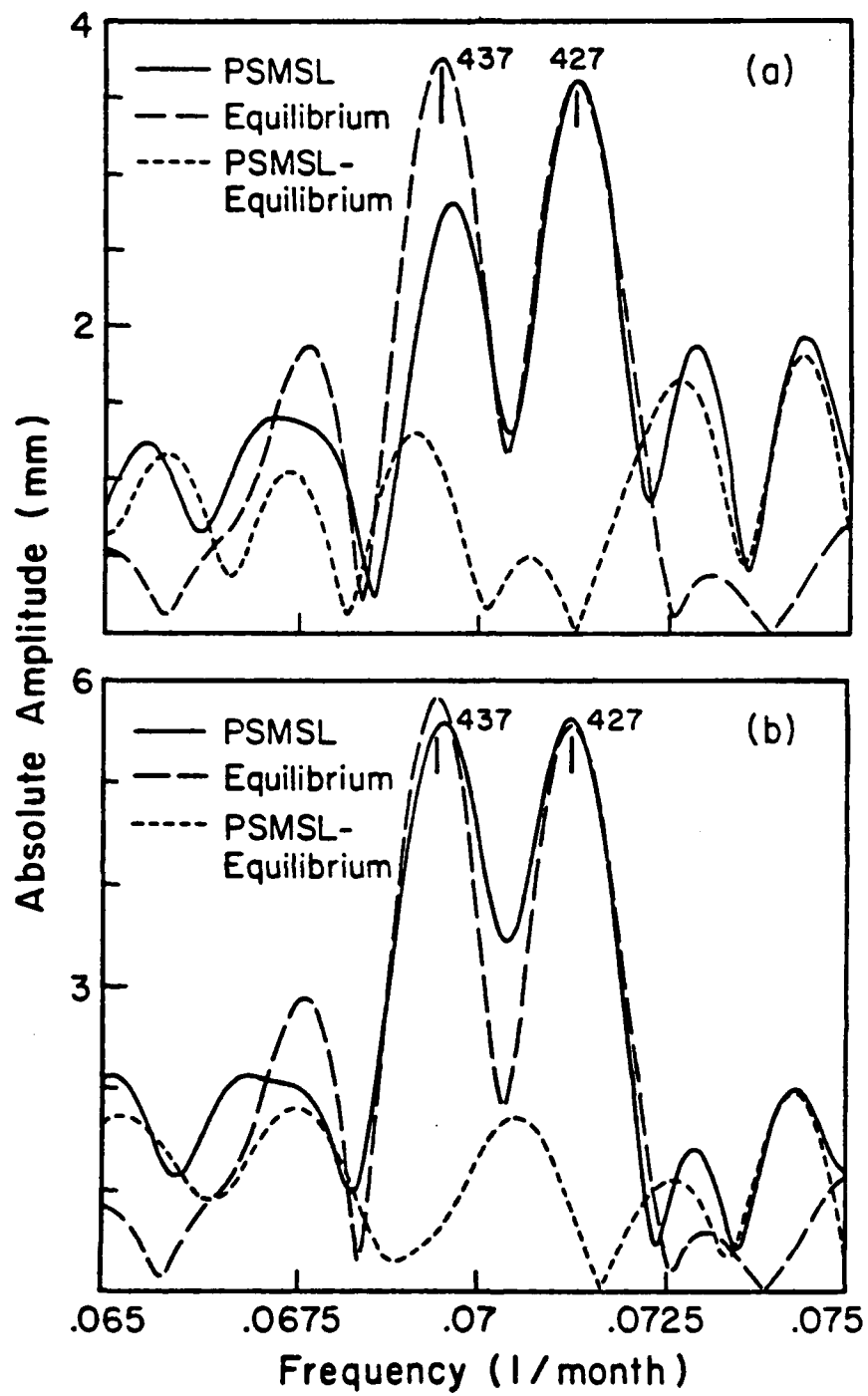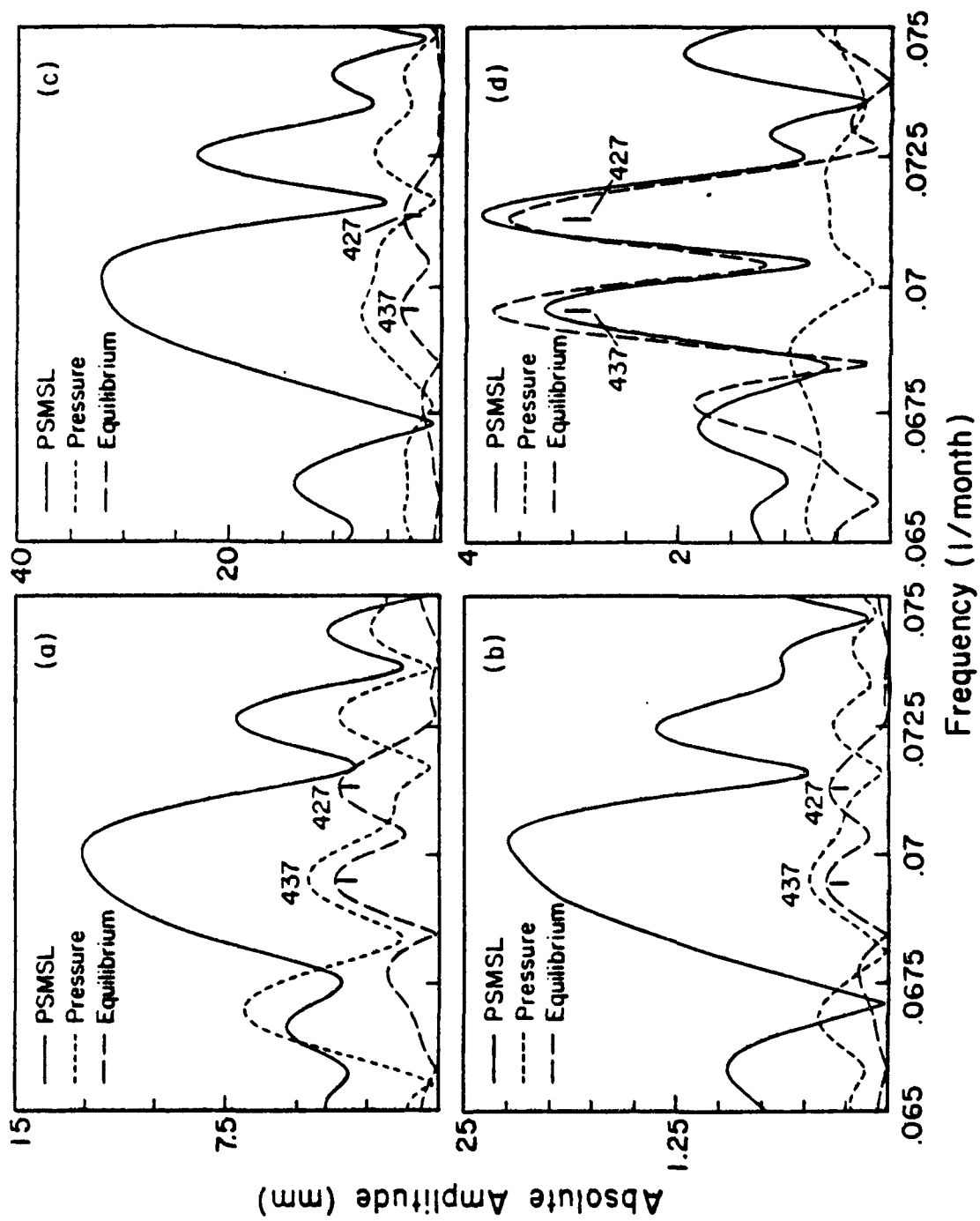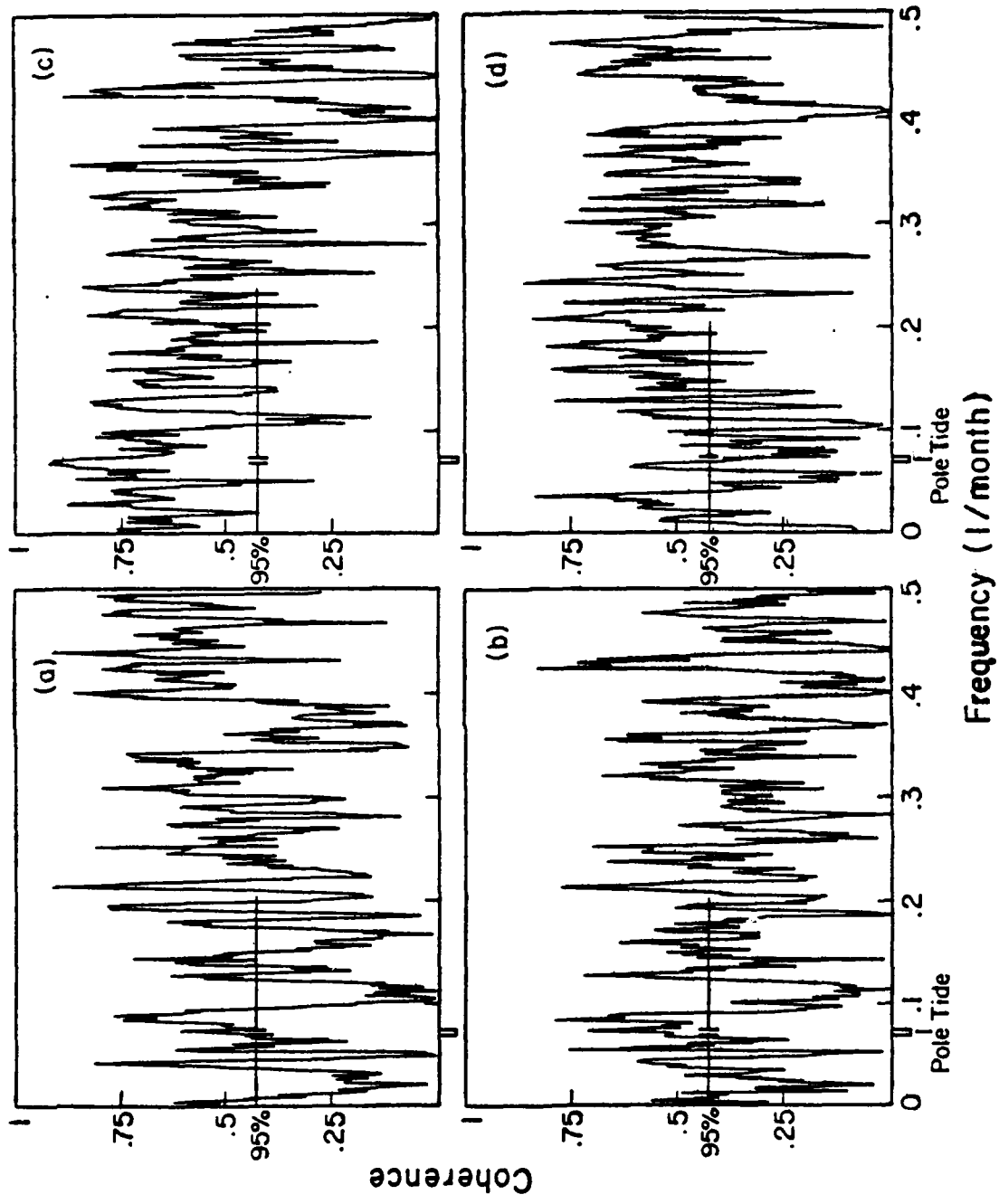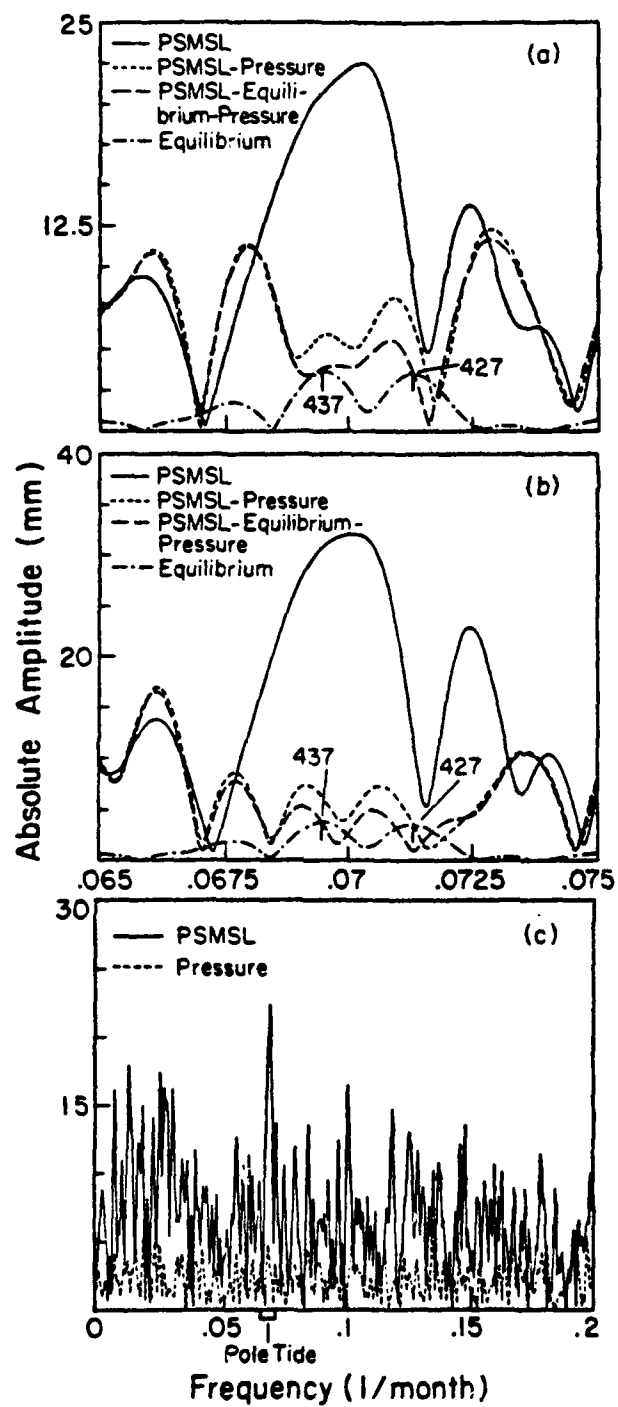
Figure III.4

Figure VI.7

Figure VI.8

Figure VI.9